Electronic transport in nanocrystalline germanium/hydrogenated amorphous silicon composite thin films

A DISSERTATION

SUBMITTED TO THE FACULTY OF THE GRADUATE SCHOOL

OF THE UNIVERSITY OF MINNESOTA

BY

Kent Edward Bodurtha

IN PARTIAL FULFILLMENT OF THE REQUIREMENTS

FOR THE DEGREE OF

DOCTOR OF PHILOSOPHY

Dr. James Kakalios

February 2015

© Kent Edward Bodurtha 2015

Acknowledgements

First and foremost, I thank my wife, Nikki, for 6+ years of support and understanding while I squirreled away my time and energy in the basement of the physics building. She has helped me cope with the frustrations when things go unexpectedly badly, and been there to share in the excitement when things go unexpectedly well. I know I could not have completed this degree with anything close to the level of happiness, balance, and sanity I enjoy in my life without her.

I also want to thank my advisor, Jim Kakalios, for his leadership and direction in the projects outlined here. As the process of completing a research Ph. D. is really one of a learning experience, I am grateful for his patience and desire to foster an educational environment in the lab.

I must acknowledge those who came before me – my coworkers who are also good friends – and their significant contributions to my experience. Charlie Blackwell and Yves Adjallah were the senior grad students when I started in Prof. Kakalios' group, and they laid the foundation of my knowledge about lab techniques and general amorphous semiconductor physics. I first met Charlie at a new grad student lunch, and his knowledge, passion, and charm played a major role in my decision to join the Kakalios group. He showed me the ins and outs of plasma deposition. Yves was a vast repository for information on the characterization side of my work. He taught me all about thermopower, and if I had not been able to build on his successes, I don't know how I would have achieved the results I did.

My contemporaries, Lee Wienkes, Ghidewon Arefe and Zvie Razieli, made my years of research easier and much more fun. I was fortunate to have Lee as the senior grad student in the Kakalios lab for around three years. Lee is one of the most brilliant physicists I've known, and he was a huge resource for my own work. He put up with me bouncing ideas off him and struggling to understand new concepts and weird results. He was also a driving force in improving and streamlining many of the more menial aspects of the lab's operation, from all of which I benefitted greatly. Ghidewon eased the burden of my coursework in the early years, and we spent countless hours in the NFC working, problem-solving and joking around together. In the last few years, Zvie was gracious to take time from his own projects to help me sort through numerous minor and major issues in my work.

Many of the faculty and staff at the University of Minnesota and elsewhere have contributed to this work. Chapter 6 of this thesis would not exist if it were not for the guiding help of Boris Shklovskii in understanding the unexpected results. I thank him for his patience while I tried to follow the theoretical work already developed for the model as described, and Sergei Baranovsk at Philipps-University Marburg for helping me understand some of his more current results. The staff at the Minnesota Nano Center (MNC), formerly the Nanofabrication Center (NFC), has been very helpful in keeping the deposition system running smoothly and safely. I would like to thank Gary Olin in particular: for the majority of my time as a graduate student, I was the sole user of germane gas in the entire NFC. Every time a squirrel died in the exhaust vent for the NFC in Keller Hall, forcing all process gas lines to shut off (there were other causes too), Gary would take the time to restart the germane gas line for me.

I also want to thank my friends outside our group: Dave Rowe, Lance Wheeler and Jason Trask in Prof. Kortshagen's group; Yeonbae Lee, Joe Kinney, Terry Bretz-Sullivan and Ilana Percher in Prof. Goldman's group; Chad Gepphert and Andrew Galkiewicz in Prof. Crowell's group.

Dedication

I dedicate this thesis to my daughter, Viivi.

Abstract

Recent interest in composite materials based on hydrogenated amorphous silicon (a-Si:H) stems in part from its potential for technical applications in thin film transistors and solar cells. Previous reports have shown promising results for films of a-Si:H with embedded silicon nanocrystals, with the goal of combining the low cost, large area benefits of hydrogenated amorphous silicon with the superior electronic characteristics of crystalline material. These materials are fabricated in a dual-chamber plasma-enhanced chemical vapor deposition system in which the nanocrystals are produced separately from the amorphous film, providing the flexibility to independently tune the growth parameters of each phase; however, electronic transport through these and other similar materials is not well understood. This thesis reports the synthesis and characterization of thin films composed of germanium nanocrystals embedded in a-Si:H. The results presented here describe detailed measurements of the conductivity, photoconductivity and thermopower which reveal a transition from conduction through the a-Si:H for samples with few germanium nanocrystals, to conduction through the nanocrystal phase as the germanium crystal fraction X_{Ge} is increased. These films display reduced photosensitivity as X_{Ge} is increased, but an unexpected increase in the dark conductivity is found in samples with $X_{Ge} > 5\%$ after long light exposures. Detailed studies of the conductivity temperature dependence in these samples exposes a subtle but consistent deviation from the standard Arrhenius expression; the same departure is found in samples of pure a-Si:H; a theoretical model is presented which accurately describes the actual conductivity temperature dependence.

Contents

Acknowledgements i

Dedication iv

Abstract v

Contents vi

List of Tables ix

List of Figures x

Chapter 1 – Introduction 1

1.1 – Material Synthesis 3

1.1.1 – Amorphous films 3

1.1.2 – Nanocrystals 5

1.1.3 – Mixed-phase nc-Ge/a-Si:H 6

1.2 – Electronic Transport in a-Si:H 9

1.3 – Thermoelectric Effect 15

1.4 – Photoconductivity of a-Si:H 18

Chapter 2 – Characterization Techniques 21

2.1 – Structural Characterization 21

2.1.1 – Raman Spectroscopy 21

2.1.2 – Fourier Transform Infrared Reflectometry (FTIR) 26

2.1.3 – Rutherford Backscattering (RBS).. 29

2.1.4 – X-Ray Diffraction... 31

2.1.5 – Profilometry.. 34

2.2 – Electronic Characterization...34

2.2.1 – Conductivity 34

2.2.2 – Thermopower.. 37

2.2.3 – Photoconductivity... 38

Chapter 3 – Structural Results of nc-Ge/a-Si:H films 40

3.1 – Raman Spectroscopy...40

3.2 – X-Ray Diffraction 44

3.3 – Rutherford Backscattering (RBS) 46

3.4 – Fourier Transform Infrared Spectroscopy...49

Chapter 4 – Transport Properties of nc-Ge/a-Si:H films 53

4.1 – Conductivity...53

4.2 – Thermopower 57

4.3 – Discussion 61

Chapter 5 – Photo-Induced Enhanced Conductivity in nc-Ge/a-Si:H 75

5.1 – Background 75

5.2 – Light-Induced Enhanced Conductivity 76

5.3 – Metastability..........81

5.4 – Discussion 84

Chapter 6 – Non-Arrhenius Conductivity..........88

6.1 – Results 88

6.2 – Discussion 95

Chapter 7 – Conclusions 101

References..........104

Appendices..........108

Appendix A 108

Appendix B 109

List of Tables

Chapter 5 | Page

Table I: Results of fits to $\sigma(T) = \sigma_0 \exp[E_\sigma / k_B T]$ and $\sigma(T) = \sigma_1 \exp[-(T_0 / T)^\kappa]$ for a variety of samples. 94

List of Figures

Chapter 1 Page

Figure 1.1: Cartoons of (a) a deposition chamber for a-Si:H thin films and (b) flow-through tube reactor for synthesis of nc-Si. 3

Figure 1.2: Sketch of the dual-chamber dual-plasma co-deposition system used to synthesize the nc-Ge/a-Si:H thin films. An upstream plasma fed by GeH_4 and Ar creates the nc-Ge, which are carried downstream to the film plasma, which is tuned to grow high-quality a-Si:H thin films. As the a-Si:H grows, germanium nanocrystals are embedded in the films, producing a composite material 7

Figure 1.3: Sketch of a single substrate after preparation into 4 distinct samples. The nc-Ge/a-Si:H film is deposited on a glass square, usually with a gradient in X_{Ge}. Two electrodes are deposited parallel to the direction of the gradient, and the sample is scribed into 5 rectangles of approximately constant nc-Ge concentration. Four of these become distinct samples with relatively constant X_{Ge}. The fifth is used to monitor the temperature on either side for the thermopower measurements. 9

Figure 1.4: Sketches of the density of states for crystalline silicon (left) and hydrogenated amorphous silicon (right). The energy gap shown here for crystalline silicon is an indirect gap, and the direct bandgap is 1.4 eV. 12

Chapter 2

Figure 2.1: Raman spectrum of a pure a-Si:H thin film (black). The total measured spectrum can be decomposed into four separate Gaussian peaks, centered at 480 cm^{-1} (blue), 410 cm^{-1} (cyan), 320 cm^{-1} (red), and 175 cm^{-1} (magenta), shown as dotted lines. The sum of these four peaks is shown by the solid green line. 24

Figure 2.2: Measured absorption via Fourier Transform Infrared Reflectometry on a pure hydrogenated amorphous silicon sample (black), zoomed in to show the Si-H vibrational modes. The total fit (green) is composed of two Gaussian peaks, one at 2000 cm^{-1} (red) and another at 2090 cm^{-1} (cyan), corresponding to Si-H and Si-H_2 bonds, respectively. The level of disorder present in the film is characterized by $R = A_{2090} / \left(A_{2090} + A_{2000} \right)$, which is 0.47 for this sample. 28

Figure 2.3: Rutherford Backscattering measurement (black) and matching simulation (red) for the bare glass used as a substrate for the nc-Ge/a-Si:H samples presented in this thesis. 30

Figure 2.4: Cartoon illustrating the origin of nonzero X-ray diffraction peak widths in nanocrystals. Coherent X-rays are incident at an angle θ_D slightly smaller than the angle θ_B, which satisfies the Bragg relation, such that the path length difference between adjacent planes is 1.1λ, slightly longer than in the simple Bragg case. The phase of X-rays scattered off each plane, relative to the top plane, is denoted by the color of the line, where red lines are in phase and blue lines are out of phase. In this case, X-rays scattered 6 lattice planes away destructively interfere, and X-rays scattered off the adjacent plane interfere nearly constructively. 33

Figure 2.5: Cartoon of the sample stage in the closed-cycle He cryostat used for conductivity measurements presented in this thesis. The sample is attached to the stage using thermal grease, and electrical connection is made to the electrodes on the sample surface. The temperature sensor labeled "T_Control" is used by the temperature controller along with the heater to control the temperature of the stage. The sensor labeled "T_Sample" gives the temperatures reported in the data in this thesis. The sample can reach temperatures up to 470 K and is thermally separated from the cold head, which is always below 70 K, by a sapphire crystal. 36

Figure 2.6**:** Sketch of the sample holder for thermopower measurements. The sample is placed so the electrodes are parallel to and atop two copper blocks, which each have an embedded heater (H1 and H2). The temperatures at each block are independently controlled using platinum resistors T_3 and T_4 as input sensors; these platinum resistors are mounted on glass slides so that their temperatures are similar to the sample temperatures. Thermocouples T_1 and T_2 are attached in a region that is electrically isolated from the measurement of V_1 and V_2, and are used in calculations of the Seebeck coefficient. 38

Chapter 3

Figure 3.1: Raman spectra for five samples produced in the same deposition run, but different distances from the nanocrystal injection tube. These spectra have been normalized to the a-Si:H TO mode at 480 cm^{-1}. 41

Figure 3.2: Raman spectrum of a nc-Ge/a-Si:H sample with X_{Ge} ~ 36% from Figure 3.1 illustrating the process used to fit the nc-Ge component and determine X_{Ge}. The full Raman spectrum (gray) contains broad Gaussian peaks associated with the a-Si:H component which overlap significantly with the Si-Ge peak. The a-Si:H component is first subtracted from the full signal, and the black curve is obtained, which can be fit (red) to 6 Gaussian peaks which overlap only slightly. 44

Figure 3.3: X-ray diffraction measurements on three nc-Ge/a-Si:H samples showing peaks due to diffraction in the (111) and (220) planes, where the germanium crystal fraction labeled for each sample was determined by Raman spectroscopy. These samples were synthesized in the same deposition run and display diffraction peak widths that correspond to nanocrystal diameters of 3.5-4.5 nm. 45

Figure 3.4: Rutherford backscattering measurement (black) and matching model (red) for a nc-Ge/a-Si:H sample with X_{Ge} ~ 32%. 47

Figure 3.5: Plots of measured FTIR spectra and fits to those spectra for samples from a single deposition run with (a) X_{Ge} ~ 0%, (b) X_{Ge} ~ 2.5%, and (c) X_{Ge} ~ 21%. The thick black line is the measured data and the red line is the sum of the Gaussian peaks in blue, green, orange and magenta. 50

Figure 3.6: Plot of the *R* factor, a measure of the relative FTIR absorption at 2090 cm^{-1} to that at 2000 cm^{-1} and 2090 cm^{-1}, against the germanium crystal fraction X_{Ge} for a number of nc-Ge/a-Si:H samples with X_{Ge} between 0 and 70%. 52

Chapter 4

Figure 4.1: Arrhenius plots of the conductivity for three nc-Ge/a-Si:H films with X_{Ge} of 3% (red circles), 14% (green triangles) and 39% (blue squares). The inset shows calculations of the reduced activation energy vs. temperature on a log-log plot for each curve in the main figure. 54

Figure 4.2: Arrhenius plot of the conductivity of the transition film with X_{Ge} = 14% from Figure 4.1 (green triangles). The red (circles) and blue (squares) lines represent thermally activated conductivities with activation energies of 0.77 eV and 0.43 eV, respectively. The dashed line indicates the result of adding the two thermally activated expressions. The inset shows calculations of the reduced activation energy vs. temperature on a log-log plot for the same set of curves. 56

Figure 4.3: Plot of the activation energy obtained from Arrhenius plots of the dark conductivity against germanium crystal fraction for a series of nc-Ge/a-Si:H films. For films in the transition region (as in Figure 4.2), which are best described by two activation energies, both values from high and low temperature fits are plotted. 57

Figure 4.4: Plots of measured voltage vs. temperature for three samples with (a) X_{Ge} ~ 0%, (b) X_{Ge} ~ 18%, and (c) X_{Ge} ~ 54%. Each curve on the plots represents the voltage measurements at temperatures $T = T_{avg} \pm \Delta T/2$ and $T = T_{avg}$. Note change of scale for Figure 4.4a. A negative slope indicates n-type conduction, while a positive slope indicates p-type conduction. 59

Figure 4.5: Measured Seebeck coefficients plotted against $1000/T_{avg}$ for nc-Ge/a-Si:H thin films with X_{Ge} = 0 (pure a-Si:H) to X_{Ge} = 75%. 60

Figure 4.6: Cartoon representation of the dual-channel model describing conduction through these nc-Ge/a-Si:H samples. One imagines consolidating all the germanium nanocrystals into a single sample, and the remaining a-Si:H film in a separate sample, then measuring across the parallel combination of the two samples. 62

Figure 4.7: Plot of calculated Seebeck coefficient against $1000/T_{avg}$ for temperatures between 350K and 450K and for X_{Ge} = 0 to 60% using the simple volume fraction model, Equation (4.3). 64

Figure 4.8: Simple sketch of the band offsets for a-Si:H and nc-Ge, assuming equilibrium conditions. The bandgap of nc-Ge is estimated to be 1.4 eV for 4 nm crystals 66

Figure 4.9: Plot of the calculated volume fractions of the a-Si:H phase (%Si), nc-Ge phase (%Ge) and voids as a function of germanium crystal fraction for the eight samples measured by RBS. For each sample, the three phases add to 100%. 68

Figure 4.10: Plot of the conductivities at 450 K of a number of samples with different germanium crystal fractions X_{Ge}. Samples that are n-type at 450 K, as measured by the thermopower, are represented as red circles. Samples that are p-type at 450 K are represented as blue squares. The purple line crossing through the n-type data points with $5 < X_{Ge} < 20\%$ is a power-law fit reflecting the expected decrease in the conductivity approaching the percolation threshold of the a-Si:H phase. 70

Figure 4.11: Plot of the calculation of the conductivity vs 1000/T using Equation (4.4) (a) for a variety of germanium crystal fractions. Plot of the calculated fraction of conductivity through the n-type phase vs 1000/T (b) for the same values of X_{Ge} in (a). Plot of the calculated Seebeck coefficients vs 1000/T using Equation (4.9) (c) for the same values of X_{Ge} in (a). Plot of the measured Seebeck coefficients vs 1000/T from Figure 4.5 (d). 74

Chapter 5

Figure 5.1: Plot of the photosensitivity as a function of light exposure time for multiple nc-Ge/a-Si:H samples. Each photosensitivity curve is calculated from Equation (5.1). 78

Figure 5.2: Log-log plot of the ratio of the dark current $\sigma_B(t)$ after exposure to light for time t, to the initial state A conductivity σ_A for a number of nc-Ge/a-Si:H samples. Each data point was taken after turning off the lamp and allowing the sample temperature to stabilize, and the light exposure time is the cumulative time the sample was exposed to the light. The black dash-dotted line marks $\sigma_B / \sigma_A = 1$, that is, no change from the state A conductivity. Samples with the same symbol are from the same deposition run, and this plot combines samples from two different deposition runs. 79

Figure 5.3: Plot of the photoresponse as a function of the cumulative light exposure time, calculated used Equation (5.2), for the data in Figure 5.1 and Figure 5.2. 80

Figure 5.4: Log-linear plot of the decay of the photo-enhanced excess conductivity versus time for a single film with X_{Ge} ~ 16%. The y-axis is the dark conductivity measured after 24 hours of illumination, normalized to 1 at $t = 0$ and to zero at $t = \infty$. The dashed lines are exponential fits to each curve, which represents the decay at temperatures between 320 K and 410 K. 83

Figure 5.5: Arrhenius plot of the values of τ found for each curve in Figure 5.4, plotted versus 1000/T. 84

Chapter 6

Figure 6.1**:** Log-log plots of the reduced activation energy versus temperature for four nc-Ge/a-Si:H samples with germanium concentrations as determined by Raman measurements included. Overlaid on each plot are model curves of the form $\sigma(T) = \sigma_1 \exp[-(T_0/T)^{\kappa}]$ where κ is equal to -1 (gray), -3/4 (green) and -1/2 (violet). 90

Figure 6.2**:** Plot of the temperature dependence of the conductivity of a nc-Ge/a-Si:H sample with X_{Ge} ~ 3%, when plotted against T^{-1} (violet curve) and $T^{-0.82}$ (green curve). 91

Figure 6.3**:** Log-log plot of the reduced activation energy for an a-Si:H sample with no Ge nanocrystals, against temperature. Also shown is the expected reduced activation energy for a T^{-1} (gray) and $T^{-1/2}$ (violet) temperature dependence, and a fit to the data (black). 93

Figure 6.4**:** (a) Log-log plot of the reduced activation energy versus temperature and (b) Arrhenius plot of the conductivity versus 1000/T for the sample in Figure 6.1a and Figure 6.2. In both of these figures, the data is shown in red and the transport energy model is shown in violet. In Figure 6.4b, the black lines represent best fits to an Arrhenius temperature dependence, yielding average activation energies E_{σ} = 0.75 and 0.78 eV for the data and model, respectively. 100

– Chapter 1 –

Introduction

No other amorphous material comes close to the level of study and understanding devoted to hydrogenated amorphous silicon. Its appeal arises from the fact that single-crystal silicon is not particularly well-suited to many semiconductor device applications. Single-crystal semiconductors are composed of a periodic arrangement of atoms that usually corresponds to the ideal environment for each atom. Defects in the crystal can arise unintentionally, and will usually lead to a degradation of the electrical characteristics of the sample. Amorphous materials have been grown in such a way that there are many defects throughout the sample, and while the electrical performance may not match the standard of a single-crystal, the growth process for amorphous materials is often much cheaper and easier than that of crystals, especially when one requires thin film semiconductors deposited over large areas on non-lattice matched substrates. The most common method of producing single-crystal silicon involves slowly drawing a crystalline ingot from a vat of molten silicon, then, after refinement, slicing the ingot into thin wafers. For applications that require very thin samples, this method is impractical because the wafers must be a minimum of a few hundred μm thick for structural integrity. While other methods can achieve nm-level thicknesses in a single-crystal of silicon, they are often not economically viable.

Amorphous silicon can be easily and inexpensively deposited onto virtually any substrate, in whatever thickness is desired. The deposition process can also be scaled up to

cover large areas very easily. This makes it a good candidate for such applications as transistors in LCD and LED displays [1], and solar cells [2]. At the time of this writing, however, crystalline silicon-based solar cells maintain an edge in price/power ratio and are the de facto standard for photovoltaics. While amorphous silicon's promise for solar energy production lies in its affordability and its amenability to thin, large area deposition, it suffers from serious electrical performance drawbacks, which have kept its efficiency quite low (<10%). Research continues in order to improve amorphous silicon for use in solar cells, and in recent years, focus has shifted to using amorphous silicon as the basis for more complex materials. The goal of these new composite materials is to resolve some of the most intractable downsides to amorphous silicon and also develop new, interesting properties. A promising direction involves embedding nanocrystals in amorphous silicon, in the hopes of achieving the best of both worlds: the low cost and large area advantages of amorphous silicon, and the superior electronic properties of crystalline silicon. Previous studies have investigated the role of silicon nanocrystals embedded in amorphous silicon. This thesis builds on that previous work by exploring the electronic properties of a composite material of germanium nanocrystals embedded in amorphous silicon.

In this thesis, I will describe the synthesis and characterization of hydrogenated amorphous silicon thin films with germanium nanocrystal inclusions. These results extend our understanding of how these nanocrystalline inclusions affect the transport properties of hydrogenated amorphous silicon thin films. In particular, the motivation for these studies is the desire to understand the underlying transport mechanisms resulting from the interactions between amorphous and nanocrystalline materials in a single composite structure.

1.1 – Material Synthesis

1.1.1 – Amorphous films

Hydrogenated amorphous silicon (a-Si:H) thin films are most commonly synthesized via Plasma-Enhanced Chemical Vapor Deposition (PECVD) [3] and its many variants, including remote plasma deposition [4], expanding thermal plasma (ETP) [5] and very high frequency PECVD (VHF-PECVD) [6]. Silane gas (SiH_4) flows between two parallel-plate electrodes in a vacuum chamber, sketched in Figure 1.1a. A radio-frequency AC power source, usually at 13.67 MHz, with a power of ~ 50 mW/cm^2 excites the silane gas into a plasma where some of the silane molecules are stripped of a hydrogen atom [7]. When both the plasma power and the silane partial pressure are low enough, very little recombination occurs, so a positive DC voltage builds up on the interior surfaces in the vacuum chamber, related to the capture of the very mobile H^+ nuclei. This positive voltage

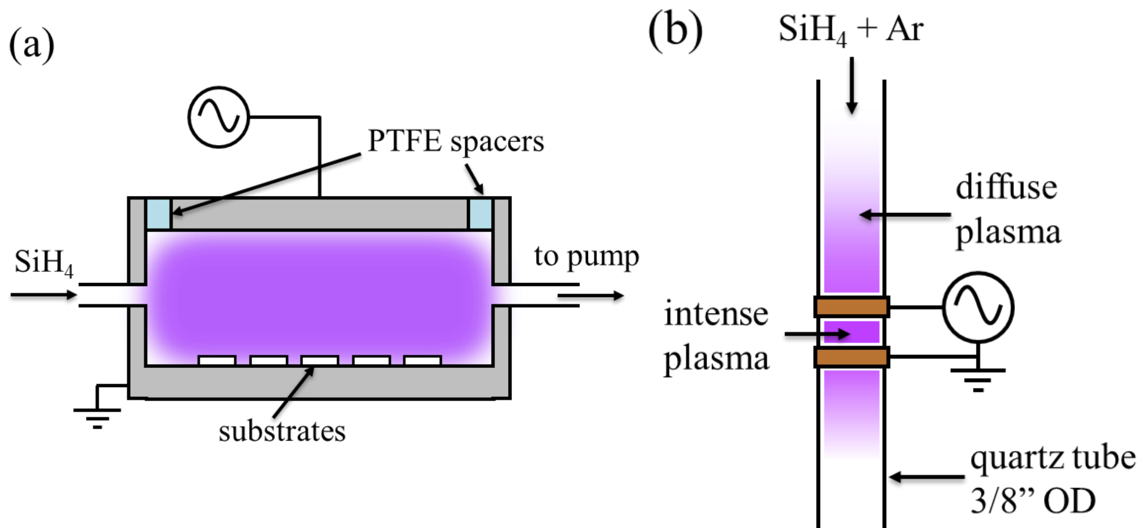

Figure 1.1**:** Cartoons of (a) a deposition chamber for a-Si:H thin films and (b) flow-through tube reactor for synthesis of nc-Si.

attracts the heavier, negatively charged silane molecules and a thin film of Si and H grows on all exposed surfaces. When the temperature of the surface is elevated to between 250 and 300°C, the quality of the resulting a-Si:H thin film is maximized [8]. These temperatures increase the mobility of each silane molecule, allowing it to "settle in" to its position relative to the already deposited Si and H atoms, and the system relaxes into a more energetically-favorable, yet still disordered configuration. Of particular importance is that the hydrogen can diffuse enough at these temperatures to passivate defects in the network of Si atoms. At too low a growth temperature there is insufficient surface diffusion of hydrogen and the defect density is increased relative to films grown at ~ 250°C. At too high a temperature, however, the diffusion of the hydrogen increases to the point that hydrogen is lost from the growing film, and there is a corresponding increase in defect density.

While not as extensively studied as amorphous silicon, hydrogenated amorphous germanium (a-Ge:H) is quite similar to a-Si:H. Thin films of high quality a-Ge:H can be fabricated using PECVD in a similar configuration to that of a-Si:H, using germane gas (GeH_4) instead of silane. For a-Si:H thin films, a higher quality, lower-defect sample is achieved by growing the film as slowly as possible. The powers used to create the silane plasma are usually the lowest possible while maintaining a stable plasma, because the deposition rate is roughly proportional to the plasma power. In a-Ge:H, however, the highest quality films are produced at high deposition rates, usually by applying large powers across the germane plasma, in a configuration similar to that sketched in Figure 1.1a [9,10]. Amorphous germanium thin films which display poor electronic properties

usually exhibit a columnar microstructure, measured via SEM, compared to high quality a-Ge:H samples which form a denser matrix [11].

1.1.2 – **Nanocrystals**

Silicon (and germanium) nanocrystals (nc-Si or nc-Ge) can be plasma-synthesized in a similar manner but require very different growth conditions than a-Si:H. In the case of nc-Si, a radio frequency power source is used at 13.67 MHz to create a plasma in a mixture of silane gas and argon, with a ratio of approximately 1:20 (SiH_4:Ar). The gas mixture is fed through a glass tube and the power source is connected to electrodes that form parallel rings around the glass tube, as in Figure 1.1b. Compared to the a-Si:H film plasma, the power and gas pressure are both increased. With sufficiently high power and pressure, the density of charged silane molecules is quite high, including SiH_3^-, SiH_2^{--} and the occasional SiH_5^+ species. These can combine to form nanoparticles, which grow for the duration of their time spent in the plasma, and are usually negatively charged.

At the same time, there are many argon ions in the plasma, which have had an electron stripped and are positively charged. When an Ar^+ ion collides with a nanoparticle, an electron is exchanged. The energy released from this exchange is equal to the ionization energy of the Ar atom, 15.8 eV, which is immediately converted to heat in the nanoparticle. The short mean free path caused by a large pressure in the nanocrystal reactor means there is a nearly constant barrage of Ar^+ ions on the surface of the nanocrystal, and the temperature of the nanocrystal is on average much higher than the surrounding gas. Upon cooling, the four-fold coordinated, over-constrained silicon nanoparticle crystallizes, rather

than forming a glass, and nanocrystals of diameter 2 – 20 nm (depending on the flow rate and RF power levels) can be fabricated in this manner [12].

1.1.3 – **Mixed-phase nc-Ge/a-Si:H**

The nc-Ge/a-Si:H films described in this thesis were grown in a dual-chamber co-deposition PECVD system [13], sketched in Figure 1.2. This system was custom-built to provide the flexibility to synthesize thin films composed of variety of different materials that would be impossible to produce in a single-chamber deposition system. In the samples investigated here, germanium nanocrystals are synthesized in an upstream nanocrystal synthesis chamber, and injected into the already-growing a-Si:H thin film. The result is a material composed of germanium nanocrystals which are dispersed and embedded throughout an a-Si:H thin film.

The nanocrystals are synthesized from a mixture of germane gas (GeH_4) and Ar, with a ratio of 1:109 (GeH_4:Ar) at a pressure of at least 4.5 Torr. The gas mixture passes through a 3/8" quartz tube, which has ring electrodes separated by 2 cm, through which 100 Watts of RF power is applied at 13.68 MHz. The nc-Ge yield can be changed by placing an orifice downstream of the nanocrystal plasma, and adjusting the overall flow rate to achieve a pressure of 4.5 Torr. For the samples presented here, the nanocrystals were synthesized using orifices from 1.5 mm to 3 mm in diameter, with total flow rates of 66 sccm to 132 sccm, where higher flow rates yielded more nanocrystals.

The amorphous silicon thin film creates a matrix surrounding the nc-Ge, and is synthesized in a separate plasma reactor, downstream from the nanocrystal plasma. The

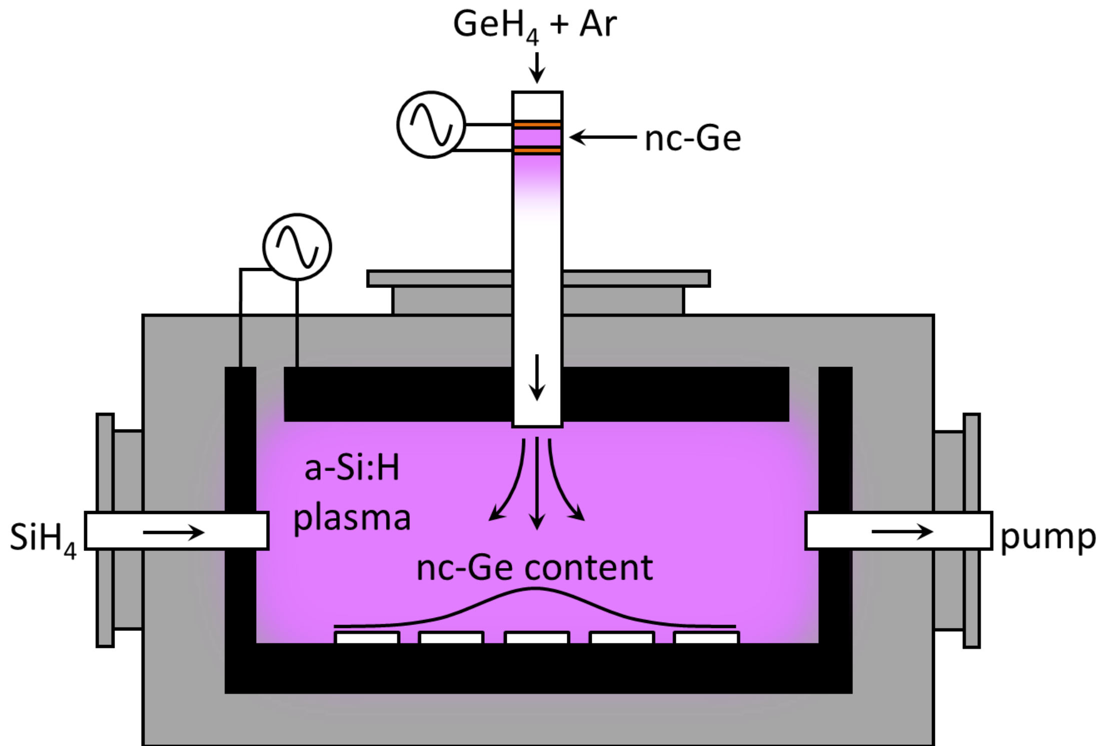

Figure 1.2: Sketch of the dual-chamber dual-plasma co-deposition system used to synthesize the nc-Ge/a-Si:H thin films. An upstream plasma fed by GeH_4 and Ar creates the nc-Ge, which are carried downstream to the film plasma, which is tuned to grow high-quality a-Si:H thin films. As the a-Si:H grows, germanium nanocrystals are embedded in the films, producing a composite material, with higher germanium content near the injection tube.

film plasma is fed by a separate gas line, which carries 2-5 sccm of silane gas (SiH_4). The plasma is created from parallel plate electrodes, 3.5” in diameter, with an RF power of 2-5 Watts at pressures around 0.25 Torr. The parameters for the film plasma were not significantly adjusted for the samples presented in this thesis; however, any residual gasses from the nanocrystal synthesis were also injected into the second plasma chamber. Accordingly, the actual film deposition conditions included 60 to 120 sccm of Ar, and any unreacted GeH_4. I will show, later, that there is no significant Ge alloying in the a-Si:H

film, indicating that either all the GeH_4 is reacted by the nanocrystal plasma, or any GeH_4 that entered the film chamber was not dissociated by the film plasma in significant quantities and passed through to the pump.

Samples were grown on Corning 1737F glass substrates, each 1.3 cm x 1.3 cm at a temperature of 250°C. Due to the relatively large inertia of the nanocrystals as they enter the film plasma chamber, the concentration of nc-Ge embedded in the a-Si:H is largest directly underneath the nanocrystal injection tube, falling from 100% in the center to 0% at the edges in some cases. In this way, it is possible to grow a series of nc-Ge/a-Si:H films in a single deposition run, where only the nc-Ge concentration is varied.

Following deposition, aluminum electrodes were evaporated on the surface of the films, parallel to the direction of the gradient in X_{Ge}. In substrates where the difference in X_{Ge} between the two ends of the substrate differed by more than a few percent, the sample was scribed perpendicular to the electrodes to divide the substrate into multiple samples of more uniform Ge concentration, as in Figure 1.3. In each deposition run, films were grown on 3 to 5 substrates, yielding from 5 to 10 distinct, measureable samples. In most cases, regions of the film where the nc-Ge concentration is over 60% begin to lose adhesion to the substrate. The material ceases to be an amorphous film with embedded nanocrystals and behaves similar to a pure nanocrystal film, such that deposition of electrodes afterwards is difficult and oxidation occurs very rapidly. Consequently, no transport measurements for samples with $X_{Ge} > 75\%$ are reported.

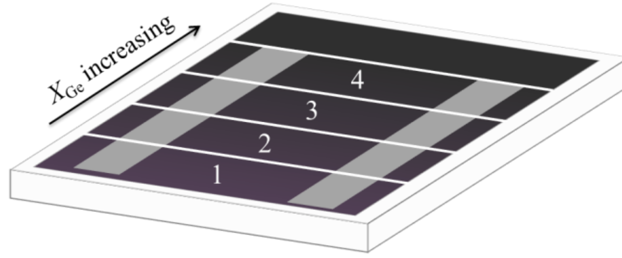

Figure 1.3: Sketch of a single substrate after preparation into 4 distinct samples. The nc-Ge/a-Si:H film is deposited on a glass square, usually with a gradient in X_{Ge}. Two electrodes are deposited parallel to the direction of the gradient, and the sample is scribed into 5 rectangles of approximately constant nc-Ge concentration. Four of these become distinct samples with relatively constant X_{Ge}. The fifth is used to monitor the temperature on either side for the thermopower measurements.

1.2 – Electronic Transport in a-Si:H

Amorphous silicon is distinguished from more conventional, crystalline semiconductors by its lack of long-range order. Crystalline silicon has a diamond cubic lattice structure, in which each silicon atom is bonded to four other silicon atoms at 109.47°, as in a tetrahedron, and the bond lengths are constant at 2.35Å. This periodicity means that it is possible to understand the properties of an entire crystal by just looking at the smallest repeating pattern, the unit cell. For silicon, the unit cell contains only eight atoms, and predictions about the optical and transport properties of the material by studying just those eight atoms have been very successful. This is done through Bloch's theorem, which leads to accurate analytical calculations of the material properties of crystalline silicon. In amorphous silicon, this periodic structure is absent. The lack of order in amorphous silicon can be manifest as a variation of the bond angle, bond length, or as a missing bond (known as a dangling bond). For an individual tetravalent silicon atom in

amorphous silicon, the variation in bond lengths very small, less than 1%, but much larger deviations are seen in the bond angle, especially in the presence of missing bonds [14].

Early studies on pure, unhydrogenated amorphous silicon found that the disorder brought about by missing bonds and variations in bond angle means that there is in fact a continuum of energy states where the bandgap should be. The density of states near the Fermi energy is quite large, so transport occurs via hopping through defect states near the Fermi energy [15]. Consequently, doping is impossible, as the high density of dangling bonds soaks up any charges donated by impurity atoms, and the Fermi energy remains pinned in the mid-gap [16]. In 1969, however, Chittick and co-workers demonstrated the deposition technique described in the previous section, which incorporates hydrogen into the amorphous silicon film, drastically reducing the defect density in the bandgap [3]. The inclusion hydrogen occupies the dangling bond sites, which helps to satisfy the valence requirements for the silicon atoms, and removes many strained Si-Si bonds, reducing states in the band tails. In hydrogenated amorphous silicon (a-Si:H) samples produced via PECVD as in Figure 1.1a, the hydrogen content is roughly 10 atomic %, meaning that a-Si:H is most accurately described as an alloy of silicon and hydrogen [18]. In a-Si:H the dangling bond density is reduced to ~ 10^{16} cm^{-3} from values as high as 10^{20} cm^{-3} in unhydrogenated a-Si, and there is a corresponding improvement in the material's optical and electronic properties.

In many ways, a-Si:H shares many characteristics with crystalline semiconductors. For example, it can be doped [19] and displays a roughly Arrhenius conductivity dependence on temperature [3]. There are notable exceptions, however, such as its anomalous Hall effect [20], incorrect Seebeck coefficient activation energy [21] and

metastable defect creation [22]. In general, those aspects in which amorphous silicon behaves like crystalline semiconductors are reflections of its short-range order, in which most silicon atoms still have tetravalent bonds. Those anomalous behaviors listed above and many more are generally the consequence of the loss of long-range order, and are determined by the interaction of large groups of atoms.

The band structure of hydrogenated amorphous silicon differs from that of crystalline silicon primarily in that there are a continuum of states at all energies within the bandgap. In any semiconductor, the treatment from Bloch's theorem on the perfect infinite crystal results in a gap around the Fermi energy where there are no available states for electrons to reside. When defects are added to the material, whether through point defects in the crystal structure or substitutional doping, energy states may become available inside the bandgap. This is the power of doping in crystalline semiconductors – by introducing defects that produce new energy states in the bandgap near the conduction band or valence band, one can shift the Fermi energy substantially, and interesting devices can be fabricated. The disorder present in hydrogenated amorphous silicon means that, rather than a gap where there are no states around the Fermi energy, there is merely a decrease in the number of states near the Fermi level, compared to higher or lower energies. The band structures of a-Si:H and crystalline silicon are sketched in Figure 1.4 to illustrate this difference. In hydrogenated amorphous silicon, conduction occurs via charge carriers hopping between states of similar energy. For energies close to the Fermi energy, the distance between nearby states is quite large, and very little current can flow through these states. These are termed defect states or midgap states, and are associated primarily with dangling-bond defects, but also with highly-strained Si-Si bonds [23]. Moving away from

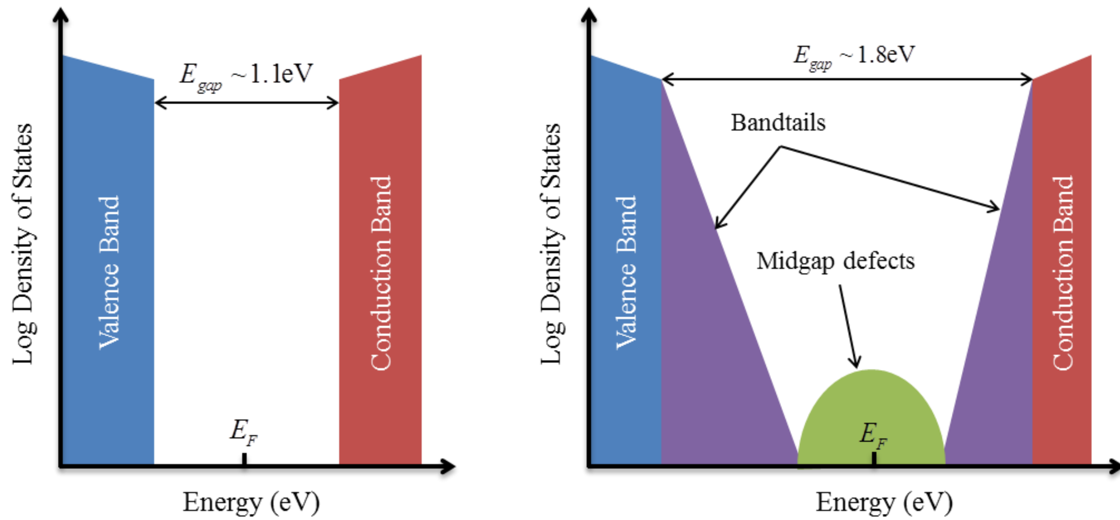

Figure 1.4**:** Sketches of the density of states for crystalline silicon (left) and hydrogenated amorphous silicon (right). The energy gap shown here for crystalline silicon is an indirect gap, and the direct bandgap is 1.4 eV.

the Fermi energy in either direction, the density of states increases exponentially. These are the bandtails, and arise from Si-Si bonds that are stretched, rotated or otherwise stressed away from their lowest energy configuration.

At some point in the bandtails, the wavefunction overlap of nearest neighbor states of similar energy becomes substantial and hopping between states is allowed. The energy at which this change occurs is termed the "mobility edge" and was predicted by Neville Mott in 1967 [24]. The vast majority of conduction through a-Si:H at temperatures above room temperature is through these 'extended' states above the mobility edge. The wavefunction overlap is sufficient that free electrons (holes) with energy above (below) the mobility edge see a continuum of states and conduct as in a metal. The total conductivity of a sample of a-Si:H is then limited by the number of electrons (holes) that are above (below) the mobility edge, which is almost completely determined by the

temperature. The tails of the Fermi function $f(\varepsilon)$ which extend past the mobility edge are exponentially dependent on the inverse of the temperature T, i.e.

$$f(\varepsilon) \sim \exp\left[-\frac{\varepsilon - \varepsilon_F}{k_B T}\right] \tag{1.1}$$

where ε_F is the Fermi energy and k_B is the Boltzmann constant. The number of electrons at any energy is just the Fermi function times the density of states, which is mostly constant above the mobility edge. Therefore, we expect that the conductivity σ will follow an Arrhenius expression when measured as a function of inverse temperature,

$$\sigma(T) = \sigma_0 \exp\left[-\frac{\varepsilon_{CB} - \varepsilon_F}{k_B T}\right] \tag{1.2}$$

where ε_{CB} is the energy of the mobility edge separating the conduction band from the bandtail states and σ_0 is a constant conductivity prefactor. In hydrogenated amorphous silicon, most researchers find that the conductivity is described by Equation (1.2), with activation energies, defined as $E_\sigma = \varepsilon_{CB} - \varepsilon_F$ between 0.8 and 1 eV [22,25–27].

Equation (1.2) is also valid for crystalline semiconductors, for the same reasons. The mobility edges in hydrogenated amorphous silicon play the role of the conduction and valence band edges in crystalline semiconductors, so any free electrons present in the conduction band must be thermally activated, and the conductivity is again limited by the overlap of the Fermi function and the conduction band.

At sufficiently low temperatures, Equation (1.2) becomes yields a very small conductivity, as there are simply too few free charge carriers in the de-localized states outside the bandgap to carry significant current. In this case, the majority of conduction through the sample can arise from electrons and holes trapped in localized defect states inside the bandgap that can tunnel from state to state, "hopping" across the sample and carrying current. This was famously predicted by Mott in 1968, called variable-range hopping (VRH), where charge carriers hop through nearby states close to the Fermi energy in a constant density of states [28]. This yields a conductivity temperature dependence given by

$$\sigma(T) = \sigma_0 \exp\left[-\left(\frac{T_0}{T}\right)^{1/4}\right] \tag{1.3}$$

The other common type of hopping seen in amorphous silicon and related materials is Efros-Shklovskii variable-range hopping, which is very similar to Mott's formulation except that it takes into account a Coulomb gap near the Fermi energy arising from charge buildup. Efros-Shklovskii VRH arrives at a similar expression for the conductivity's temperature dependence, except that the exponent in Equation (1.3) is 1/2 instead of 1/4 [29]. Both Mott and Efros-Shklovskii VRH have been observed in a variety of disordered semiconductors, generally at very low temperatures [30,31].

Compared to conduction through de-localized states, variable-range hopping yields much less current per charge carrier. In unhydrogenated amorphous silicon (a-Si) thin films, for example, the density of dangling bond states in the center of the bandgap is very large ($\sim 10^{20}$ cm^{-3}). In these materials, electronic conduction is dominated by hopping

through states near the Fermi energy, simply on account of the sheer number of occupied states given by the product of the density of states and the Fermi function. Measurements of the temperature dependence of the conductivity confirm that electronic transport through these films is described by variable-range hopping through dangling bond states [32].

1.3 – Thermoelectric Effect

The thermoelectric effect, also known as the thermopower or Seebeck effect, is a method of measuring the entropy per unit charge in a material. To first order, one can approximate the free charge carriers in any material as an ideal gas. When a temperature gradient is applied across a sample, it induces motion of free charge carriers by diffusion from the hot end towards the cold end of the sample. In a sample with only free electrons, the electrons begin to accumulate at the cold end and a voltage difference is created across the sample with a negative potential at the cold end. The resulting electric field repels the electrons back towards the hot end, counteracting the diffusion of more electrons, and the sample quickly reaches a steady-state voltage. In an open-circuit configuration, the Seebeck coefficient S is defined as the negative voltage induced per degree of temperature gradient,

$$S = -\frac{dV}{dT} \tag{1.4}$$

Because a temperature gradient, which is insensitive to charge, induces the motion of the charge carriers, it is possible to determine the sign of the majority charge carrier from the sign of the Seebeck coefficient, where a negative (positive) S means that electrons (holes) are the majority charge carrier.

The simple treatment of charge carriers as a gas is convenient for understanding the sign of the Seebeck coefficient, but it doesn't provide much insight into the magnitude of *S*, nor is it particularly accurate for semiconductors and insulators, in which the mean free path of each charge carrier is much too short to approximate as an ideal gas. In a lightly n-doped semiconductor, the Fermi level is above the center of the bandgap and there are many more free electrons than holes. When a temperature gradient is applied across the sample, the Fermi function is broader at the hot end, resulting in more filled states above the Fermi level and more empty states below the Fermi level, compared to the cold end. When an electron is thermally promoted to higher energy in the presence of a temperature gradient, it sees more empty states at similar energies in the direction of the cold end, and fewer towards the hot end. This promotes diffusion towards the cold end, in which each diffusion event from a thermally-activated charge carrier will quickly end in phonon scattering and dissipation in the form of heat. Those conduction band electrons will fill lower energy states closer to the cold end, and the thermal excitation → diffusion → scattering process causes an overall drift of charge carriers towards the cold end.

In intrinsic or compensated semiconductors that have both conducting electrons and holes, the sign of the thermoelectric voltage depends primarily on the mobility of the charge carriers. In a-Si:H, the mobility of electrons in the conduction band is around ten times the mobility of holes in the valence band, and undoped a-Si:H has a negative thermopower [33]. The sign of the thermopower can also depend on the slope of the density of states near the Fermi energy, especially in materials with very few free electrons or holes in the conduction and valence bands. If the density of states is larger above the Fermi energy than below, electrons will have more options for diffusion via Fermi's Golden Rule,

and the electron voltage will be larger than the hole voltage. This can be seen in unhydrogenated amorphous silicon, in which there is a very large defect concentration and the motion of charge carriers occurs only via hopping through defect states near the Fermi energy. The Seebeck coefficient is then very sensitive to the slope of the density of states at the Fermi energy, and can be either positive or negative, depending on the midgap defect state energy densities and the position of the Fermi energy.

The Seebeck coefficient is largest for materials with a single dominant charge carrier, because the minority charge carrier produces an additive voltage of the opposite sign, but its magnitude is also dependent on the bandgap and Fermi energy of the material. A large bandgap means that more energy is transferred per charge carrier, which directly translates to a larger voltage. Usually, semiconductors have the largest Seebeck coefficients, because the energy per charge carrier is small in metals, and insulators have so few charge carriers.

A growing application of the Seebeck effect is in devices termed thermoelectrics. These are materials that generally have very large thermopowers, and can drive a useable current from a temperature gradient or create a temperature gradient from an applied voltage. Thermoelectrics have great technological promise, as they can be used to harvest waste heat from any heat-generating process and turn it into immediately useable electricity, and they can be used for refrigeration with no moving parts [34]. Thermoelectrics are a nascent field, however, and have not gained widespread adoption outside of some niche markets due to their relatively high cost and low efficiency. The efficiency of any thermoelectric material can be expressed by the Figure of Merit zT, defined as

$$zT = \frac{S^2 \sigma T}{\kappa} \tag{1.5}$$

where T is the temperature, σ is the electrical conductivity and κ is the thermal conductivity [35].

The Figure of Merit is a very interesting combination of metrics, as it is largest when S and σ are both large and κ is small, meaning the material should have the conductivity of a metal, the thermopower of a semiconductor, and the thermal conductivity of an insulator. Put another way, one wants many charge carriers that each carry a lot of energy but very little heat. In most cases the materials with largest zT are heavily-doped semiconductors to achieve large σ and relatively large S, with added heavy-atom impurities to disrupt thermal conduction through the lattice, caused by phonons [36].

1.4 – Photoconductivity of a-Si:H

When light is absorbed by a-Si:H, the conductivity can increase, owing to an increase in charge carriers from the generation of electron-hole pairs. The excess conductivity is termed the photoconductivity, σ_{ph} and is determined by the product of the photo-excited charge carrier generation rate G, the recombination lifetime τ_{rec}, the electron charge, and mobility μ. Over prolonged exposure times of a few hours or more, the photoconductivity gradually decreases. Once the light is turned off, the dark conductivity of a-Si:H does not return to its original value, but rather assumes a significantly smaller value. The sample can be returned to its original state by annealing at elevated temperatures

of 450 K or so for around 30 minutes or more. To distinguish between the dark conductivity before and after light exposure, the terms “state A” and “state B” are used, respectively.

The origin of the decrease in dark conductivity in state B, known as the Staebler-Wronski Effect (SWE), is not completely understood, but most theories suggest that it is related to the presence of hydrogen in the amorphous silicon matrix [37–39]. The hydrogen atoms in a-Si:H passivate bonds with Si atoms that would otherwise have no partner, known as “dangling bonds.” In the band structure of a-Si:H, dangling bonds are associated with energy states in the middle of the bandgap. These midgap states are the primary sites where the recombination of electron-hole pairs occurs. In one proposed model for the microscopic physics of the SWE, if a photon is absorbed near a Si-Si bond that is sufficiently strained, the Si-Si bond may break, creating two dangling bonds. Usually, the Si-Si bond would quickly reform, but a nearby hydrogen atom, which is quite mobile within the sample near room temperature, may move into the region of the broken bond and passivate one of the newly-broken Si bonds. Now, the two remaining unpaired Si bonds are too far apart to create a bond between them, and the number of dangling bonds has increased. Upon annealing, hydrogen diffusion brings these light-induced dangling bonds in close proximity, and they can then disappear by reforming a Si-Si bond. Other models have been proposed to account for the origin of the SWE, involving the trapping of charges or the breaking of Si-H bonds [40,41].

In the context of a useful a-Si:H solar cell, an increase in the number of dangling bond defects, and therefore the recombination rate, greatly decreases its efficiency, as in this case the photo-generated electrons and holes are less likely to reach the electrodes,

decreasing the useful current produced by the device. For this reason, researchers have focused on mitigating the SWE in amorphous silicon since its discovery in 1977.

There are a number of approaches that have been investigated in the hopes of minimizing or even eliminating the SWE in amorphous silicon. It has previously been shown that decreasing the amount of bonded hydrogen in the a-Si:H can improve the resistance to metastable light-induced conductivity changes. For example, deposition of a-Si:H using the hot wire technique yields a material with a lower percentage of bonded hydrogen, around 1 at. % (compared to 8-10 at. % for PECVD a-Si:H), and improved metastable light-induced conductivity changes [18,42].

In recent years, there has been interest in creating composite structures based on a-Si:H to mitigate the SWE. Previously, it has been shown that embedding silicon nanocrystals in a-Si:H can lead to improved dark conductivity, as well as a decrease in the magnitude of the SWE following extended illumination [43].

– Chapter 2 –

Characterization Techniques

This chapter focuses on measurement techniques that will be used to characterize the materials presented in this thesis. In particular, I emphasize here the physics behind the measurements, in addition to the technical logistics of how the measurements were performed. I begin with structural measurements, used to understand the composition of the materials, including the ratios of different phases in a composite material and the amount of disorder present in a uniform film. The second section describes the methods used to determine the electronic transport properties of these materials.

2.1 – Structural Characterization

2.1.1 – **Raman Spectroscopy**

Raman spectroscopy is a technique that analyzes the inelastic scattering of monochromatic light. A monochromatic laser is incident on the sample and the vast majority of the photons are scattered elastically via Rayleigh scattering, departing with the same energy and wavelength as the incident photons. A small fraction of the incident photons interact with the bonds between atoms, exciting their vibrational modes. Raman scattering is contrasted with absorption of a photon in that absorption requires a permanent electric dipole moment, whereas Raman scattering has no such requirement. A dipole moment is induced by the incident EM field of the light, which allows observation of symmetric (Si-Si or Ge-Ge) vibrational modes that are unavailable in absorption

measurements. The spectra presented in this thesis will focus on stretching modes involving Si and Ge atoms, but other modes (wagging, rocking, etc) can also be excited by Raman scattering.

The scattered energy of a photon can be either smaller or larger than the incident energy, corresponding to Stokes and anti-Stokes Raman scattering, respectively. The magnitude of the energy shift is sensitive to the atomic masses in the bonds as well as the strain and disorder in the lattice structure. This means that Raman spectra can be used to determine the relative concentrations of different atoms and different phases in a sample. In this work, Raman spectroscopy will be used primarily to determine the relative concentration of germanium nanocrystals in the nc-Ge/a-Si:H thin films. Because it can distinguish between crystalline and amorphous phases of the same elements in a material, Raman will also be used to establish the amount of amorphous germanium, Si-Ge alloying, and nanocrystalline silicon that could, in principle, be present in the nc-Ge/a-Si:H samples.

The energy shifts in Raman scattering are usually reported in units of wavenumber (cm^{-1}), mostly for historical reasons, and in this thesis, I will only look at the Stokes Raman scattering, in which the photons lose some energy in order to excite a vibrational mode in the solid. In single crystals, the Raman spectrum consists of a single, very sharp peak at a single energy. For crystalline silicon, the one signature peak is observed at 520 cm^{-1}, and for crystalline germanium, a corresponding peak is found at 300 cm^{-1}. In these crystals, a single peak is observed because the photons have very little momentum (k) to impart to the crystal structure, compared to a phonon. Momentum is conserved during Raman scattering and due to the dispersion relations and band structures in c-Si and c-Ge, there is only a

single phonon mode that can be activated while maintaining momentum conservation, the $k = 0$ point in the transverse optical (TO) mode.

In amorphous silicon, however, the lack of long-range order relaxes the requirement of momentum conservation. Any phonons that are activated can effectively “borrow” momentum from the nearby defects and strained bonds, a feature that isn’t available to single-crystals. This is reflected in a band of allowable phonon energies, corresponding to a band in energies of the scattered photons that are detected, with each band appearing as a broadened, Gaussian peak. A second consequence of the lack of long-range order in amorphous silicon is that, in addition to the TO mode, the other, non-*k*-conserving phonon modes can be activated during Raman scattering: transverse acoustic (TA), longitudinal optical (LO), or longitudinal acoustic (LA). As a result, the total Raman signal from the Si-Si bonds in amorphous silicon is composed of multiple Gaussian peaks, one from each population of phonon modes. The peaks for the TO, LO and LA modes all overlap somewhat, centered at 480 cm^{-1}, 410 cm^{-1} and 320 cm^{-1}, with widths approximately 55 cm^{-1}, 65 cm^{-1} and 85 cm^{-1}, respectively. The peak corresponding to the TA mode is found at 175 cm^{-1} with a similar width to the other peaks. However, the detector used to measure the Raman spectra presented here was filtered to remove the huge Rayleigh signal at low energies. Consequentially, only the higher-energy tail of the TA peak is visible in the spectra presented here, and analysis of the TA peak is ignored.

A sample Raman spectrum for a hydrogenated amorphous silicon thin film is shown in Figure 2.1. The total measured spectrum is decomposed into four separate peaks, each corresponding to a different phonon mode. Because of the overlap of the TO,

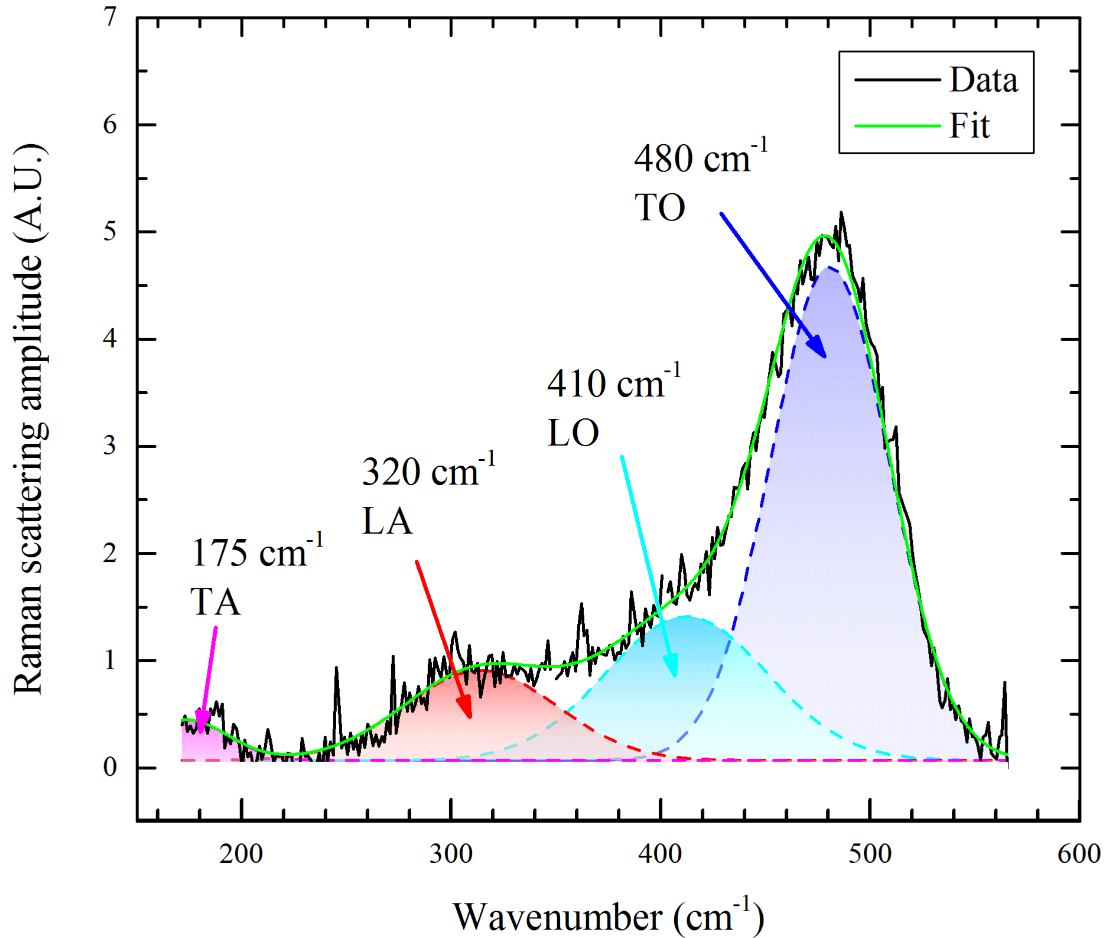

Figure 2.1**:** Raman spectrum of a pure a-Si:H thin film (black). The total measured spectrum can be decomposed into four separate Gaussian peaks, centered at 480 cm^{-1} (blue), 410 cm^{-1} (cyan), 320 cm^{-1} (red), and 175 cm^{-1} (magenta), shown as dotted lines. The sum of these four peaks is shown by the solid green line.

LO and LA modes, many different fits can accurately describe the data, where the widths, positions and heights of each peak vary considerably. In some Raman fits, the mathematically best fit involved characteristics which were clearly unphysical, most commonly a very large LO peak shifted up to ~ 430 cm^{-1}. In this case, the TO peak height is reduced, and its center is shifted up to 490 cm^{-1} or so. In this and similar case, the difference in quality of fit between the mathematically best fit and a more constrained,

physically consistent fit is almost always vanishingly small, so the constrained fit is preferred.

The measured Raman spectrum for nanocrystals resembles a mixture between the single-crystal and amorphous signals. As the nanoparticles are crystalline, there is still a momentum conservation requirement, but their long-range order ends at the surface of the nanocrystal. This leads to a slight relaxation in the requirement of momentum conservation when compared to single-crystals. The immediate implication of this is that the non-momentum conserving phonon modes are partially accessible, all of which are at lower energies than the single-crystal TO $k = 0$ mode in Si and Ge, so the resulting nanocrystalline peak is shifted to lower energy. A secondary effect is that the nanocrystalline Raman signal is broadened asymmetrically, with a larger tail at lower energies, reflecting the inclusion of the lower energy LO, LA and TA modes [44–46].

In silicon nanocrystals, the position of the Raman peak is dependent on the size of the nanocrystals, where smaller nanocrystals have a peak shifted to lower energies, usually between 510 and 515 cm^{-1}. However, the position of the peak is also quite sensitive to other characteristics of the nanocrystals, including stress [47] and surface states [48], which can cause similar shifts. It is therefore more reliable to use a separate characterization technique to determine the size of the nanocrystals, such as X-ray diffraction.

For germanium nanocrystals, while the body of literature is sparser than for nc-Si, there is still some correlation between the position of the Raman peak and the size of the nanocrystals. The amorphous germanium Raman spectrum is reminiscent of the amorphous silicon spectrum, with the TO mode at 278 cm^{-1}, the LO mode at 233 cm^{-1} and

the LA mode at 175 cm^{-1} [49], and indeed the nc-Ge Raman peak is usually shifted to lower energies from the single-crystal Ge peak at 300 cm^{-1} [46]. However, for very small germanium nanocrystals, less than 5 nm in diameter, the position of the Raman peak can actually back up to higher energies, and even reach higher energy than the single-crystal peak [50].

The Raman data presented in this thesis were all collected using a Witec Alpha 300R confocal Raman microscope located in the Characterization Facility (CharFac) at the University of Minnesota. It used an argon-ion 52 laser at 514.5 nm focused to a spot size of ~ 2-3 μm and the detector was an UHTS 200 spectrometer. The power of the laser was kept below 6 mW in order to minimize local heating of the sample, which can cause the locations of the peaks to shift to lower wavenumbers by a few cm^{-1}.

2.1.2 – **Fourier Transform Infrared Reflectometry (FTIR)**

FTIR is an optical technique that measures the absorption of light in the infrared range. Absorption can occur when a photon's energy matches the vibrational energy of an atomic bond in the sample. The energy of a vibrational mode depends primarily on the atoms involved and the type of vibration (stretching, wagging, rocking, etc.). For example, in a-Si:H thin films, absorption is seen at 2000 cm^{-1}, which corresponds to the stretching of Si-H bonds when the other 3 bonds on the silicon atom are Si-Si bonds [51,52]. Because the oscillator energy may depend on the local environment around the absorbing bond, it is often possible to distinguish between, for example, the Si-H stretching mode above and a $Si\text{-}H_2$ stretching mode, where the silicon atom is bound to two hydrogen and two silicon atoms. An absorption peak is found at 2090 cm^{-1} corresponding to the $Si\text{-}H_2$ stretching

mode [53], but it has also been related to the Si-H stretching mode in the vicinity of many other Si-H bonds, for instance, at the surface of a silicon nanocrystal [54].

From classical electrodynamics, absorption or emission of a photon can occur with a changing dipole moment. For this reason, only vibrational modes that present a change in the net dipole moment can be detected through infrared absorption. For example, a Si-H bond has a nonzero dipole moment due to the different electron distributions of the Si and H atoms. When the bond stretches or bends, the dipole moment changes. This bond can be measured with FTIR and is considered IR-active. For a Si-Si bond, however, the symmetry in electron distribution means that there is no net dipole moment, and as that bond stretches or bends, there is no change in the dipole moment so the bond is IR-inactive. In general, bonds between two different elements are usually IR-active; symmetrical bond are IR-inactive and are typically probed using Raman spectroscopy.

In a-Si:H thin films, the Si-H stretching modes are used to probe the disorder in the material. Conventionally, the ratio between the integrated area of the 2090 cm^{-1} peak to the 2000 cm^{-1} peak is used to characterize the amount of disorder present in a-Si:H, defining the structure factor

$$R = A_{2090} / \left(A_{2090} + A_{2000} \right) \qquad (2.1)$$

where A_n is the integrated area of the Gaussian profile corresponding to the peak centered at n. Under this definition, larger R values indicate more disorder in the amorphous silicon thin film. Figure 2.2 shows a fit to an FTIR spectrum for a pure a-Si:H thin film.

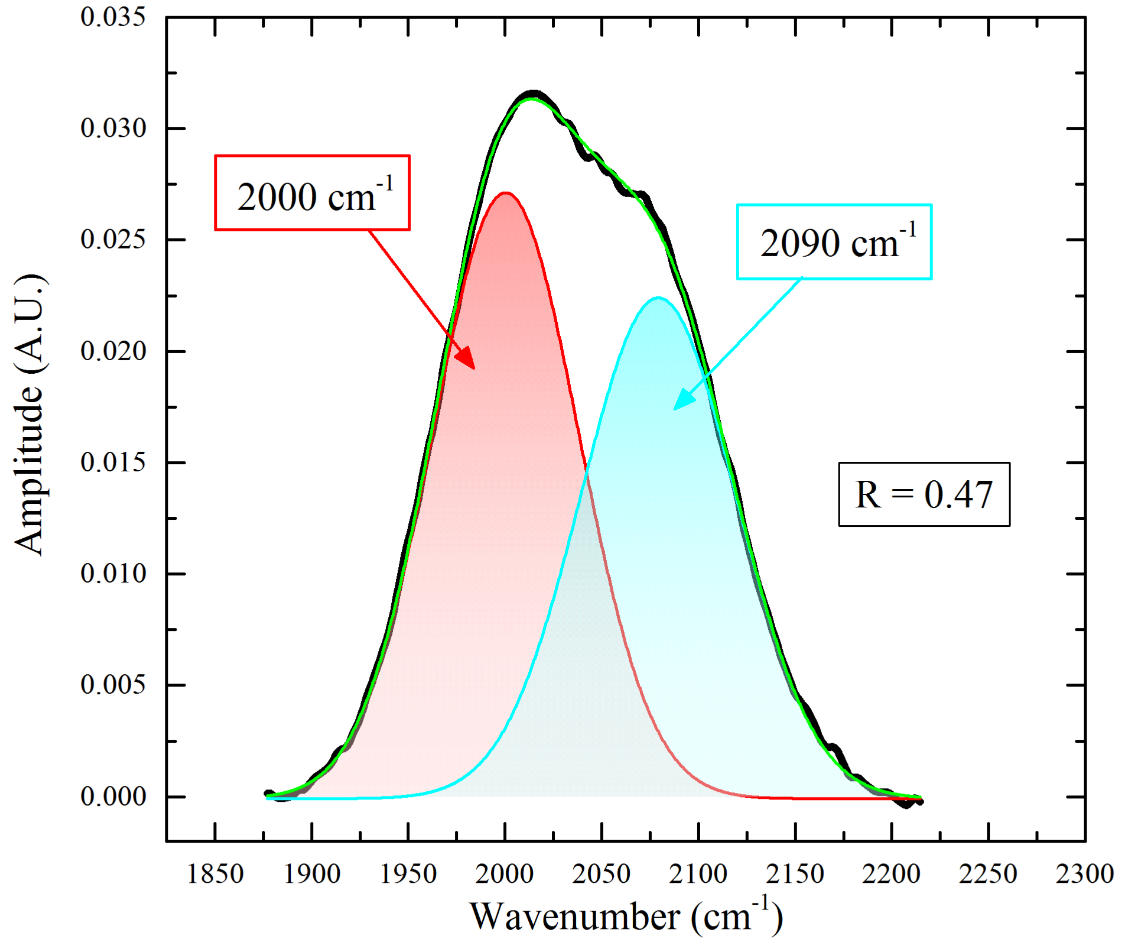

Figure 2.2: Measured absorption via Fourier Transform Infrared Reflectometry on a pure hydrogenated amorphous silicon sample (black), zoomed in to show the Si-H vibrational modes. The total fit (green) is composed of two Gaussian peaks, one at 2000 cm^{-1} (red) and another at 2090 cm^{-1} (cyan), corresponding to Si-H and Si-H_2 bonds, respectively. The level of disorder present in the film is characterized by $R = A_{2090} / \left(A_{2090} + A_{2000}\right)$, which is 0.47 for this sample.

In hydrogenated amorphous germanium thin films, the Ge-H and Ge-H_2 stretching modes, analogous to the 2000 and 2090 cm^{-1} modes in a-Si:H, occur at 1870 and 1980 cm^{-1}, respectively [55]. Because the width of all these peaks in a-Si:H and a-Ge:H are on the order of 50 cm^{-1}, it is impossible to distinguish the Ge-H_2 and Si-H modes in hydrogenated

materials that contain both Si and Ge, such as amorphous Si-Ge alloys and the nc-Ge/a-Si:H composite films studied here.

2.1.3 – **Rutherford Backscattering (RBS)**

Rutherford backscattering is famous for its role in discovering the nucleus. A beam of positively charged ions (typically alpha particles, He^{++}) is directed at sample, and the ions are repelled by the positively charged nuclei in the sample and scattered at a wide range of angles. Those ions that are scattered close to 180 degrees are collected in the measurement. The ions in the incident beam are all at a uniform energy, but the scattered ions lose energy via interactions with the atoms in the sample. The cross-section of each nucleus is very small, so the ions can penetrate quite far before being backscatttered. As the ion bores deeper into the sample, it loses energy via shallow-angle scattering with the electron clouds of the atoms it passes until it is finally backscattered by a heavier nucleus. The amount of energy lost depends on how far into the sample it travelled before being backscattered, the "stopping power" of the atoms it passed on the way, and the charge and mass of the nucleus that backscattered it. The stopping power of an atom is determined by its electron distribution, and is usually found experimentally for each element. Using the known stopping powers of different materials, it is possible to use the measured energy distribution of the backscattered ions to find the ratio of different elements in the sample. In practice this is done by running a simulation of the experiment with the compositions and thicknesses of both the sample and substrate, calculating the resulting distribution of energies, and then iteratively modifying the model to match the measured data.

An RBS measurement detects the energy of each backscattered ion, and produces a histogram of the number of ions found at each energy. Because the probability of backscattering from a nucleus in a homogenous material is nearly constant throughout its thickness, an RBS spectrum exhibits plateaus that correspond to each element present in the sample. Figure 2.3 displays the RBS spectrum of a bare glass slide. The ions elastically collide with the nuclei in the sample, so ions that were backscattered by nuclei with large mass lose very little energy, and the plateaus corresponding to those nuclei extend to higher energies. The highest-energy edge of each plateau corresponds to nuclei at the front surface

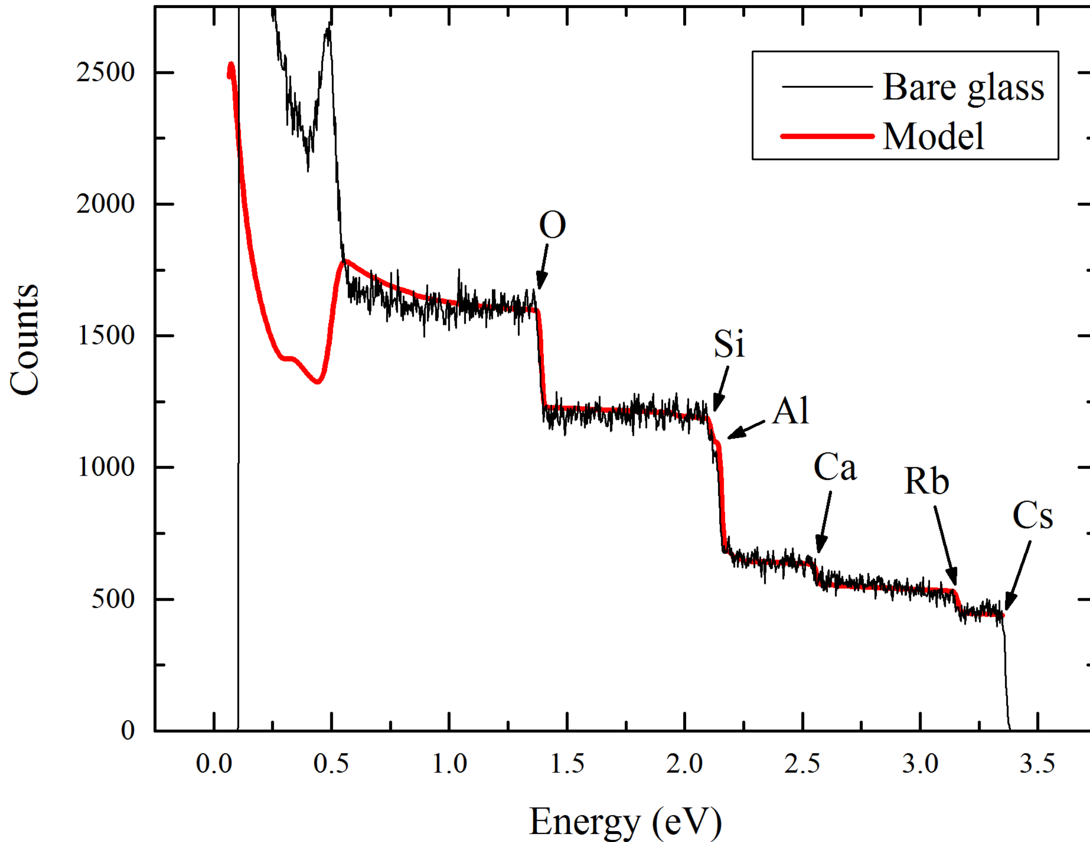

Figure 2.3: Rutherford Backscattering measurement (black) and matching simulation (red) for the bare glass used as a substrate for the nc-Ge/a-Si:H samples presented in this thesis.

of the sample, while the lowest-energy edge of each plateau corresponds to nuclei at the back surface of the sample. Because the glass is thick (1 mm), each plateau in Figure 2.3 extends all the way to zero energy, meaning that the total stopping power of the sample was larger than the energy of the incident ions. For energies below ~0.5 MeV, the simulation does not accurately match the measurement. This is a consequence of inelastic, non-Rutherford scattering events with lower Z nuclei (including Si, O and H) which are detected in the measurement but not taken into account in the simulation.

2.1.4 – **X-Ray Diffraction**

In X-ray diffraction spectroscopy, the lattice structure of a crystalline sample is used as a diffraction grating for incident photons of uniform energy. As the size of the unit cell of most solids is on the order of a few Angstroms, diffraction will be strongest and easiest to measure when the wavelength of the photons is similar or slightly smaller than the atomic spacing, necessitating the use of X-rays. When a beam of coherent X-rays are incident on the crystal, the lattice planes create a reflecting surface; however, the X-rays can penetrate many layers before being reflected as they interact weakly with the atom's electrons. The beam of reflected X-rays, as it exits the sample, can experience constructive or deconstructive interference when the angle of reflection θ, the lattice spacing d and the wavelength λ satisfy the Bragg relation,

$$n\lambda = 2d\sin\theta_B \tag{2.2}$$

for constructive interference and

$$\frac{(n+1)}{2}\lambda = 2d\sin\theta_B \tag{2.3}$$

for destructive interference, where n is an integer. In a sample that is a single crystal, multiple angles of incidence are probed and a "spot" is detected where the constructive interference condition is met. In samples that are not a single crystal, for example, a powder of nanocrystals that are all randomly oriented, there are always some nanocrystals that are in the proper orientation to satisfy the Bragg relation for any incident angle. Of the nanocrystals for which $\theta = \theta_B$, their orientations in the ϕ direction can take any value, meaning the constructive interference "spot" is now smeared into a ring, concentric with the incident beam. During analysis, the measured spectrum is integrated over ϕ to show the constructive interference peaks at different scattering angles θ.

In crystals that are very small, the peaks broaden, and this broadening can be used to determine the size of the crystal in the direction of the relevant lattice plane. For the angle θ_B satisfying the Bragg relation, the first-order constructive interference condition occurs when the path length difference between X-rays scattered from adjacent planes is λ. The non-Bragg scattering of X-rays at an incident angle θ_D which is slightly smaller than θ_B, such that the path length difference for adjacent planes is 1.1λ is sketched in Figure 2.4. An X-ray that is reflected from lattice plane 1 will almost constructively interfere with an X-ray reflected off lattice plane 2. Destructive interference occurs from X-rays scattered farther away, in plane 6, where the path length difference is 5.5λ, satisfying Equation (2.3) . For a crystal that is very small, around 2-3 lattice planes in this case, the destructively interfering X-rays are not found, and there will be some net constructive interference

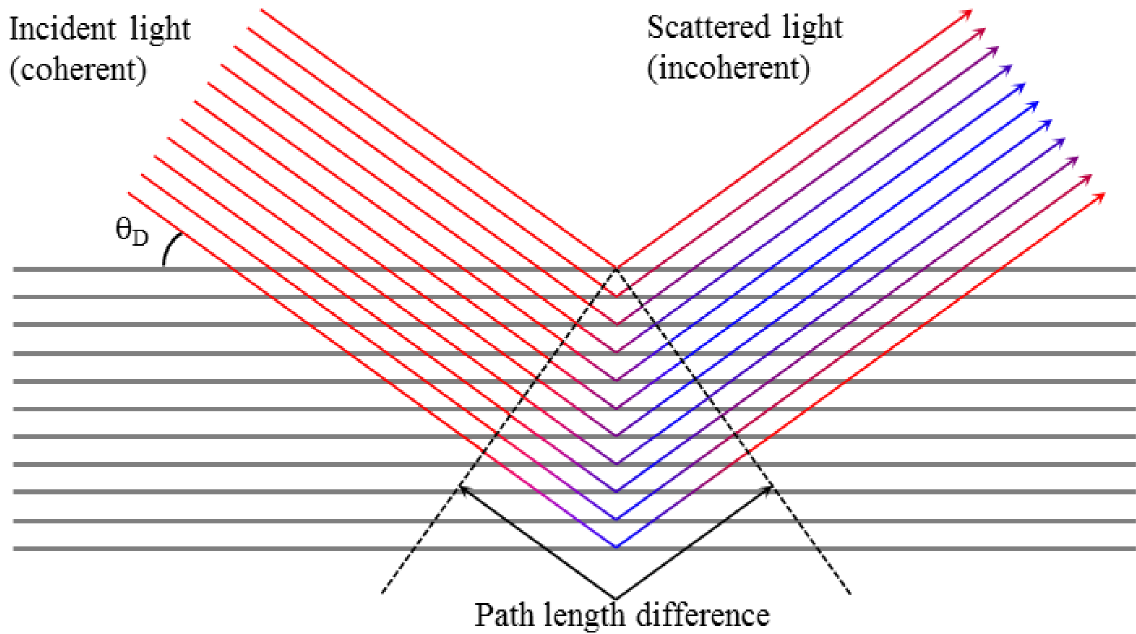

Figure 2.4: Cartoon illustrating the origin of nonzero X-ray diffraction peak widths in nanocrystals. Coherent X-rays are incident at an angle θ_D slightly smaller than the angle θ_B, which satisfies the Bragg relation, such that the path length difference between adjacent planes is 1.1λ, slightly longer than in the simple Bragg case. The phase of X-rays scattered off each plane, relative to the top plane, is denoted by the color of the line, where red lines are in phase and blue lines are out of phase. In this case, X-rays scattered 6 lattice planes away destructively interfere, and X-rays scattered off the adjacent plane interfere nearly constructively.

measured at θ_D. For incident angles much closer to θ_B, larger crystals can experience this partial constructive interference, and this leads to the broadening seen in the Bragg peaks. The nanocrystal size, δ, can be calculated from the width of the peaks, β, using the Scherrer equation [56]:

$$\delta = \frac{\lambda}{\beta \cos\theta} \tag{2.4}$$

The detected peak of scattered X-ray intensity is also broadened by the limitations of the instrument. This minimum peak width is evaluated by measuring the peak width of a single-crystal sample of corundum, Al_2O_3, which has negligible natural linewidth, and the instrument broadening is subtracted from the total breadth of the signal to isolate the broadening due to nanocrystal size. The XRD data presented in this thesis were collected using a Bruker-AXS Microdiffractometer with 2.2 kW sealed Cu X-ray source at λ = 1.5418 Å.

2.1.5 – **Profilometry**

Profilometry is a technique in which a probe is dragged very lightly across the surface of the sample and the vertical movement of the probe is measured to determine the shape or profile of the sample's surface. The substrates of each sample presented here were partially masked before deposition to create a sharp edge in the film, the height of which is the film's thickness. By directing a profilometry scan normal to that edge, passing from bare glass to the sample surface, an accurate measurement of the film's thickness can be made. The nc-Ge/a-Si:H samples showed significant correlation between X_{Ge} and thickness, averaging around 1.1 μm for samples with $X_{\mathrm{Ge}} < 10\%$ and increasing by a factor of 3-8 for samples with $X_{\mathrm{Ge}} > 25\%$.

2.2 – Electronic Characterization

2.2.1 – **Conductivity**

The simplest and most common transport measurement is the conductivity as a function of temperature. On the surface of the sample, two chromium or aluminum

electrodes are evaporated in a coplanar configuration. The length L of the electrodes are up to 1 cm, 500 nm thick, and the separation W between the two electrodes is between 0.5 and 4 mm. Electrical contact is made with the electrodes by securing the end of a thin, bare wire to each electrode with silver paint. Ideally, the silver paint acts only as a binding agent and current flows directly from the electrode to the wire. Poor electrical contact often leads to non-Ohmic transport; all samples were tested for linear current-voltage curves before any other measurements were made. At a given temperature, the current I is measured at a constant voltage V, and the conductivity is given as

$$\sigma = \frac{I}{V}\frac{W}{Ld} \tag{2.5}$$

where d is the thickness of the film.

The majority of the dark conductivity measurements presented in this thesis were performed under vacuum in a closed-cycle cryostat sketched in Figure 2.5. The sample stage consists of a partially gold-plated copper block with an embedded cartridge heater. The sample stage is separated from the cryostat's cold head by a sapphire crystal, which has a low thermal conductivity to allow the sample stage to reach temperatures up to 470 K. At very low temperatures, however, the thermal conductivity of the sapphire is large enough to cool the sample stage to 10 K. The temperature of the sample is monitored by a Si diode mounted next to the sample on the sample stage (T_Sample). A second sensor is placed near the heater to provide an input for the temperature controller (T_Control).

Conductivity measurements reported in this thesis were all performed in a two-probe configuration. A DC voltage of up to 100 V was applied across the sample and the

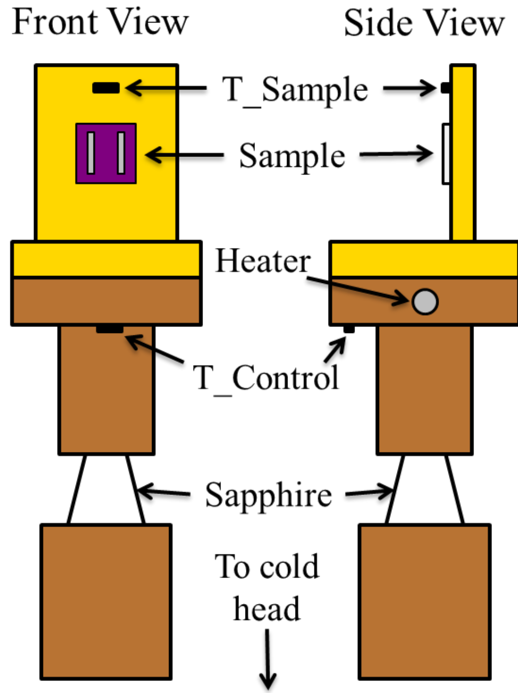

Figure 2.5: Cartoon of the sample stage in the closed-cycle He cryostat used for conductivity measurements presented in this thesis. The sample is attached to the stage using thermal grease, and electrical connection is made to the electrodes on the sample surface. The temperature sensor labeled "T_Control" is used by the temperature controller along with the heater to control the temperature of the stage. The sensor labeled "T_Sample" gives the temperatures reported in the data in this thesis. The sample can reach temperatures up to 470 K and is thermally separated from the cold head, which is always below 70 K, by a sapphire crystal.

current was measured by a femto-ammeter. Because the samples presented here are all undoped and very resistive, with resistances between 1 GΩ and 100 TΩ, any contact resistances that may be present at the interfaces between the sample and electrodes are orders of magnitude smaller, and negligible in our final current measurements.

2.2.2 – Thermopower

Thermopower measurements presented in this thesis were performed in a custom-made measurement system. Inside a vacuum chamber capable of reaching < 5 mTorr, the sample is placed across two separate copper blocks (H_1 and H_2 in Figure 2.6) such that the electrodes are directly above and parallel to the direction of the copper blocks. The copper blocks are separated by 4 mm, and the electrodes on each sample presented here also have a separation of 4 mm. Inside of each copper block, a 50W cartridge heater is embedded. The temperature of each block is controlled independently by a dual-channel temperature controller, using platinum resistors (T_3 and T_4) attached to glass slides on each copper block as input sensors. The temperatures of the blocks T_3 and T_4 are set so that the average is $T_{avg} = (T_3 + T_4)/2$ and the temperature gradient $\Delta T = T_1 - T_2$ is measured using the sample temperatures rather than the control temperatures T_3 and T_4. The temperature gradient induces a thermoelectric voltage ($V_1 - V_2$ in Figure 2.6) across the sample. For each average temperature, thermal gradients of $T_3 - T_4 = \pm 12$ °C and 0 are generated and the respective induced voltages are recorded, eliminating contributions of any small temperature-dependent voltage offset to the signal [21]. Temperature stability is maintained within ±0.05K of the target set temperatures for at least 90 seconds before collecting data. The entire measurement system is capable of measuring the electrical properties of high impedance thin films down to $\sigma \sim 10^{-8}\ \Omega^{-1}\text{cm}^{-1}$ and resides in a vacuum chamber [21]. The measured Seebeck coefficient is derived from the slope of the resulting linear plot of induced voltage against ΔT, and the process is repeated at a new average temperature, from 350K to 450K.

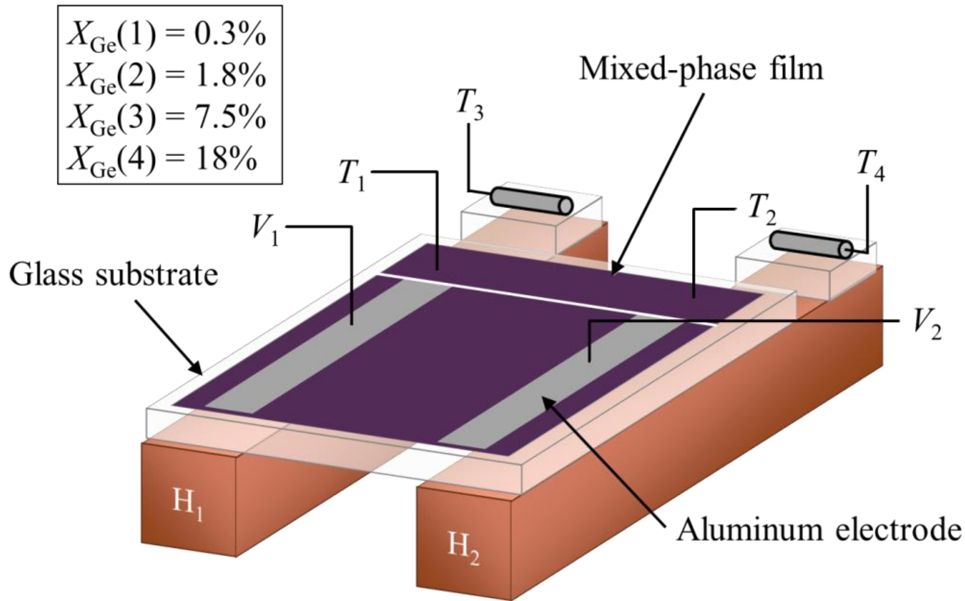

Figure 2.6**:** Sketch of the sample holder for thermopower measurements. The sample is placed so the electrodes are parallel to and atop two copper blocks, which each have an embedded heater (H1 and H2). The temperatures at each block are independently controlled using platinum resistors T_3 and T_4 as input sensors; these platinum resistors are mounted on glass slides so that their temperatures are similar to the sample temperatures. Thermocouples T_1 and T_2 are attached in a region that is electrically isolated from the measurement of V_1 and V_2, and are used in calculations of the Seebeck coefficient.

2.2.3 – **Photoconductivity**

Photoconductivity measurements were performed in a system similar to the closed-cycle system described in Section 2.2.2, though without the low temperature capabilities. The measurement system consists of a copper block with an embedded cartridge heater, upon which resides the sample. A thermocouple is attached to a piece of glass mounted on the copper block next to the sample, so that the measured temperature is close to the sample temperature and is used as both the input for the temperature controller and the sample temperature. The entire system resides in a vacuum chamber with a window that filters

infrared frequencies, to minimize sample heating while the light source is on. Measurements are made at pressures below 5 mTorr, and temperatures between room temperature and 470 K are achievable.

As described in Section 1.4, a-Si:H undergoes metastable conductivity changes upon exposure to light. To distinguish between the pre- and post-light soak state, the terms "state A" and "state B" are used, respectively. To return an a-Si:H sample to state A from state B, it is annealed at 470 K for at least two hours. A typical measurement of the photoconductivity in a-Si:H begins with annealed sample in state A at 320 K, the lowest temperature that is easily controllable with just a heater. The dark, state A conductivity σ_A is measured for a few minutes or until it is stable, and then the film is illuminated with white light by a tungsten-halogen (W-Ha) lamp with intensity ~ 100 mW/cm^2 and the photoconductivity σ_{ph} is measured. Although the window filters out most of the IR wavelengths, the temperature increases by a few degrees and stabilizes again to 320 K after a few minutes. When the lamp is turned off, the state B dark conductivity σ_B is measured, typically as a function of temperature as the sample is heated from 320 K to the annealing temperature of 470 K.

– Chapter 3 –

Structural Results of nc-Ge/a-Si:H films

The following chapter will discuss the effects of incorporating germanium nanocrystals into an a-Si:H thin film to create a composite, mixed-phase thin film.

The measurements used to determine the structural properties of the nc-Ge/a-Si:H thin films are now discussed. The methods described herein all involve analysis of the scattering of particles or light from the sample. From these results, we are able to accurately determine the concentration of germanium nanocrystals in each sample.

3.1 – Raman Spectroscopy

This section will describe the technique used to determine the relative fractions of nc-Si, a-Si, nc-Ge, and a-Ge in the nc-Ge/a-Si:H samples, by comparing the Raman signals originating from different phonon modes associated with Si-Si and Ge-Ge bonds.

Typical Raman spectra for a series of samples prepared in a single deposition run are shown in Figure 3.1. These spectra have been normalized to the broad peak at 480 cm^{-1}, which is due to the TO mode of a-Si:H. Across this set of samples, there is a dramatic increase in the size of the sharp peak at 300 cm^{-1}, which is associated with the TO mode in germanium nanocrystals. Unlike in nc-Si, however, the location of the nc-Ge peak is not significantly shifted to lower wavenumber, and in fact is often shifted to higher wavenumbers than in bulk c-Ge, as high as 302 cm^{-1}. This is in agreement with Choi, *et al*., who found the shift to lower wavenumber in nc-Ge to be greatest in nanocrystals with

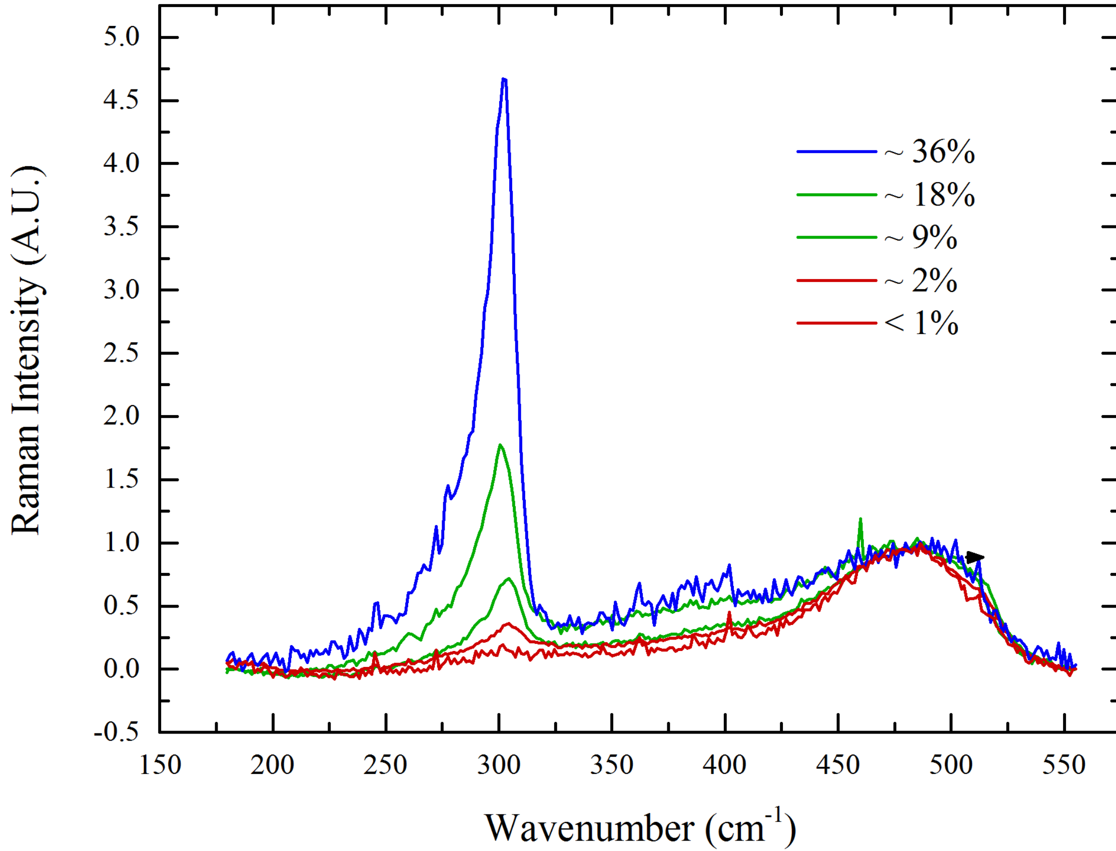

Figure 3.1: Raman spectra for five samples produced in the same deposition run, but different distances from the nanocrystal injection tube. These spectra have been normalized to the a-Si:H TO mode at 480 cm^{-1}.

~6 nm diameters, with a smaller shift as the size decreased, and observed a shift to higher wavenumber for nc-Ge smaller than ~3 nm [50]. In measured spectra of pure germanium nanocrystals, the sharp, asymmetric peak can be fit to four Gaussian peaks at 230, 278, 295 and 300 cm^{-1}. In most cases, the peak at 230 cm^{-1} is the shortest and widest of the four peaks, and the one at 300 cm^{-1} is the tallest and narrowest (see Figure 3.2). This same fitting technique is applied to the nc-Ge signal in the mixed-phase samples presented in this paper, and the sum of the four areas is used for the total signal originating from the nc-Ge phase.

Another feature visible in the spectra shown in Figure 3.1 is a broad peak centered around 390 cm^{-1}. In amorphous Si-Ge alloys, a similar peak is observed, and is attributed to Si-Ge bonds [57,58]. In these nc-Ge/a-Si:H samples, the peak at 390 cm^{-1} is likely due to asymmetric Si-Ge bonds on the surfaces of the Ge nanocrystals and not Si-Ge alloying within the a-Si:H matrix, reflected in the roughly linear relationship between the sizes of the Si-Ge peak at 390 cm^{-1} and the nc-Ge peak at 300 cm^{-1} in Figure 3.1. If there were any significant alloying of Si and Ge in the amorphous phase, its magnitude would be independent of the germanium crystal fraction. This was verified by growing a set of films with identical parameters to a nc-Ge/a-Si:H run, except that the nanocrystal plasma was turned off. The resulting Raman spectrum from this hydrogenated amorphous Si-Ge alloy displayed broad peaks at 278 and 480 cm^{-1} corresponding to the TO modes in a-Ge:H and a-Si:H, respectively, and a broad peak centered at 390 cm^{-1}. The relative magnitudes of each of these peaks were independent of the location of the substrate in the deposition chamber. The variation in the height of the peak at 390 cm^{-1} in the nc-Ge/a-Si:H samples is therefore not due to alloying that is sensitive to the substrate location, but is rather associated with the Si-Ge bonds surrounding the nanocrystals themselves (whose concentration is sensitive to the distance from the nanocrystal injection tube). At present, the process of fitting the Raman peaks is uncertain enough that any studies of the expected sub-linear saturation of the relative size of the 390 cm^{-1} peak due to Ge-Ge bonds at the nanocrystal surfaces at very high X_{Ge} are not possible.

In pure a-Si:H films, the Raman spectrum between 250 cm^{-1} and 500 cm^{-1} consists of the LA, LO and TO Si-Si modes at 320, 410 and 480 cm^{-1}, respectively. Samples far from the nanocrystal inlet, with undetectably small germanium concentrations such as the

sample with $X_{Ge} < 1\%$ in Figure 3.1, can be accurately fit using Gaussian functions centered at these three wavenumbers, as described in Section 2.1.1. When the germanium concentration increases, however, the broad Si-Ge mode at 390 cm^{-1} sufficiently overlaps with the 320 and 410 cm^{-1} peaks to make any attempt to fit all peaks simultaneously prohibitively difficult. In order to limit the number of variables, it is necessary to first subtract the pure a-Si:H signal from the total spectrum, where the pure a-Si:H signal is assumed to be unchanged in each spectrum from a given deposition run. The resulting spectrum, shown in Figure 3.2 for the sample with $X_{Ge} \sim 36\%$ from Figure 3.1, then contains the asymmetric nc-Ge peak at 300 cm^{-1}, the broad Si-Ge mode around 390 cm^{-1}, and in many samples, a small μc-Si peak around 510 cm^{-1}. The mc-Si peak is likely the result of Ar bombardment of the growing a-Si:H, crystallizing a portion of the amorphous film and creating hydrogenated microcrystalline silicon [59]. The resulting crystalline silicon fraction is usually smaller than 1% and does not contribute significantly to the electronic properties of the composite film.

The final, quantitative determination of the germanium crystal fraction is then determined by comparing the relative integrated areas of the nc-Ge and a-Si:H TO modes,

$$X_{Ge} = A_{Ge} / (A_{Ge} + \gamma \mathrm{A}_{Si}) \tag{3.1}$$

where γ is the ratio of the relative Raman scattering cross-sections, σ_{Ge}/σ_{Si}. This parameter was determined experimentally by comparing with results from Rutherford Back Scattering of the same samples, which will be discussed below.

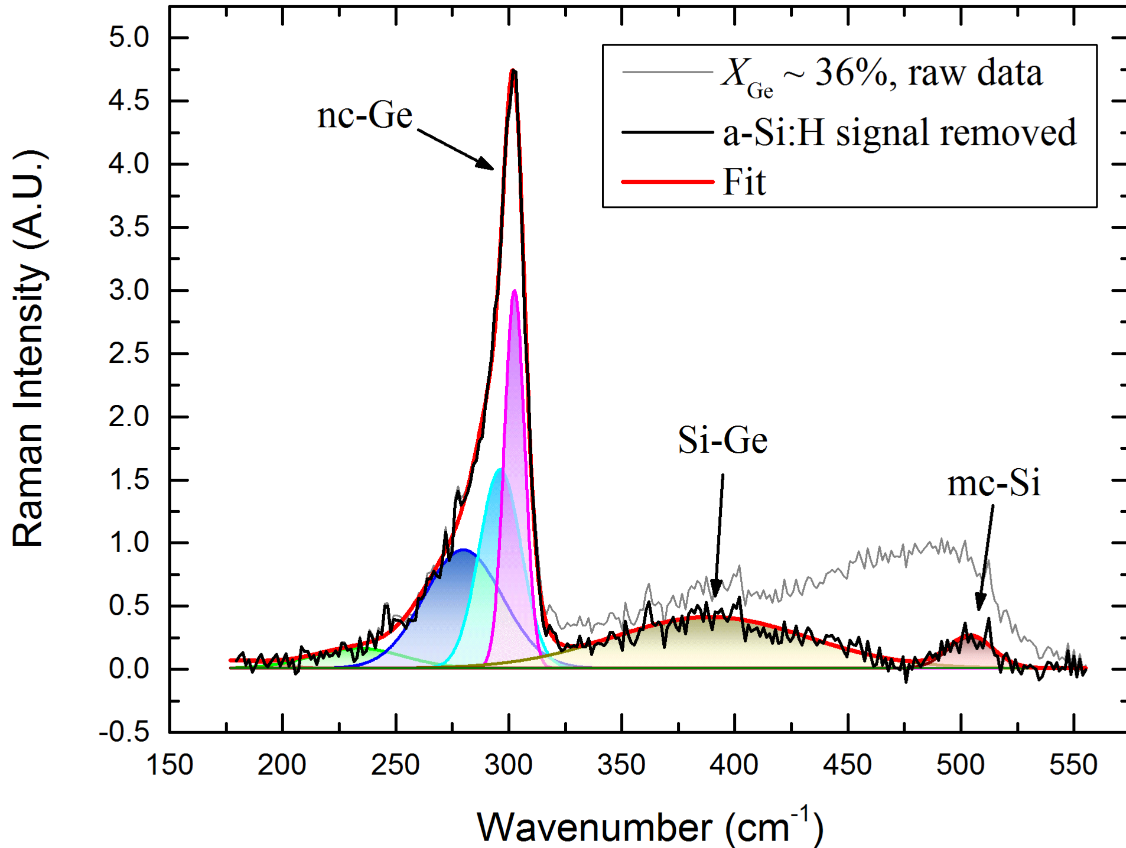

Figure 3.2: Raman spectrum of a nc-Ge/a-Si:H sample with X_{Ge} ~ 36% from Figure 3.1 illustrating the process used to fit the nc-Ge component and determine X_{Ge}. The full Raman spectrum (gray) contains broad Gaussian peaks associated with the a-Si:H component which overlap significantly with the Si-Ge peak. The a-Si:H component is first subtracted from the full signal, and the black curve is obtained, which can be fit (red) to 6 Gaussian peaks which overlap only slightly.

3.2 – X-Ray Diffraction

The sizes of the germanium nanocrystals were determined via X-ray diffraction. Measurements were made on a Bruker D8 Discover microdiffractometer on the nc-Ge/a-Si:H samples and on accumulations of nc-Ge dust from deposition runs in which the film plasma was turned off and no SiH_4 was present in the system. There are no substantial variations between the germanium nanocrystals in the nc-Ge/a-Si:H thin films and

freestanding nc-Ge. Diffraction spectra for a few nc-Ge/a-Si:H samples are shown in Figure 3.3. Two main diffraction peaks are present in these spectra, correlating to the (111) and (220) crystal planes for germanium. The small size of the nanocrystals leads to broadening of these peaks, as described in Section 2.1.4. Calculating the width of the peaks, it is possible to determine the size of the nanocrystals, parallel to the relevant crystal plane. We find spherical nanocrystals with diameters ranging from 3.5 to 4.5 nm in films with X_{Ge} between 2% and 35%. Across a single deposition run, nanocrystal sizes are fairly

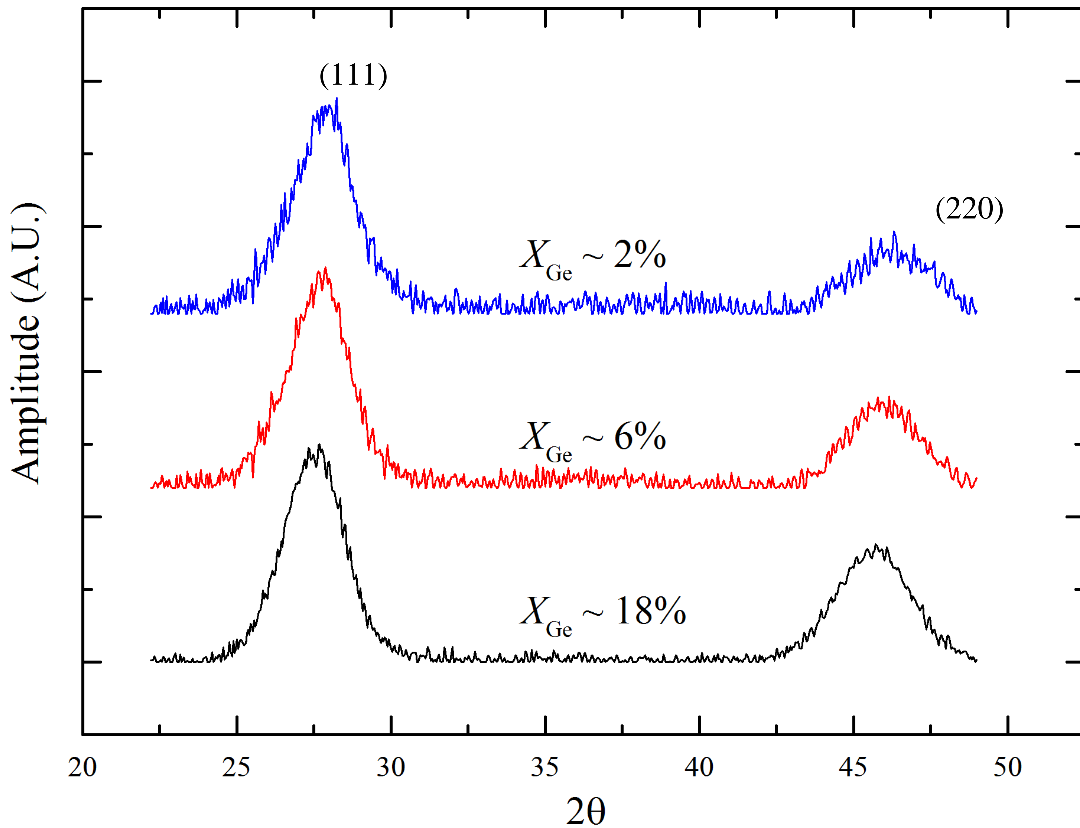

Figure 3.3: X-ray diffraction measurements on three nc-Ge/a-Si:H samples showing peaks due to diffraction in the (111) and (220) planes, where the germanium crystal fraction labeled for each sample was determined by Raman spectroscopy. These samples were synthesized in the same deposition run and display diffraction peak widths that correspond to nanocrystal diameters of 3.5-4.5 nm.

consistent, with variations in diameter of less than 1 nm, suggesting that the nanocrystal plasma produces relatively homogenously sized nanocrystals. In the event of a wide size distribution, one would expect that samples with lower X_{Ge} would have smaller nanocrystals than those with large X_{Ge}, because they were farther from than nanocrystal inlet during deposition.

3.3 – Rutherford Backscattering (RBS)

RBS measurements allow the determination of the number fraction of each element in the sample. This was used to find γ in Equation (3.1), which provides a path to use the Raman spectra to determine X_{Ge} for each film. Eight samples were measured from two deposition runs, with X_{Ge} found to be between 1 and 60%. Correlating these values with the Raman spectra of the same samples, γ was found to be 2.63.

RBS spectra were measured using an incident beam of He^{++} ions at 3.8 MeV, focused onto a 2 mm diameter spot. Figure 3.4 shows a typical RBS spectrum with a matching model that reveals that about 29% of the atoms in the sample are Ge and the rest are Si with about 10% oxygen as well. The spectrum features "plateaus" that each correspond to different elements in the sample. The width of the plateau is determined by the density and thickness of the layer, and the maximum energy of the plateau is determined by the mass and charge of the backscattering atom. For this sample with two layers, the thin film and the glass substrate, some ions pass through the top layer and backscatter off the substrate. The measured energies of those ions that are backscattered in the substrate are shifted to lower energies than if they had scattered off an identical atom in the film, as they passed through the thickness of the film and felt its entire stopping power. This makes

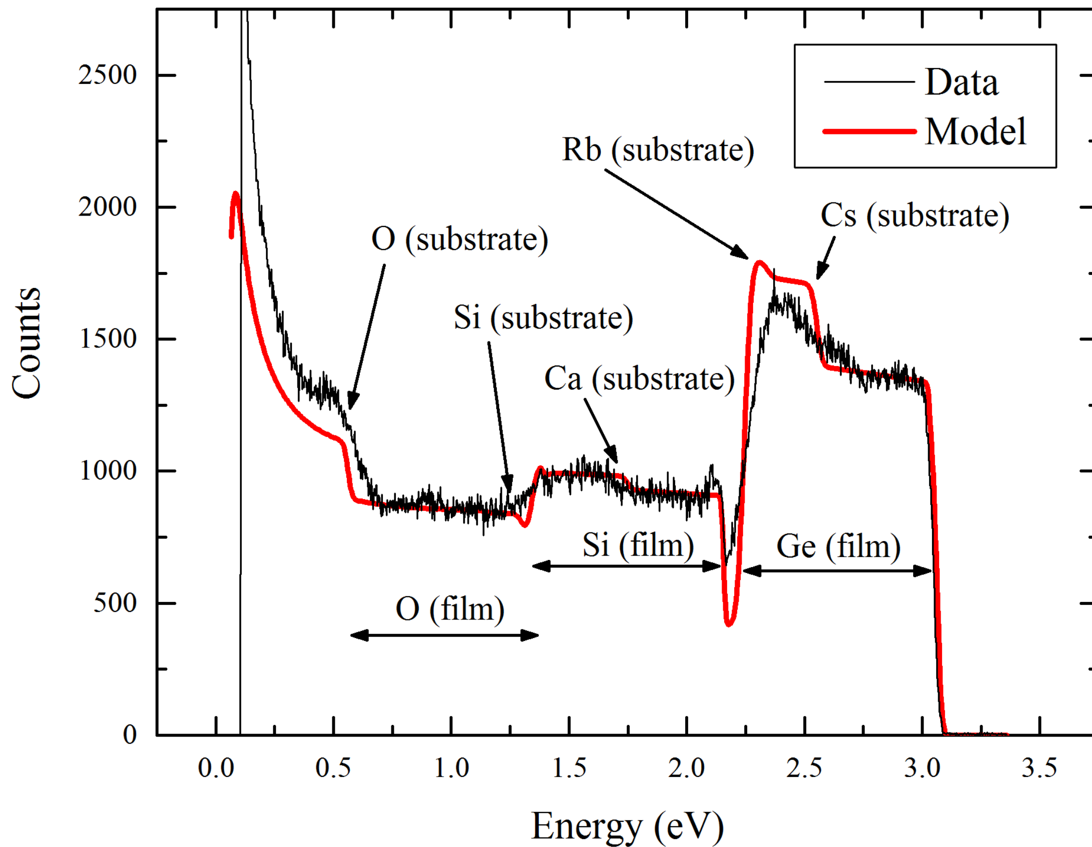

Figure 3.4: Rutherford backscattering measurement (black) and matching model (red) for a nc-Ge/a-Si:H sample with X_{Ge} ~ 32%.

it difficult to directly identify the substrate signal, since each of its plateaus are shifted to lower energies than would be expected, by an amount which is dependent on the exact composition of the film. For an accurate model of the combined film and substrate system, it is therefore necessary to know the exact atomic makeup of the substrate, which is straightforward to calculate from an RBS measurement of a bare substrate. The results of this measurement on the glass used for the substrate of the nc-Ge/a-Si:H samples is shown in Figure 2.3, revealing significant impurities of high-Z atoms including Cs and Rb.

Surprisingly, the RBS measurements on these nc-Ge/a-Si:H samples indicates that their density is very low, at least for samples with high X_{Ge}. For instance, the sample shown in Figure 3.4 with X_{Ge} ~ 32%, would be expected to have a density of 3.53 g/cm^{-3}. The RBS model uses the known thickness of the film, as measured via profilometry, and finds a density of only 1.5 g/cm^{-3}. This means that over half of the macroscopic bulk of this sample consists of voids. It is unclear exactly how the microscopic structure looks, but one can imagine extensive shadowing by nanocrystals which are piling up on top of each other faster than the a-Si:H film can fill in the gaps. The void fraction increases more or less linearly with X_{Ge}, and is approximately zero for X_{Ge} ~ 0%.

Given the large void fraction, it is not surprising that there is a significant amount of oxygen present in these films. For the sample in Figure 3.4, oxygen accounts for approximately 10% of all the atoms in the film, and the amount of oxygen also scales roughly linearly with X_{Ge}, presumably residing on the surfaces of the voids. Note that two oxygen signals are present in Figure 3.4, one arising from oxygen in the sample and the other, at a lower energy, from oxygen in the substrate. As seen in Figure 3.4, the film oxygen signal is very weak compared to that of Si and Ge, so there is a large uncertainty in the amount of oxygen in each film from this measurement. The a-Si:H phase of these samples is also significantly composed of H atoms, which are not included in the simulation. Because H atoms are less massive than the He^{++} nuclei which are incident on the sample, there can be no backscattering from any H atoms in the sample. Similar to RBS, Forward Recoil Elastic Spectrometry (FRES) measures the non-backscattered signal, and would be an effective avenue to determine the amount of hydrogen in these films.

3.4 – Fourier Transform Infrared Spectroscopy

Infrared spectra were recorded on nc-Ge/a-Si:H to probe the bonding between Si & Ge and hydrogen. Measured FTIR spectra for three samples from the same deposition run are shown in Figure 3.5. While these spectra are measured between 375 and 4000 cm^{-1}, the data in Figure 3.5 is restricted to the region between 1800 and 2400 cm^{-1} where the Si-H and Ge-H stretching modes are found. In Figure 3.5a, which displays a sample with X_{Ge} ~ 0%, the signal is dominated by two peaks at 2000 cm^{-1} and 2090 cm^{-1}, as in pure a-Si:H (Figure 2.2). In Figure 3.5b (X_{Ge} ~ 2.5%) and Figure 3.5c (X_{Ge} ~ 21%), as X_{Ge} increases, a mode at 2250 cm^{-1} is found to increase correspondingly. An infrared-active mode at 2250 cm^{-1} has previously been reported in samples of porous, oxidized silicon, and is attributed to Si-H bonds when the Si atom is back-bonded to three oxygen atoms [60,61]. This is a plausible source of the mode at 2250 cm^{-1} in the samples presented here, because RBS measurements indicate that the material becomes very porous as X_{Ge} increases and the film becomes significantly oxidized.

A second feature that can be seen across these figures is the relative sizes of the 2000 and 2090 cm^{-1} peaks. As X_{Ge} increases, the size of the 2090 cm^{-1} peak increases relative to the size of the 2000 cm^{-1} peak. In pure a-Si:H samples, a large peak at 2090 cm^{-1} is associated with SiH_2 stretching modes, found to be correlated with large defect densities and poor electronic quality. It seems reasonable that, as nc-Ge are embedded into the a-Si:H, the surrounding film is structurally perturbed and becomes more disordered. The parameter R can be calculated using Equation (2.1), and is found to be

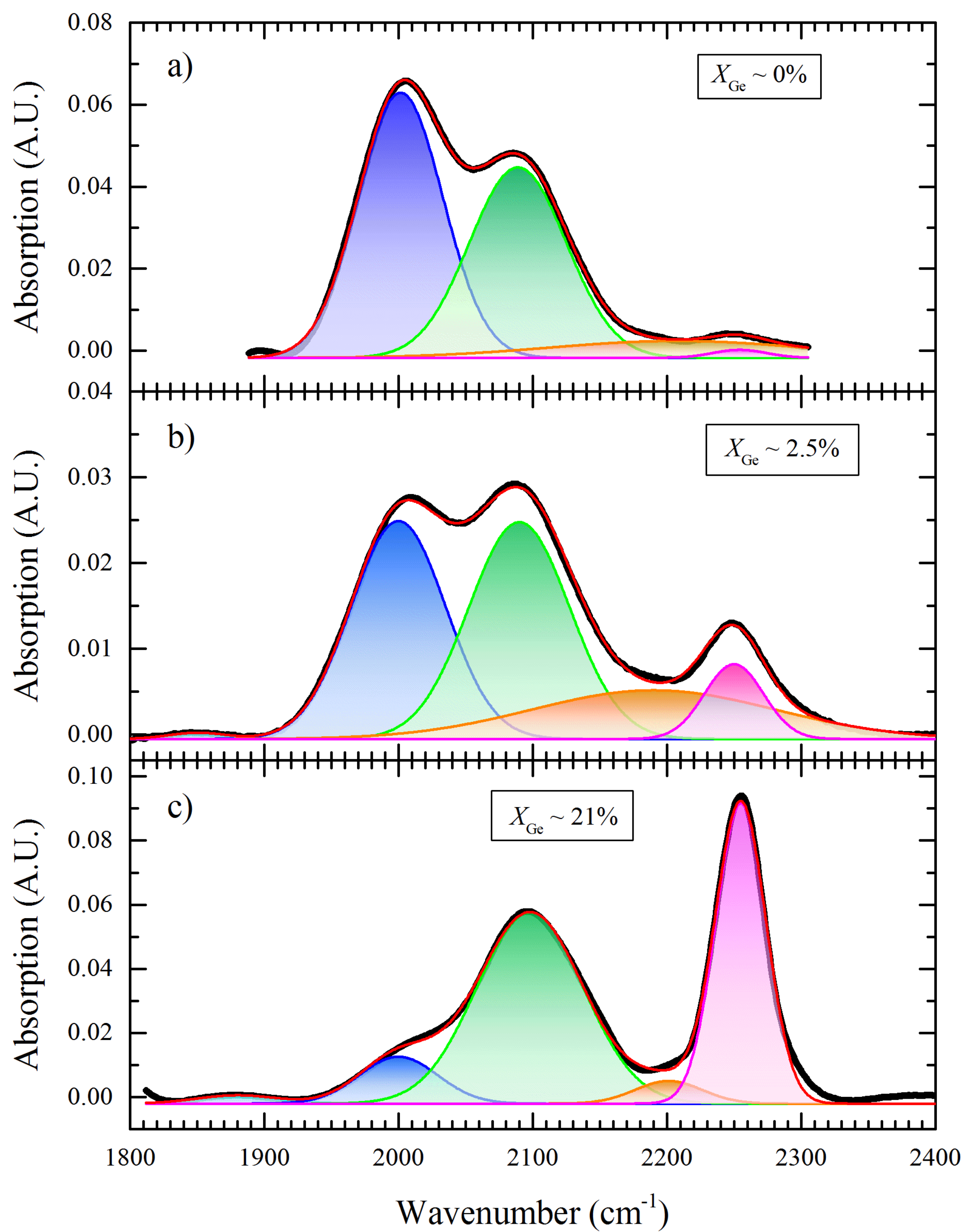

Figure 3.5: Plots of measured FTIR spectra and fits to those spectra for samples from a single deposition run with (a) X_{Ge} ~ 0%, (b) X_{Ge} ~ 2.5%, and (c) X_{Ge} ~ 21%. The thick black line is the measured data and the red line is the sum of the Gaussian peaks in blue, green, orange and magenta.

0.45 in Figure 3.5a (X_{Ge} ~ 0%), 0.51 in Figure 3.5b (X_{Ge} ~ 2.5%), and 0.93 in Figure 3.5c (X_{Ge} ~ 21%).

The fits in Figure 3.5 also include a Gaussian peak at 2190 cm^{-1}. The origin of this peak is difficult to determine with certainty, and while it may correspond to an infrared-active mode, for example, a Si-H stretching mode when the Si atom is back-bonded to 1 or 2 oxygen atoms, it may also simply be an artifact of the background subtraction involved in producing these spectra. These nc-Ge/a-Si:H samples are relatively thick, > 1 μm, and the absorption fringes due to reflections off the front and back surfaces of the film are around 1000 cm^{-1} apart. The fringes are very large compared to the peaks described here, so they must be subtracted from the spectrum before fitting can be performed. This process is difficult when multiple broad peaks overlap as in these spectra, especially when the peaks of interest lie in an area where the fringes have significant curvature.

There is little clear evidence of Ge-H bonds in these FTIR spectra. In a-Ge:H, the Ge-H stretching mode is found at 1870 cm^{-1}, and the Ge-H_2 stretching mode is found at 1980 cm^{-1}. These modes are analogous to the 2000 and 2090 cm^{-1} Si-H stretching modes in a-Si:H, and because we believe there is no significant Si-Ge alloying in the amorphous phase, it is understandable that the 1870 and 1980 cm^{-1} modes would be absent. In FTIR measurements on silicon nanocrystals, however, the dominant mode is found at 2090 cm^{-1}, and is generally attributed to Si-H bonds on the surfaces of the nanocrystals. We might expect to see an analogous peak in these nc-Ge/a-Si:H samples at 1980 cm^{-1}, but it is impossible to distinguish this peak from the Si-H mode at 2000 cm^{-1}. It is unclear to what extent the peak near 2000 cm^{-1} in Figure 3.5 originates from the Si-H bonds in a-Si:H or the Ge-H bonds in nc-Ge or both.

In the samples presented here, *R* is found to increase with germanium content, as shown in Figure 3.6. This is likely due to the presence of voids introduced at the interfaces with the germanium nanocrystals. In pure a-Si:H films, the surfaces of voids are believed to be hydrogen-terminated, and contribute to infrared absorption near 2090 cm^{-1} [55]. As shown in Section 3.3, the addition of nc-Ge introduces voids in the composite nc-Ge/a-Si:H film, resulting in enhanced absorption at 2090 cm^{-1}.

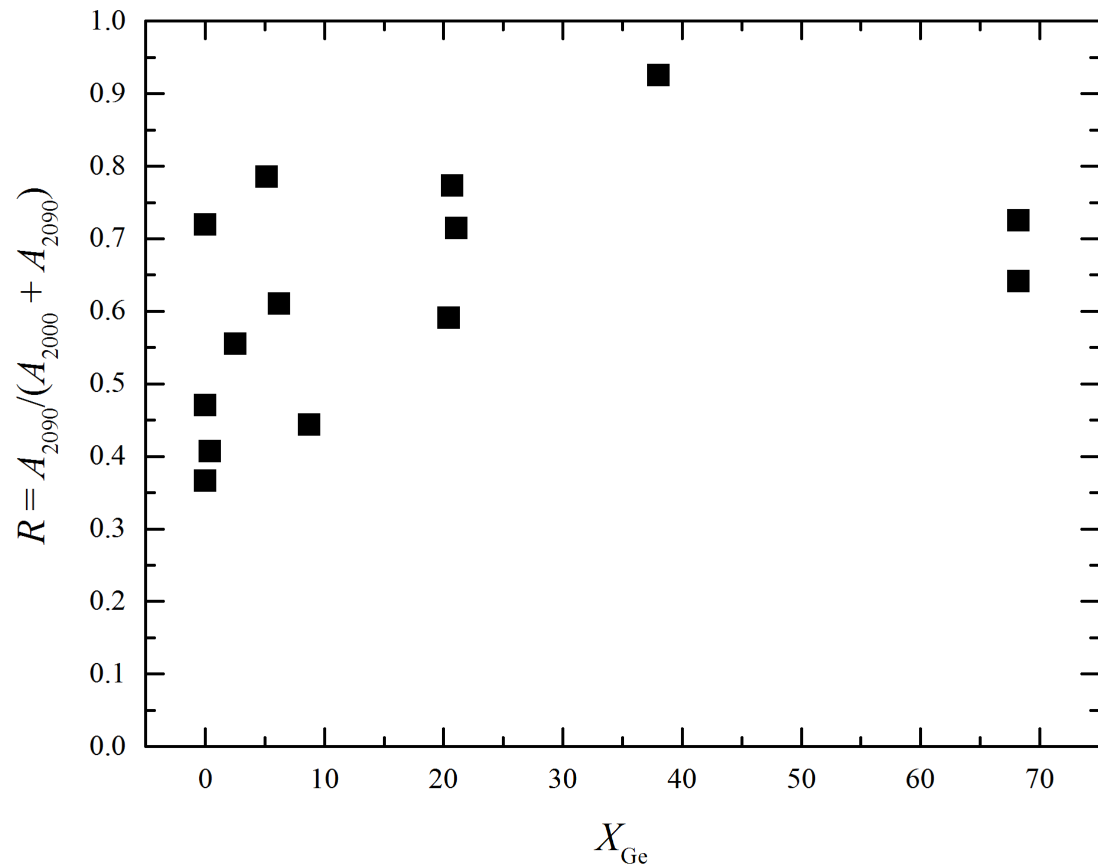

Figure 3.6: Plot of the *R* factor, a measure of the relative FTIR absorption at 2090 cm^{-1} to that at 2000 cm^{-1} and 2090 cm^{-1}, against the germanium crystal fraction X_{Ge} for a number of nc-Ge/a-Si:H samples with X_{Ge} between 0 and 70%.

– Chapter 4 –

Transport Properties of nc-Ge/a-Si:H films

4.1 – Conductivity

Measurements of the temperature dependence of the dark conductivity were performed in a closed-cycle cryostat as discussed in Section 2.2.1, for samples with X_{Ge} ranging from 0 to 75%. Figure 4.1 shows Arrhenius plots of the conductivity σ vs $1000/T$ for just three samples, which were chosen to illustrate the three distinct regimes that were found as X_{Ge} is varied. For low ($X_{Ge} < 10\%$, red circles) and high ($X_{Ge} > 25\%$, blue squares) germanium crystal fractions, these data are well described by Equation (1.2), $\sigma = \sigma_0 exp[-E_\sigma / k_B T]$, where σ_o is the pre-exponential factor and E_σ is the conductivity activation energy. For $X_{Ge} < 10\%$, $E_\sigma \sim 0.75$ eV, similar to previous measurements of pure, undoped a-Si:H films [62] and for $X_{Ge} > 25\%$, $E_\sigma \sim 0.4$ eV, consistent with other measurements of germanium nanocrystal films [63].

Samples with intermediate crystal fractions show significant curvature on an Arrhenius plot, however. In order to more accurately determine the conductivity temperature dependence, the "reduced activation energy" is calculated using a procedure developed by Zabrodskii and Shlimak [64]. The logarithmic derivative of the conductivity $w(T) = \mathrm{d}ln\sigma/\mathrm{d}ln\mathrm{T}$ is computed, and plotted against temperature on a log-log plot, shown in the inset to Figure 4.1. Thermally activated conduction would yield a slope of -1, with different activation energies represented as parallel lines. The calculations of the reduced activation energies of the curves in Figure 4.1 indicate that conduction is thermally

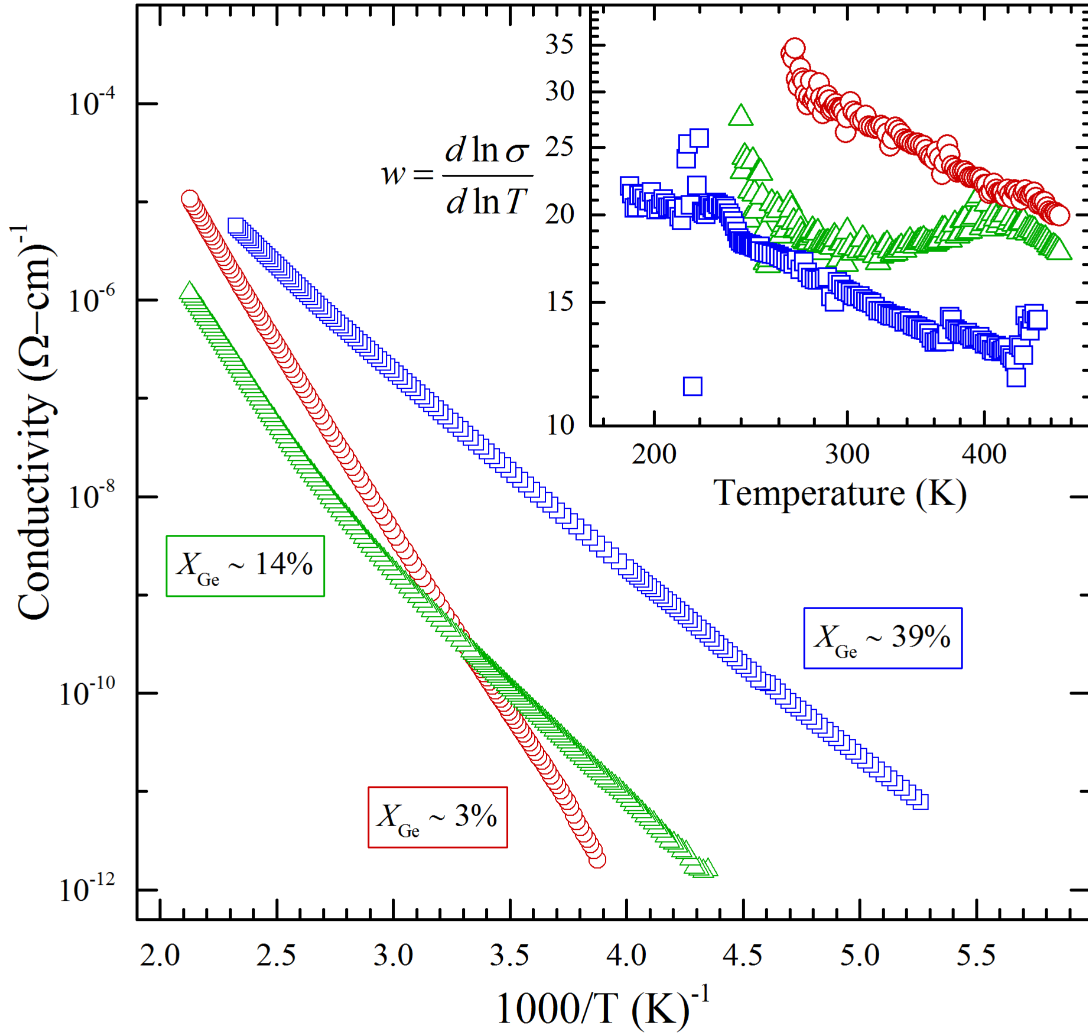

Figure 4.1: Arrhenius plots of the conductivity for three nc-Ge/a-Si:H films with X_{Ge} of 3% (red circles), 14% (green triangles) and 39% (blue squares). The inset shows calculations of the reduced activation energy vs. temperature on a log-log plot for each curve in the main figure.

activated [65] with single activation energies for both the n- and p-type samples, while the transition samples display conduction similar to that seen in the p-type films at low temperature and conduction similar to that seen in the n-type samples at high temperature. [We note that there is in fact a small but significant deviation from purely Arrhenius behavior observed these films, which will be discussed in detail in Chapter 6. For the time

being we will consider the conductivity in these films to be adequately described by a thermally activated expression, Equation (1.2).] The measured conductivity of the X_{Ge} ~ 14% film fits very closely to the sum of two activated conduction paths

$$\sigma = \sigma_1 exp\left[-\frac{E_1}{k_B T}\right] + \sigma_2 exp\left[-\frac{E_2}{k_B T}\right] \tag{4.1}$$

with activation energies E_1 = 0.77 eV and E_2 = 0.43 eV, corresponding to a-Si:H and nc-Ge conduction, respectively. Figure 4.2 plots the measured conductivity for this film along with the calculated fit and the exponential curves that comprise the fit curve. The inset to Figure 4.2 shows the reduced activation energy calculation performed on each of these curves and serves as further evidence of the quality of the fit. It is worth noting here that it was possible to achieve a satisfactory fit of the conductivity using significantly different values for the parameters $\sigma_{1,2}$ and $\varepsilon_{1,2}$, or even using a completely different functional form, such as $\sigma(T) = \sigma_1 \exp[-(T_0/T)^{\kappa}]$, as in Mott and Efros-Shklovskii variable-range hopping [28,29]. However, because the reduced activation energy calculation is sensitive to variations in the data, none of these other potential fits matched the reduced activation energy of the measured data, as in the inset to Figure 4.2. Unlike n-type doped a-Si:H containing silicon nanocrystal inclusions, there is no evidence of multi-phonon hopping in the transition regime [31].

Figure 4.3 plots the activation energy against germanium crystal fraction for a series of composite films. The thermally activated conductivity is always well described by a single activation energy of ~ 0.75 – 0.8 eV for $X_{Ge} < 10\%$ and ~ 0.4 eV for $X_{Ge} > 25\%$. For

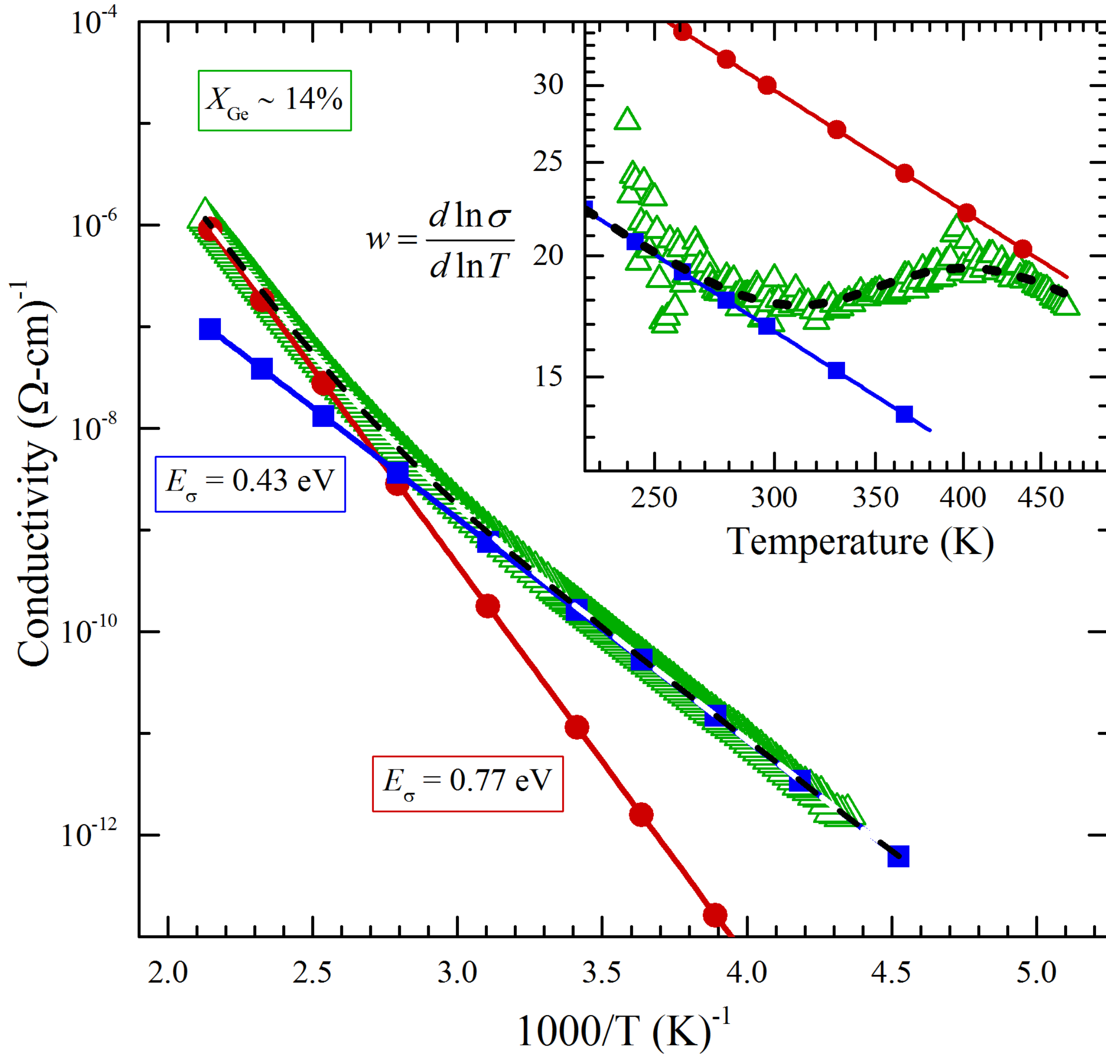

Figure 4.2: Arrhenius plot of the conductivity of the transition film with X_{Ge} = 14% from Figure 4.1 (green triangles). The red (circles) and blue (squares) lines represent thermally activated conductivities with activation energies of 0.77 eV and 0.43 eV, respectively. The dashed line indicates the result of adding the two thermally activated expressions. The inset shows calculations of the reduced activation energy vs. temperature on a log-log plot for the same set of curves.

the films with intermediate germanium content, the activation energies shown in Figure 4.3 are those which yield good fits across the entire measured temperature range, as in Figure 4.2.

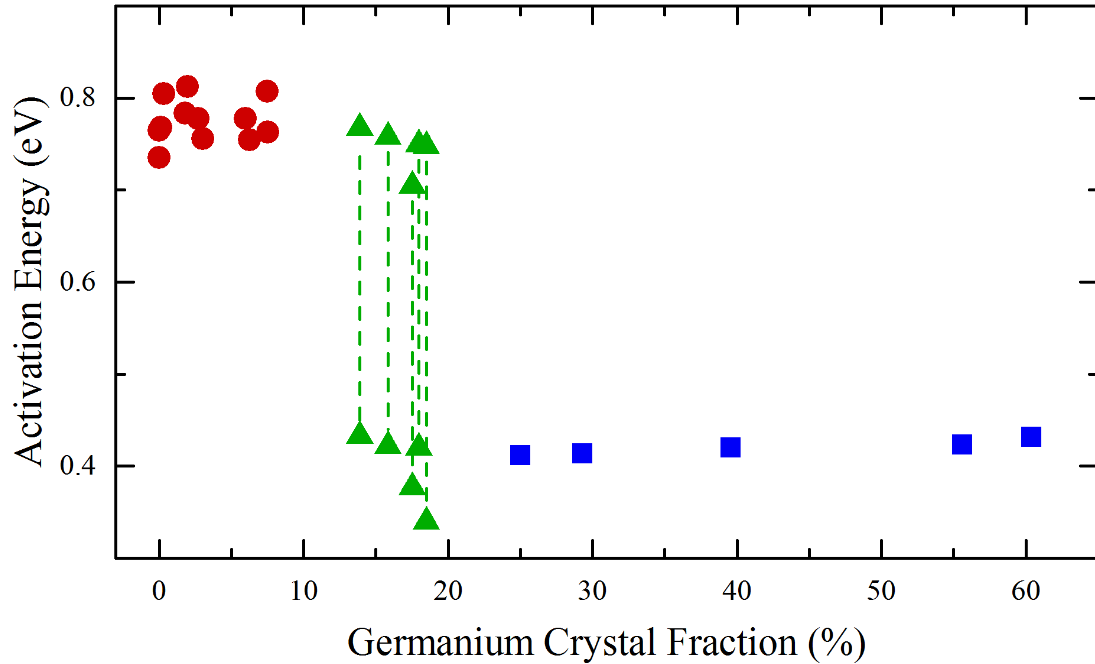

Figure 4.3**:** Plot of the activation energy obtained from Arrhenius plots of the dark conductivity against germanium crystal fraction for a series of nc-Ge/a-Si:H films. For films in the transition region (as in Figure 4.2), which are best described by two activation energies, both values from high and low temperature fits are plotted.

4.2 – Thermopower

The thermopower of composite nc-Ge/a-Si:H films was found using the measurement system and technique described in Section 2.2.2. Figure 4.4a shows the raw thermopower data for a single sample with a germanium concentration of about 0.1%. Each group of connected data points represents a different T_{avg} from 350 to 450 K, and each data point within a group is a different ΔT. All curves clearly display a negative slope over the entire temperature range examined, indicating n-type conduction. Similarly, a film with X_{Ge} = 54%, shown in Figure 4.4c, displays an induced voltage against temperature with a

positive slope, indicating p-type conduction. In contrast, a film with an intermediate germanium concentration of $X_{Ge} = 18\%$, shown in Figure 4.4b, displays a positive slope near room temperature, and above ~ 370 K the slope of the plot of ΔV against ΔT has rotated to a negative value. This measurement procedure was repeated for all of the films synthesized, with $0\% < X_{Ge} < 75\%$.

Figure 4.5 shows plots of the Seebeck coefficient against $1000/T_{avg}$ of the nc-Ge/a-Si:H films with germanium crystal fractions ranging from 0% (pure a- Si:H) up to $X_{Ge} = 75\%$. For all of the films for which $X_{Ge} < 10\%$, a negative thermopower is observed; fits of these data to $S = (k_B / e)[E_S / k_B T + A]$ find a negative activation energy E_S ~ - 0.3 to - 0.5 eV, consistent with previous measurements of undoped a-Si:H [33]. For germanium crystal fractions between approximately $10 < X_{Ge} < 25\%$, the thermopower exhibits a temperature dependent transition to positive values at lower temperatures. For $X_{Ge} > 25\%$, the thermopower is positive for all temperatures examined, with a smaller, positive slope of $E_S \sim +0.2$ eV.

These results are consistent with a transition from conduction through the a-Si:H at low X_{Ge} to through the nc-Ge at high X_{Ge}. P-type conduction has been observed in bulk single crystal germanium [66], polycrystalline germanium [67], single-crystal germanium nanowires [68,69], Ge/Si core-shell nanowires [70–72] and Ge nanocrystals embedded within a SiO_2 matrix prepared by co-sputtering [63]. In nanoscale materials, p-type transport has been attributed to a hole accumulation layer in the germanium nanocrystals due to acceptor-like surface states [69,71]. This is in contrast with hydrogenated microcrystalline germanium, which has been found to have an n-type thermopower with

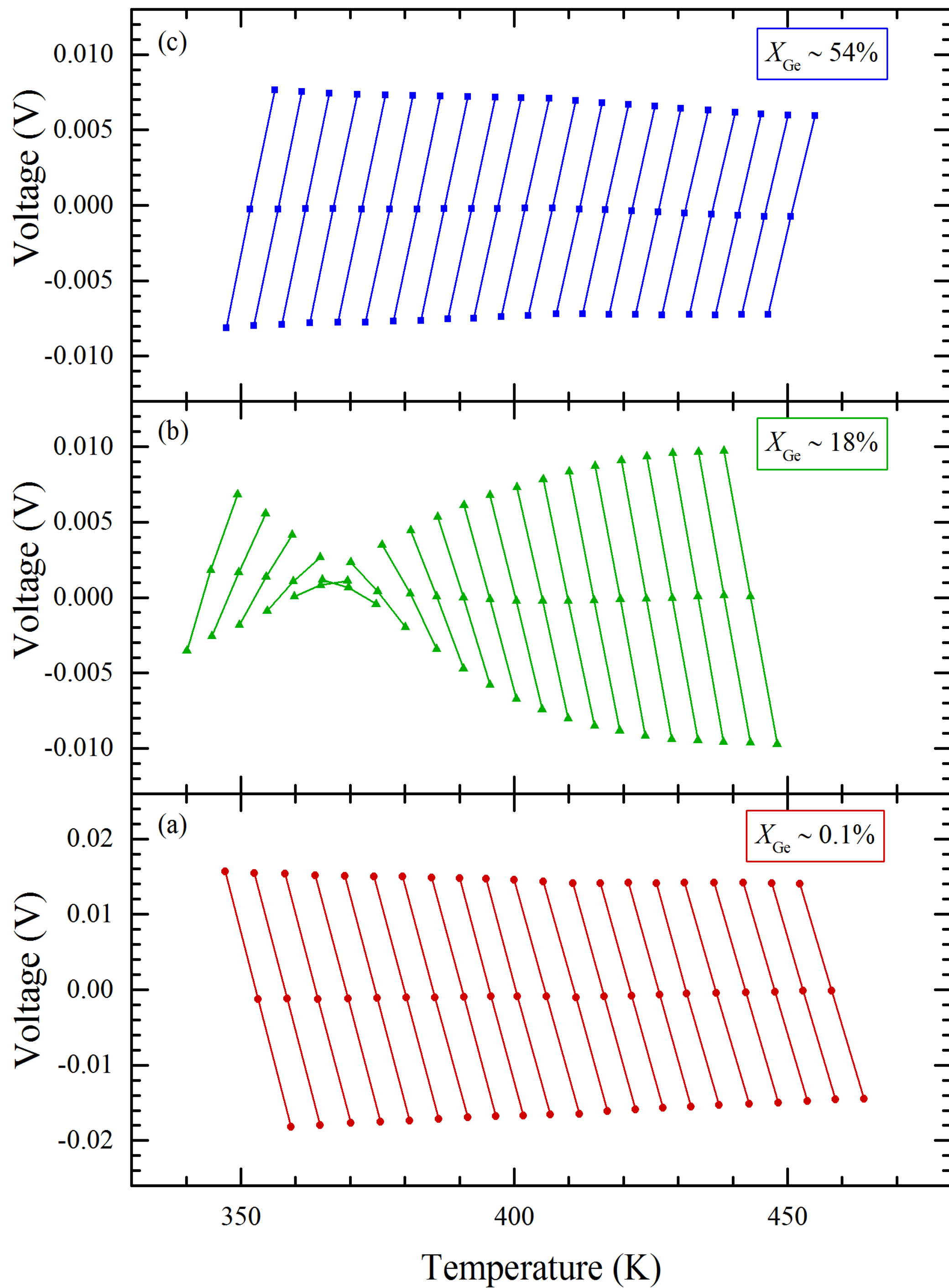

Figure 4.4**:** Plots of measured voltage vs. temperature for three samples with (a) X_{Ge} ~ 0%, (b) X_{Ge} ~ 18%, and (c) X_{Ge} ~ 54%. Each curve on the plots represents the voltage measurements at temperatures $T = T_{avg} \pm \Delta T/2$ and $T = T_{avg}$. Note change of scale for Figure 4.4a. A negative slope indicates n-type conduction, while a positive slope indicates p-type conduction.

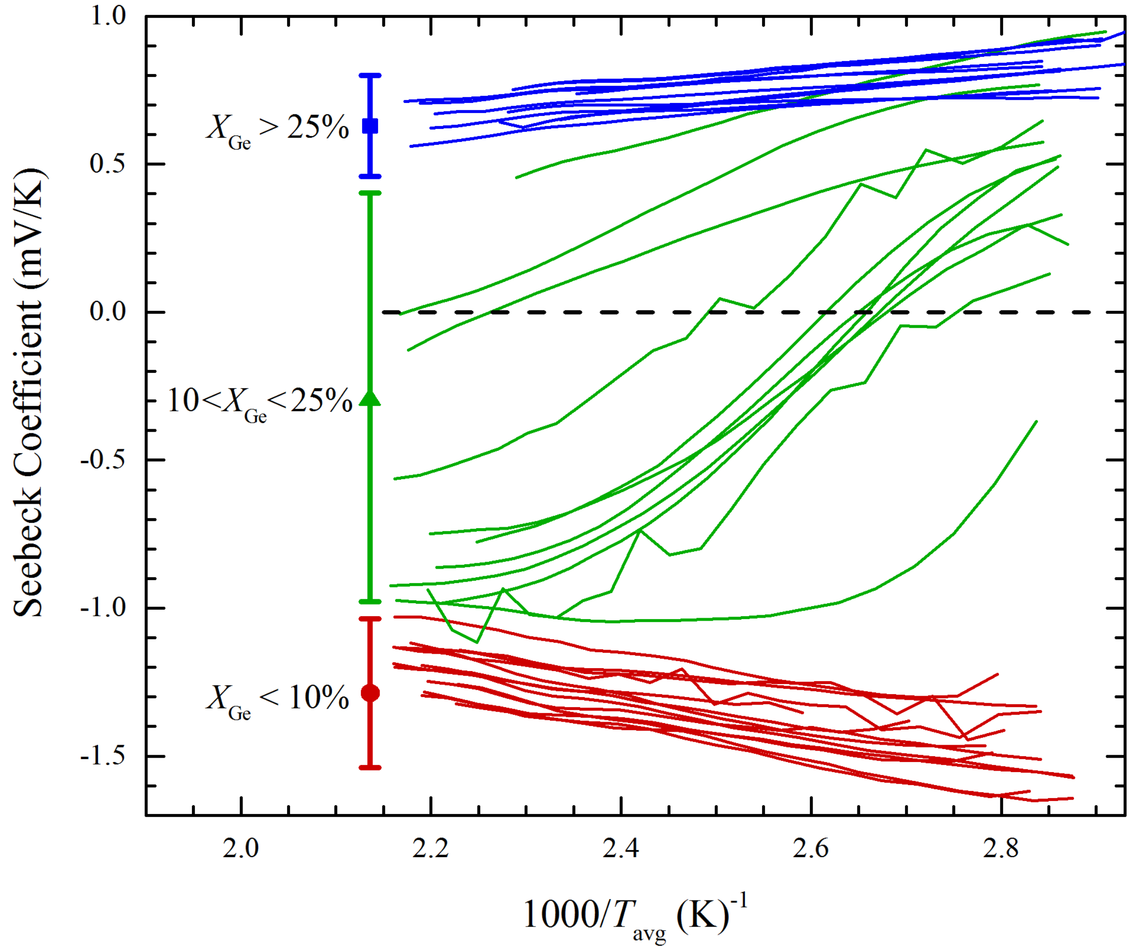

Figure 4.5: Measured Seebeck coefficients plotted against 1000/T_{avg} for nc-Ge/a-Si:H thin films with X_{Ge} = 0 (pure a-Si:H) to X_{Ge} = 75%.

grain diameters as small as 5 nm [73]. It is possible that a hole accumulation layer arises due to interfacial effects between the germanium nanocrystal and surrounding silicon atoms or polymers, which are not found in microcrystalline germanium.

Figure 4.1 and Figure 4.5 find that the dark conductivity activation energy ε_σ is larger than the thermopower activation energy E_S in both the low and high X_{Ge} regimes. The difference in activation energies in a-Si:H is well-known, and is typically ascribed to the influence of long-ranged disorder, such as potential fluctuations or composition

modulations, on electronic transport [21,62]. However, a difference in activation energies is not expected in crystalline materials, and the difference found here for the $X_{Ge} > 25\%$ films may be due to energy barriers associated with the grain boundary region surrounding the nanocrystals.

Note also that if the transition from n-type to p-type transport were due to the addition of holes in the a-Si:H matrix, donated from the nc-Ge, then one would expect the activation energy of the a-Si:H to initially increase with increasing X_{Ge} when the Fermi energy is pulled towards midgap, and then decrease with increasing germanium concentration as the Fermi energy moves towards the valence band edge. That this is not observed in Figure 4.3 supports the model of two distinct conduction channels, through the a-Si:H and through interconnected nc-Ge chains.

4.3 – Discussion

The nc-Ge/a-Si:H thin films display a transition from n-type to p-type conduction as X_{Ge} is increased, and for samples with $10 < X_{Ge} < 25\%$, a transition from n- to p-type is observed as the temperature is increased. For samples with an n-type thermopower, the conductivity is well-described by an Arrhenius expression with activation energy $E_{\sigma} \sim 0.8$ eV. For samples with a p-type thermopower, the activation energy is ~ 0.4 eV, and transition samples see a transition between the two activation energies, corresponding very well to the transition in the sign of the thermopower. The simplest explanation for this behavior is that the n-type samples show conduction through the a-Si:H, the p-type samples show conduction through the nc-Ge, and in the transition samples, current flows through both phases, weighted by the germanium crystal fraction. This is a dual-channel picture,

which has been studied in other systems and can be imagined as two parallel resistors, one composed of a-Si:H and the other of nc-Ge, as in Figure 4.6. The a-Si:H resistor is intrinsically n-type with an activation energy of ~ 0.8 eV and the nc-Ge resistor is intrinsically p-type with an activation energy of ~ 0.4 eV. For samples with small crystal fractions, we can imagine the a-Si:H resistor has a large cross-section while the nc-Ge resistor has a very narrow cross-section. The resistance of the nc-Ge resistor is then much larger than the resistance of the a-Si:H resistor, and much more current flows through the a-Si:H, so the sample is n-type with an activation energy of ~ 0.8 eV. For samples with large X_{Ge}, the opposite holds and the sample is p-type with an activation energy of ~ 0.4 eV. For samples with intermediate X_{Ge}, the resistances of each resistor are relatively similar, so current flows through both. The difference in activation energy between the two phases means that as the temperature is increased, the resistance of the a-Si:H phase decreases faster than the resistance of the nc-Ge phase, and a larger percentage of the total current passes through the a-Si:H.

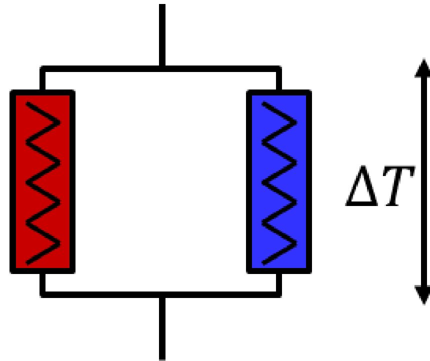

Figure 4.6: Cartoon representation of the dual-channel model describing conduction through these nc-Ge/a-Si:H samples. One imagines consolidating all the germanium nanocrystals into a single sample, and the remaining a-Si:H film in a separate sample, then measuring across the parallel combination of the two samples.

The dual-channel model has been studied extensively in the context of metal alloys and composites [74], and these results can be applied here. The conductivity $\sigma(T)$ of the composite material is simply a sum of the a-Si:H and nc-Ge conductivities, weighted by the germanium crystal fraction X_{Ge},

$$\sigma(T) = (1 - X_{Ge})\sigma_{Si} + X_{Ge}\sigma_{Ge} \tag{4.2}$$

where σ_{Ge} is the conductivity of a pure nc-Ge sample and σ_{Si} is the conductivity of a pure a-Si:H sample. The resulting thermopower for this system is determined from the number of charge carriers in each phase and their mobilities, so it is weighted not by the volume fractions but by the fractional conductivities of each phase.

$$S(T) = \frac{(1 - X_{Ge})\sigma_{Si}S_{Si} + X_{Ge}\sigma_{Ge}S_{Ge}}{\sigma(T)} \tag{4.3}$$

Figure 4.7 shows a plot of the calculated thermopower for samples with a variety of germanium crystal fractions using the two-band expression, Equation (4.3). The values for σ_{Si} and S_{Si}, and σ_{Ge} and S_{Ge} are taken from measurements from X_{Ge} = 0% (pure a-Si:H) and X_{Ge} = 60% films, respectively. The calculated Seebeck coefficients for samples with X_{Ge} < 10% are negative at most temperatures, and for samples with X_{Ge} > 25%, the calculated Seebeck coefficients are mostly positive. More importantly, for transition samples with 10% < X_{Ge} < 25%, the calculated Seebeck coefficient in Figure 4.7 changes from p-type at low temperatures to n-type at higher temperatures, in general agreement with the data. However, the calculated transition is much more gradual than what is actually observed in Figure 4.5. For samples with X_{Ge} ~ 1-5%, the measured data is overwhelmingly

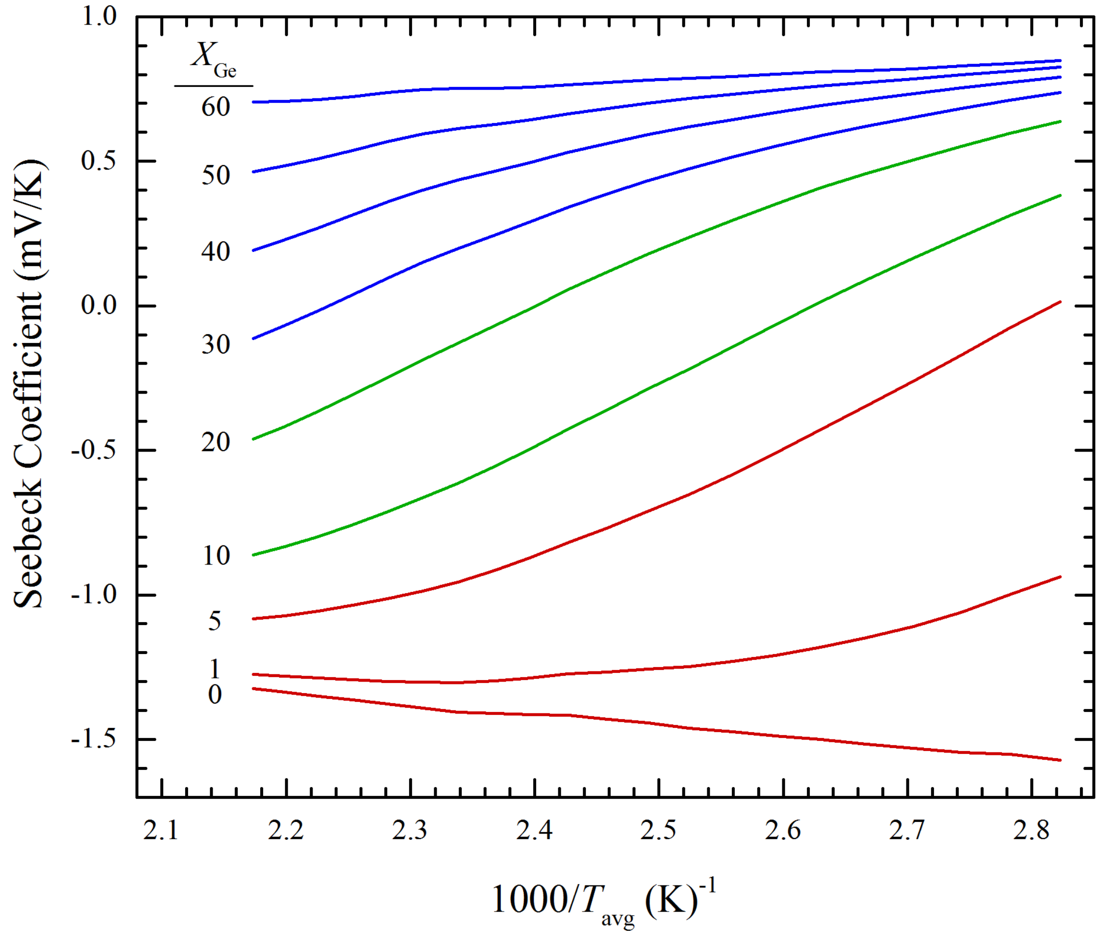

Figure 4.7: Plot of calculated Seebeck coefficient against $1000/T_{avg}$ for temperatures between 350K and 450K and for X_{Ge} = 0 to 60% using the simple volume fraction model, Equation (4.3).

n-type and a-Si:H-like at all temperatures. However, the naïve two-band expression predicts significant influence by the nc-Ge at lower temperatures, which is not seen in the data. Similarly, for samples with X_{Ge} ~ 25-30%, the two-band expression predicts significant influence by the a-Si:H phase at higher temperatures, which also not apparent in the data.

That the model does not grasp the entirety of the physics in these materials is not surprising, however. For example, the two-band model requires that the nc-Ge phase

percolates at all values of X_{Ge}, which is clearly not the case for small X_{Ge}. Simulations for randomly packed hard spheres find that percolation occurs at a volume fraction of ~ 20% [75–77]. However, a recalculation of the thermopower from a standard percolation perspective would not be appropriate either, because the conductivities of the two phases are within a few orders of magnitude of each other. It is therefore reasonable to expect that any non-percolating superclusters of germanium nanocrystals may significantly affect the overall conductivity. Such sub-threshold clusters are normally not discernable in transport data. However, the fact that the two phases have differing signs for their majority carriers allows us to see the effects of non-system spanning clusters at lower X_{Ge} values.

While an exact treatment is difficult, some simple modifications to the two-channel model can significantly improve its accuracy. For $X_{Ge} < 10\%$, both the measured conductivity and thermopower activation energies are constant and similar to those of pure a-Si:H. In this regime, clusters of nanocrystals will not span the entire sample, so any current path that includes a nanocrystal cluster must also pass through the a-Si:H. As a result, those current paths that include nanocrystals would need to overcome the band offsets between the two materials, as sketched in Figure 4.8. This cartoon illustrates the conduction and valence bands at the a-Si:H/nc-Ge heterojunction; the magnitudes of contributions to band offsets from Si-Ge alloying, strain fields and surface charges at the nanocrystal interface are not well known and are not included in this simple sketch. Computer simulations [78,79] and scanning tunneling spectroscopy measurements [80] find that the energy gap of 4 nm Ge nanocrystals is approximately 1.4 eV due to quantum confinement effects. The a-Si:H is n-type and the nanocrystals are p-type, therefore current paths that enter and then exit a nanocrystal would effectively see an n-p-n junction. This

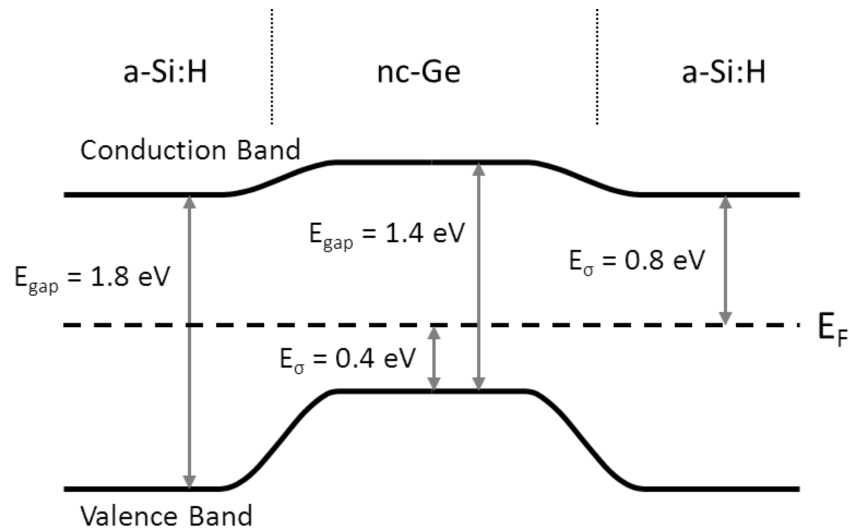

Figure 4.8: Simple sketch of the band offsets for a-Si:H and nc-Ge, assuming equilibrium conditions. The bandgap of nc-Ge is estimated to be 1.4 eV for 4 nm crystals, and the boundaries between the nc-Ge and a-Si:H phases are assumed to be smooth.

would significantly increase the resistance of such current paths, resulting in a smaller current through the germanium nanocrystals than predicted by the two-channel model.

At a particular crystal fraction, the clusters would become sufficiently extended that the higher conductivity of the germanium nanocrystals would begin to outweigh the resistance associated with charge transport into and out of the nanocrystal phase, and conduction would begin to flow through the nanocrystals. This would be particularly important at lower temperatures, where the resistance of the a-Si:H matrix is high. In addition, even once an extended chain of germanium nanocrystals is formed, the conductivity of this phase would be less than expected from the two-channel model because many of the nanocrystals may form dead ends or loops which do not contribute to the conductivty of the Ge phase [77]. Note that in Figure 4.2, the magnitude of the p-type

conductivity curve needed to fit the data for a transition film is ~ 30 times smaller than the conductivity of film with $X_{Ge} > 25\%$ in Figure 4.1.

For $X_{Ge} > 25\%$, we find that there is a much smaller contribution to the thermopower from the a-Si:H phase than predicted by the two-channel model. This means that, while up to 75% of the material is composed of a-Si:H (as determined from Raman measurements), a much smaller fraction appears to contribute to electronic charge transport across the sample. It is possible that the inclusion of Ge nanocrystals disturbs the surrounding a-Si:H, either structurally or electrically, resulting in a shell of non-conducting a-Si:H around each chain of germanium nanocrystals. A non-conducting region may be related to oxidation of the a-Si:H film, which was found to be strongly dependent on X_{Ge} in the FTIR measurements in Section 3.4. This leads to two related effects: first, there should be a drastically decreased contribution to transport from clusters of nanocrystals or a-Si:H regions that do not span the entire sample, assuming the non-conducting shell is wide enough to present a significant tunneling barrier. This has the same effect as the band offset argument above for $X_{Ge} < 10\%$, and the actual case may be a combination of both effects. Second, though the a-Si:H phase would normally percolate across the sample until $X_{Ge} \sim 80\%$, the non-conducting shells would lead to the disruption of a percolating path in the a-Si:H at a smaller value of X_{Ge}. Through a simple calculation, shown in Appendix A, in which a 1.4 nm thick non-conducting shell is added to every Ge nanocrystal, conduction through the a-Si:H would be completely disrupted due to percolation at $X_{Ge} \sim 20\%$.

Not mentioned so far in this discussion is what role, if any, the porosity of the nc-Ge/a-Si:H films plays. Briefly mentioned in Section 3.3, RBS and profilometry measurements from the same samples indicate that as X_{Ge} increases, so does the void

fraction. In fact, as shown in Figure 4.9, the void fraction increases faster than the volume fraction of germanium, and is about 3-4 times larger than the %Ge for all X_{Ge}. For X_{Ge} > 25%, the total volumetric percentage of a-Si:H film (%Si in Figure 4.9) is less than 50%. The presence of voids inside the film should have a significant effect on the ability of the a-Si:H to percolate in films with large X_{Ge}. Accounting for voids, the percolation threshold for the a-Si:H phase is at X_{Ge} ~ 45%, rather than at X_{Ge} ~ 80% as stated above. On its own, however, this doesn't completely resolve the discrepancies between the measured

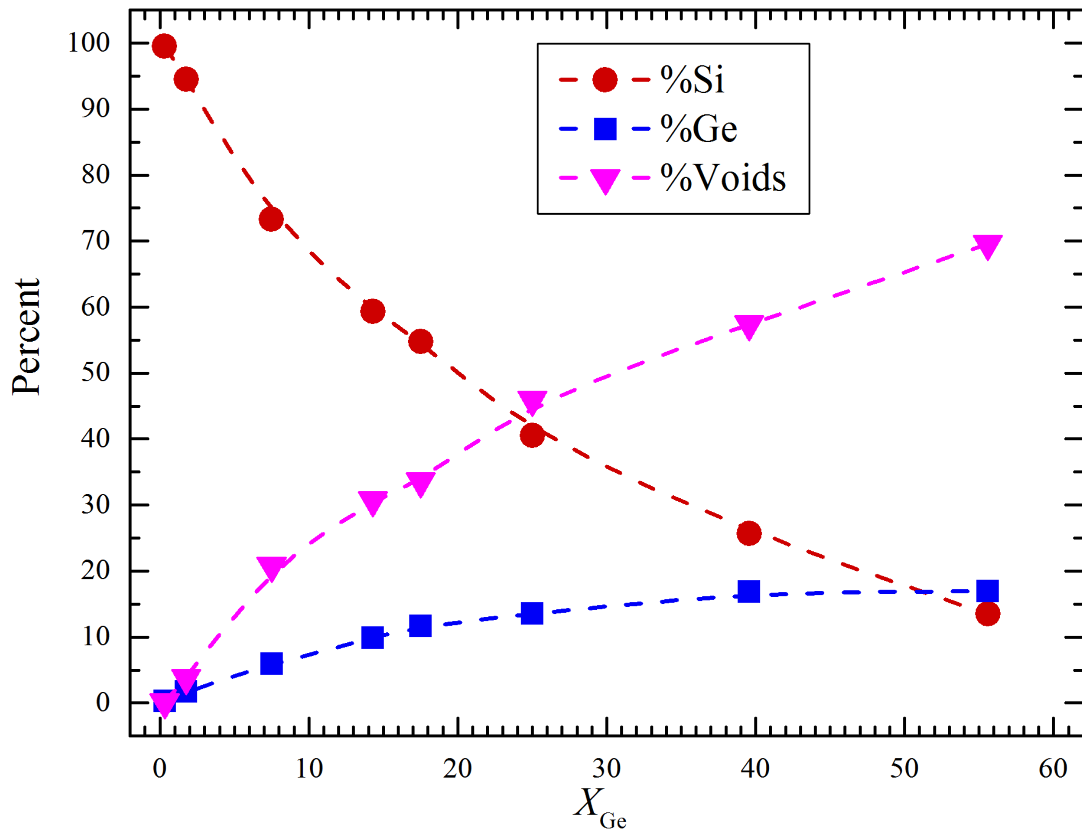

Figure 4.9: Plot of the calculated volume fractions of the a-Si:H phase (%Si), nc-Ge phase (%Ge) and voids as a function of germanium crystal fraction for the eight samples measured by RBS. For each sample, the three phases add to 100%.

thermopower data in Figure 4.5 and the two-band model in Figure 4.7, which suggest the percolation threshold of the a-Si:H phase occurs near X_{Ge} ~ 15 – 25%.

As discussed in Chapter 3, the presence of nc-Ge corresponds with an increase in oxidation of the a-Si:H film. A reasonable postulate is that the oxidation occurs at the surfaces of the voids, which are introduced concurrently with the nc-Ge. The decrease in the conductivity of the a-Si:H phase for $X_{Ge} > 5\%$ may then arise from a layer of partially oxidized amorphous silicon near the void surfaces. A basic calculation of the thickness required to induce a percolation transition in the a-Si:H phase due to a non-conducting shell around the void phase, if one assumes voids of the same size and shape as the germanium nanocrystals, i.e. 4 nm diameter spheres, is performed in Appendix B. The calculation finds a very thin, 0.75 nm or ~ 3 atoms thick, non-conducting shell would be sufficient to meet the percolation threshold in the a-Si:H phase at $X_{Ge} = 25\%$.

If it really is the case that the current passing through the a-Si:H phase is being decreased due to percolation effects as X_{Ge} increases, the magnitude of the conductivity will be noticeably changed in the n-type regime. For small X_{Ge}, in the absence of any percolation effects, the magnitude of the n-type conductivity should decrease linearly with X_{Ge}. However, our measurements find a much faster decrease, shown in Figure 4.10. While the scatter in the data hinders a conclusive determination of the exact functional form of the conductivity decrease, it clearly proceeds faster than linearly, and may be described by an exponential or power law. If the a-Si:H phase reaches its percolation threshold near X_{Ge} ~ 25%, we would expect the decrease in conductivity to follow a power law with critical exponent between 1.6 and 2, as X_{Ge} approaches the percolation threshold [81,82]. The power-law fit line shown in Figure 4.10 has exponent -2, indicating that these

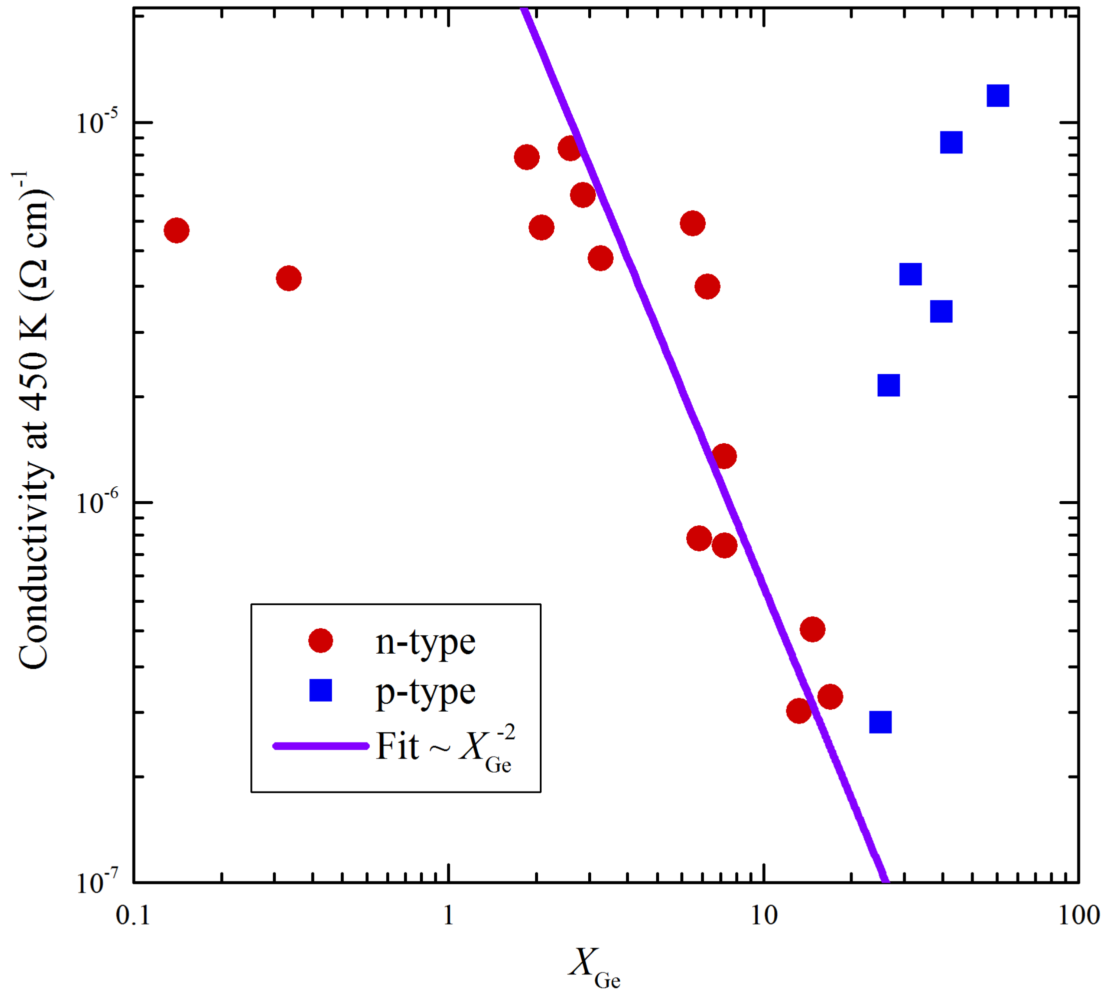

Figure 4.10: Plot of the conductivities at 450 K of a number of samples with different germanium crystal fractions X_{Ge}. Samples that are n-type at 450 K, as measured by the thermopower, are represented as red circles. Samples that are p-type at 450 K are represented as blue squares. The purple line crossing through the n-type data points with $5 < X_{Ge} < 20\%$ is a power-law fit reflecting the expected decrease in the conductivity approaching the percolation threshold of the a-Si:H phase.

measurements are indeed consistent with a percolation threshold of the a-Si:H phase near $X_{Ge} \sim 25\%$.

It is possible to improve on the above calculation of the dual-channel model of Figure 4.7 by incorporating the result of Figure 4.10 into the calculation of the conductivity

in Equation (4.2). The original calculation assumes the conductivity of each phase is independent of the germanium crystal fraction, however, the qualitative arguments above indicate that such an assumption is unrealistic, primarily due to the effects of percolation. To first order, the conductivity of a uniform material is constant far above and zero far below the percolation threshold. Near the percolation threshold, it follows a power-law expression.

At any temperature and germanium crystal fraction, the total conductivity through the sample can be written simply as the sum of the conductivities of the n- and p-type components

$$\sigma(T, X_{Ge}) = \sigma_n(T, X_{Ge}) + \sigma_p(T, X_{Ge}) \tag{4.4}$$

Incorporating percolation effects, the n-type component can be written as

$$\sigma_n(T, X_{Ge}) = (1 - X_{Ge})\sigma_{Si}(T)\xi_n(X_{Ge}) \tag{4.5}$$

where $\xi_n(X_{Ge})$ is a temperature-independent factor accounting for the decrease in conductivity of the n-type phase due to percolation. From Figure 4.10,

$$\xi_n(X_{Ge}) = \begin{cases} 1 & X_{Ge} < 3\% \\ A_n T^{-2} & X_{Ge} > 3\% \end{cases} \tag{4.6}$$

Similarly, the p-type component of the conductivity is

$$\sigma_p(T, X_{Ge}) = X_{Ge}\sigma_{Ge}(T)\xi_p(X_{Ge}) \tag{4.7}$$

and

$$\xi_p(X_{Ge}) = \begin{cases} A_p T^n & X_{Ge} < 30\% \\ 1 & X_{Ge} > 30\% \end{cases} \tag{4.8}$$

where n is estimated from Figure 4.10 to be equal to 5. Both A_n and A_p are chosen so that ξ_n and ξ_p are continuous at 3% and 30%, respectively, though the derivatives of ξ_n and ξ_p are discontinuous. Finally, the Seebeck coefficient is calculated in the same way as Equation (4.3) from the fractional conductivities of each phase, that is,

$$S(T, X_{Ge}) = \frac{\sigma_n(T, X_{Ge}) S_{Si} + \sigma_p(T, X_{Ge}) S_{Ge}}{\sigma(T, X_{Ge})} \tag{4.9}$$

and the results of this revised model are shown in Figure 4.11 for a variety of values of X_{Ge}. In each subplot of Figure 4.11, red curves correspond to $X_{Ge} < 10\%$, green curves to $10 \leq X_{Ge} < 25\%$, and blue curves to $X_{Ge} \geq 25\%$. Figure 4.11a shows the calculated conductivity as a function of $1000/T$ for X_{Ge} between 1 and 60%. Samples with $X_{Ge} < 10\%$ show conductivities that are consistent with an Arrhenius expression with $E_\sigma \sim 0.8$ eV. Samples with $X_{Ge} \geq 25\%$ show conductivities that are consistent with an Arrhenius expression with $E_\sigma \sim 0.4$ eV over the entire temperature range. Samples with $10 \leq X_{Ge} < 25\%$ show curvature indicative of a transition between $E_\sigma \sim 0.8$ eV at high temperatures and $E_\sigma \sim 0.4$ eV at low temperatures. This is in agreement with the measured conductivity activation energies presented in Figure 4.2. Also, the magnitude of the conductivity at high temperature reaches a minimum around $X_{Ge} \sim 15\%$, nearly two orders of magnitude less than at $X_{Ge} \sim 0\%$, in agreement with Figure 4.10.

Figure 4.11b shows the fractional conductivity of the n-type components of the conductivities shows in Figure 4.11a. This presents a clear view of the transition from pure

n-type conduction (red) to pure p-type conduction (blue) and the temperature-dependent transition (green). Figure 4.11c shows the calculated Seebeck coefficients for the same X_{Ge} values as Figure 4.11a and b. Figure 4.11d repeats the measured Seebeck coefficient data already presented in Figure 4.5 for comparison with Figure 4.11c. The calculated Seebeck coefficients in Figure 4.11c show that, for $X_{Ge} < 10\%$, conduction is purely n-type, and for $X_{Ge} > 25\%$, conduction is purely p-type. As revealed in the measurements in Figure 4.11d, the transition occurs only over $10 < X_{Ge} < 25\%$, which is successfully reproduced with the present model. In contrast, the simple dual-channel model of Figure 4.7 shows a transition from n-type to p-type conduction that spans approximately $5 < X_{Ge} < 40\%$.

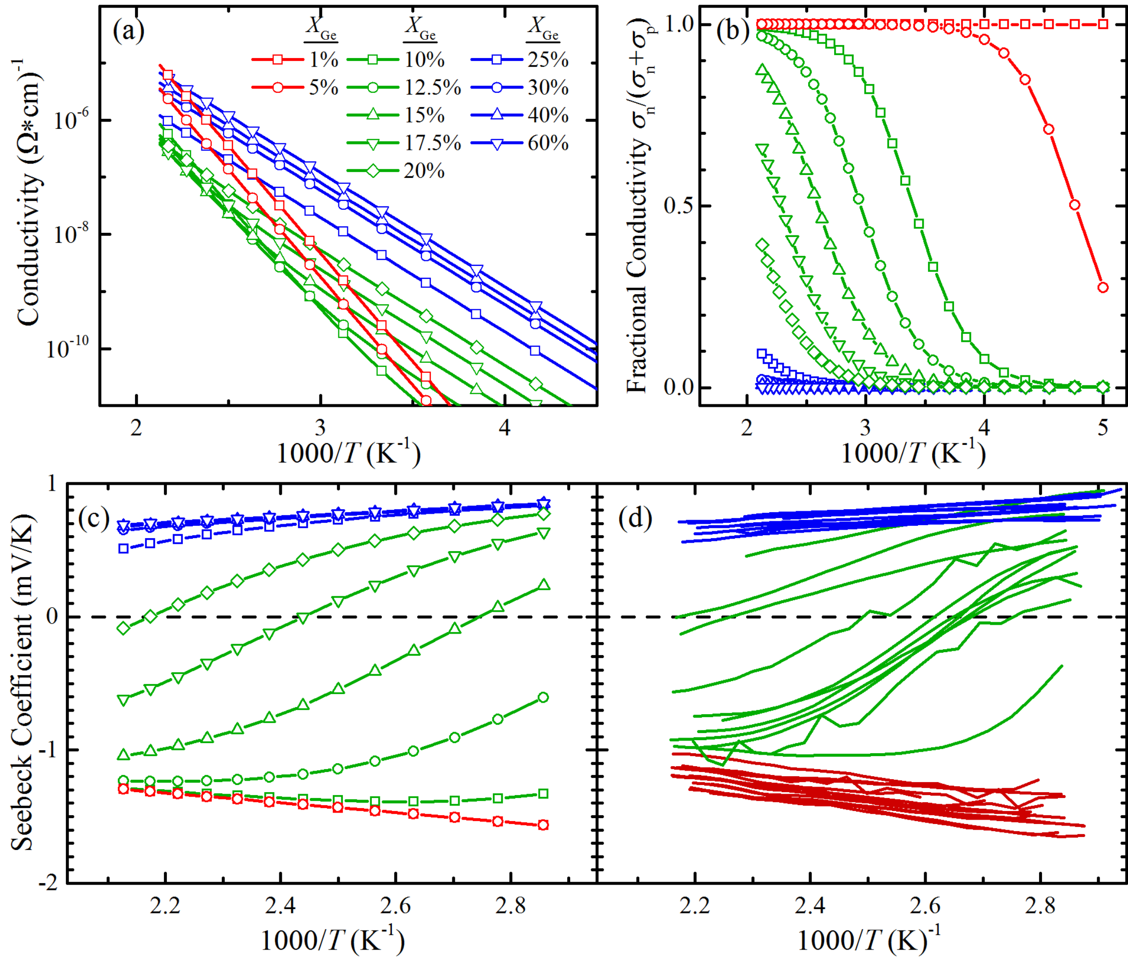

Figure 4.11: Plot of the calculation of the conductivity vs 1000/T using Equation (4.4) (a) for a variety of germanium crystal fractions. Plot of the calculated fraction of conductivity through the n-type phase vs 1000/T (b) for the same values of X_{Ge} in (a). Plot of the calculated Seebeck coefficients vs 1000/T using Equation (4.9) (c) for the same values of X_{Ge} in (a). Plot of the measured Seebeck coefficients vs 1000/T from Figure 4.5 (d).

– Chapter 5 –

Photo-Induced Enhanced Conductivity in nc-Ge/a-Si:H

5.1 – Background

As discussed in Chapter 1, much of the interest in amorphous silicon lies in its promise as the basis for inexpensive photovoltaic devices. The original motivation for embedding silicon nanocrystals in amorphous silicon arose out of an interest in exploring any possible improvements in the transport properties under illumination. Studies of the properties of nc-Ge/a-Si:H films were naturally extended to measurements of the photoconductivity. The work presented in this chapter was done collaboration with Kevin Nangoi, as part of his Senior Honors Thesis in 2013-2014, and it uncovered two results: the germanium nanocrystals suppress the photoconductivity of the amorphous silicon, and the germanium nanocrystals temporarily increase the dark conductivity of the film following light exposure. The first result is not too surprising, as it is reasonable to expect that the interfaces between a-Si:H and nc-Ge is highly disordered, leading to many defect states that can trap electron or holes and lead to very fast recombination rates.

The second result is very surprising, however, and is reminiscent of past measurements on a-Si:H and other disordered systems where Persistent Photoconductivity (PPC) was observed. PPC has been seen in a wide range of materials systems, including AlGaAs alloys [83], ZnCdSe alloys [84,85], conducting polymers such as poly(p-phenylenevinylene) [86], compensated hydrogenated amorphous silicon (a-Si:H) [87], and doping modulated amorphous silicon superlattices [88–90]. The observed magnitude,

temperature dependence and relaxation time of the PPC effect is not identical for these various systems, and accordingly, different models have been proposed to account for these observations. However, all of the systems that display Persistent Photoconductivity have one important feature in common: they are all photoconductive.

The lack of photoconductivity in these nc-Ge/a-Si:H films makes them unique. Consequentially, Persistent Photoconductivity is neither an appropriate name nor description, and a fundamentally new explanation is required. This chapter will detail measurements of the light-induced enhanced conductivity of nc-Ge/a-Si:H films, including a discussion of its dependence on X_{Ge} and its decay after the light has been turned off, followed by a proposal of a possible physical interpretation of these results.

5.2 – Light-Induced Enhanced Conductivity

This section will discuss the generation of the light-induced enhanced conductivity in nc-Ge/a-Si:H films with X_{Ge} between 0 and 30%. As detailed in section 1.2, pure a-Si:H thin films experience a dramatic increase in conductivity when exposed to absorbing illumination. When the film is in state A, after metastable defects have been removed by annealing above 450 K for at least 30 minutes, light exposure causes an increase in the conductivity by 4-6 orders of magnitude as a result of the generation of electron-hole pairs following the absorption of photons with energies larger than the bandgap, 1.8 eV. Due to metastable defect creation (the Staebler-Wronski effect), the photoconductivity decreases as illumination continues, and when the light is turned off, the dark conductivity does not return to its original value, but rather decreases by up to several orders of magnitude below its state A value. The film is termed to be in a metastable state B [22]. The photosensitivity

is typically defined as the ratio of the photoconductivity σ_{ph} to the dark, state A conductivity σ_{A},

$$\text{photosensitivity}(t) \equiv \frac{\sigma_{\text{ph}}(t)}{\sigma_{\text{A}}} \tag{5.1}$$

Calculations of the photosensitivity as a function of light exposure time for a number of nc-Ge/a-Si:H samples are shown in Figure 5.1. For nc-Ge/a-Si:H samples with very low germanium nanocrystal content, $X_{\text{Ge}} < 3\%$, the initial photosensitivity is large, and the photosensitivity decreases as the light exposure time increases due to the SWE, similar to what is seen in pure a-Si:H films. As X_{Ge} increases, the initial photosensitivity decreases, and for large X_{Ge}, there is little or no photosensitivity. A decrease in photoresponse is also found in hydrogenated amorphous Si-Ge alloys produced via PECVD, in which the addition of a small amount of Ge to an a-Si:H film results in a sharp decrease in the photoresponse [91–93]. However, in these materials, the photoresponse remains well above unity regardless of the germanium concentration. The decrease in photoresponse is attributed to the preference of H atoms to bond with Si rather than Ge, resulting in a large defect density from the unhydrogenated Ge atoms [94,95].

Surprisingly, over very long light exposure times (> 24 hours), the photosensitivity appears to increase for samples with $X_{\text{Ge}} > 5\%$. Because σ_{A} is a constant in the calculation of the photosensitivity, the apparent increase in the photosensitivity of these samples must be a result of an increase in the photoconductivity, σ_{ph}.

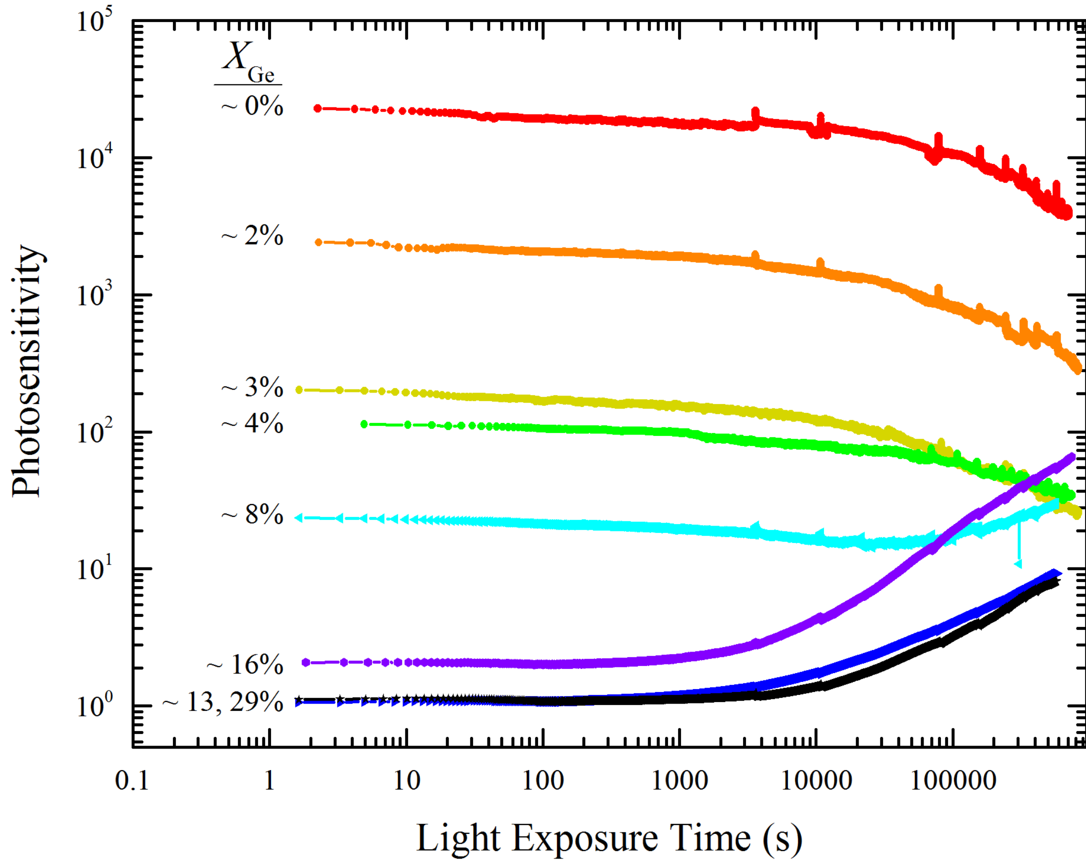

Figure 5.1: Plot of the photosensitivity as a function of light exposure time for multiple nc-Ge/a-Si:H samples. Each photosensitivity curve is calculated from Equation (5.1).

In the measurements for Figure 5.1, the light was turned off at regular intervals during the light exposure and the dark conductivity was measured as a function of time as well, albeit intermittently. The dark conductivity as a function of time during the light exposure is plotted in Figure 5.2, revealing that the apparent increase in the photosensitivity at long time scales in Figure 5.1 is not due to an increase in the photoconductivity at all, but rather an increase in the dark conductivity. It is then appropriate to define the photoresponse as

$$\text{photoresponse}(t) = \frac{\sigma_{\text{ph}}(t)}{\sigma_{\text{dark}}(t)} \quad (5.2)$$

using the dark conductivity at the same time *t* instead of σ_{A}, which is the dark conductivity at $t = 0$. Figure 5.3 shows that the photoresponse, Equation (5.2), does not increase with time, and is equal to unity at all times for the samples with the largest X_{Ge}.

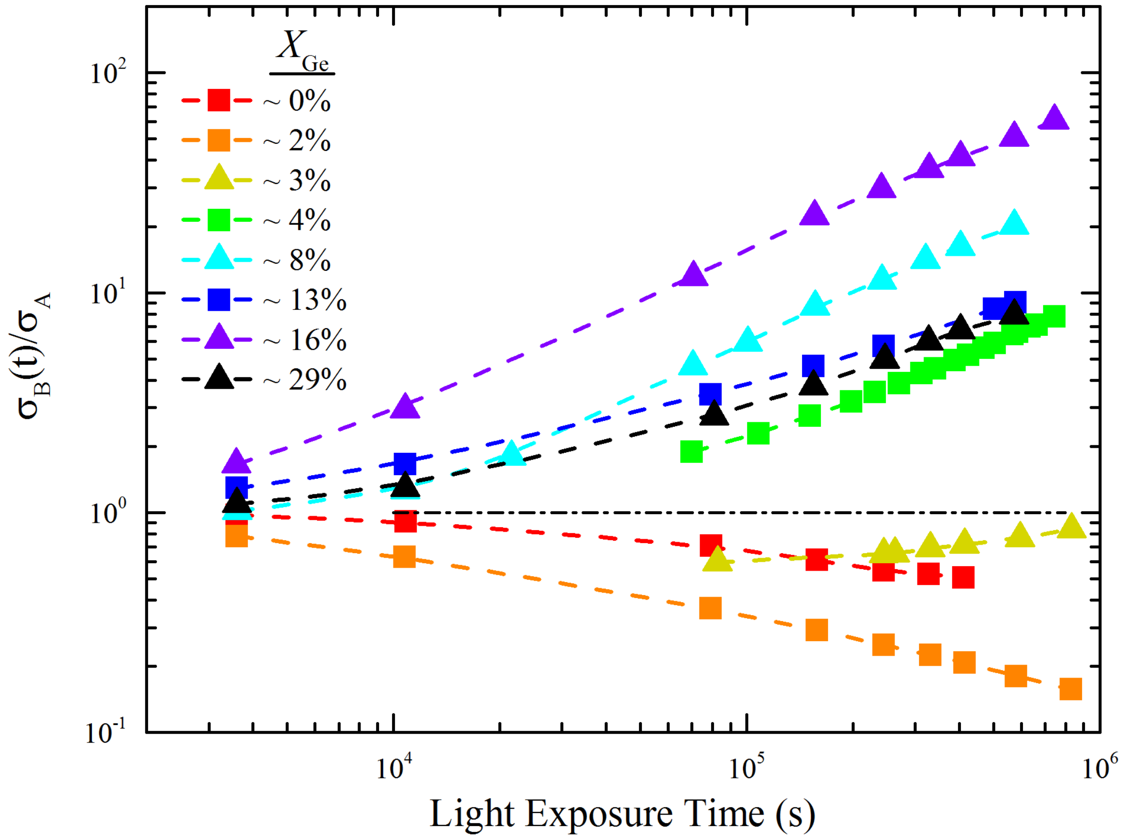

Figure 5.2: Log-log plot of the ratio of the dark current $\sigma_B(t)$ after exposure to light for time *t*, to the initial state A conductivity σ_{A} for a number of nc-Ge/a-Si:H samples. Each data point was taken after turning off the lamp and allowing the sample temperature to stabilize, and the light exposure time is the cumulative time the sample was exposed to the light. The black dash-dotted line marks $\sigma_B / \sigma_A = 1$, that is, no change from the state A conductivity. Samples with the same symbol are from the same deposition run, and this plot combines samples from two different deposition runs.

Samples with very low $X_{Ge} < 2\%$ display optoelectronic behavior very similar to pure a-Si:H, dominated by the Staebler-Wronski Effect. Samples with larger $X_{Ge} > 10\%$ show no Staebler-Wronski Effect and little or no photoresponse, but exhibit a photo-induced enhanced conductivity. For samples with moderate X_{Ge} between 3 and 8%, there is a convolution of the two effects. These samples all display photoresponses larger than unity that decrease with light exposure and dark currents that increase with time. In the case of the sample with $X_{Ge} \sim 3\%$, the dark current initially decreased, then increased after 10^5 seconds (about 1 day). The magnitude of this increase in the dark current in Figure 5.2 loosely correlates with X_{Ge}, but there is significant variation between samples.

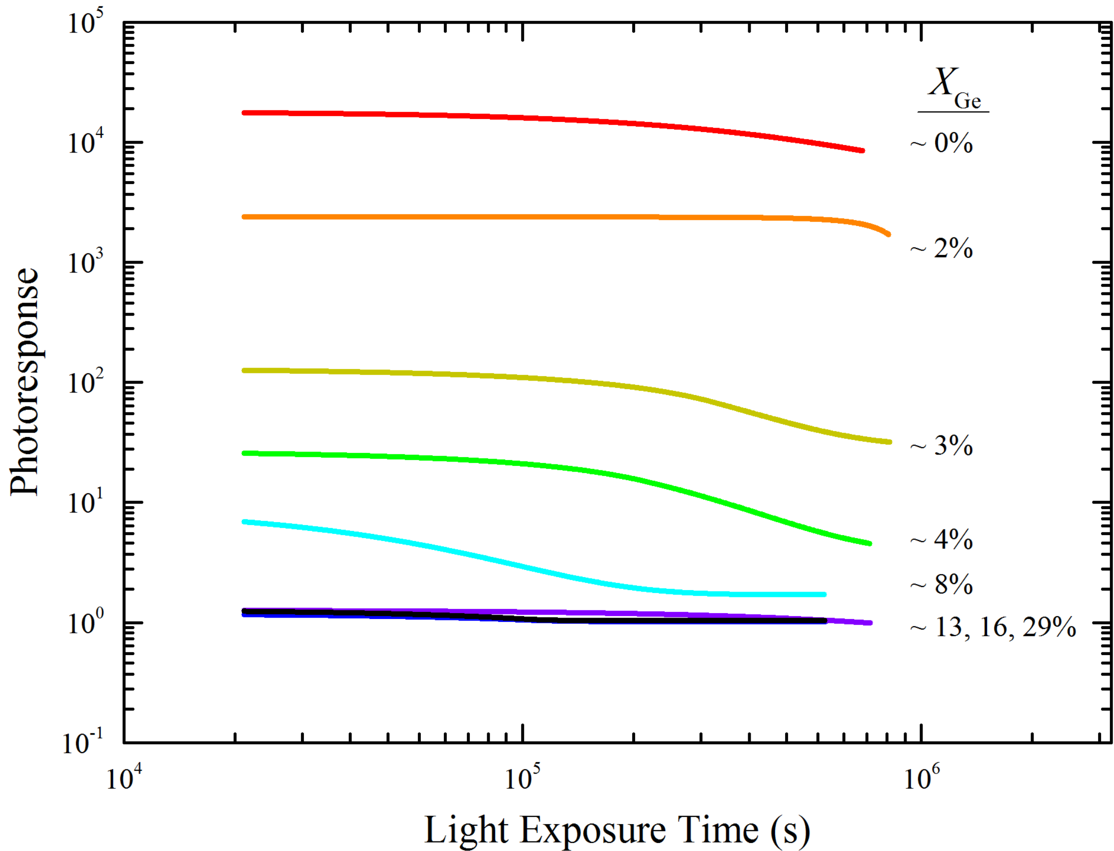

Figure 5.3: Plot of the photoresponse as a function of the cumulative light exposure time, calculated used Equation (5.2), for the data in Figure 5.1 and Figure 5.2.

The symbols in Figure 5.2 denote samples that originate from the same deposition run, and with the exception of the black triangles, $X_{Ge} \sim 29\%$, the inconsistencies disappear when considering only samples within the same deposition run. The sample with $X_{Ge} \sim 29\%$ is a fundamentally different sample from the rest, as it displays p-type conductivity with an activation energy ~0.4 eV. As described in Chapter 4, this sample exhibits conduction through the nc-Ge phase and very little transport is believed to occur through the a-Si:H, unlike the other 7 samples presented here which are all n-type or transition samples.

5.3 – Metastability

The PPC effect in doping modulated amorphous silicon and compensated a-Si:H, as well as the SWE in a-Si:H, is metastable and can be removed by annealing at 470K. In these materials, the annealing time can be quite short, and only thirty minutes at 470K is typically sufficient to remove all metastable light-induced conductance changes and restore the film to its state A condition. In contrast, we have found that anneals of over 17 hours are necessary in order to remove the photo-induced excess conductivity in the nc-Ge/a-Si:H films. That the photo-induced excess conductivity is not removed as easily as other metastable opto-electronic effects is perhaps not surprising, considering that the time scale for the generation of the photo-induced excess conductivity is so long. In Figure 5.1, the time before the excess conductivity becomes noticeable is on the order of tens of hours, while the SWE and other photo-induced metastable characteristics reported previously become significant after minutes or even seconds of illumination.

To investigate the nature of the photo-induced excess conductivity, the decay of the excess conductivity was studied at different temperatures. For these measurements, the

film in state A is illuminated at 320 K for t_{exp} = 8.6 x 10^4 sec, and then the dark current is monitored as a function of time at this fixed temperature. The film is then re-annealed into state A, and cooled to 350 K, where it then receives the same light exposure as before. The time dependence of the dark conductivity after illumination is monitored at this new temperature. This procedure is repeated for measurement temperatures of 380K and 410K.

The results of this measurement for a single sample with X_{Ge} ~ 16% are shown in Figure 5.4, which features a log-linear plot of $\Delta\sigma_B(t)/\Delta\sigma_B(0)$ vs t, where $\Delta\sigma_B(t) = \sigma_B(t) - \sigma_B(t = \infty)$, $\Delta\sigma_B(0) = \sigma_B(0) - \sigma_B(t = \infty)$, $\sigma_B(t = \infty)$ is the extrapolated long-time value of the dark conductivity σ_B following light soaking, and $\sigma_B(0)$ is the dark conductivity 500 sec after illumination is stopped, in order to ensure a stable temperature during the conductivity measurements. That is, the y-axis in Figure 5.4 is the conductivity, normalized to unity at t = 500 sec and to zero at $t = \infty$. When normalized in this manner, a stretched exponential time dependence for σ_B is observed for the SWE in intrinsic a-Si:H [96] as well as the PPC effect in alternating doped multilayer films [97,98] and compensated a-Si:H [99]. That is, for these systems $\Delta\sigma_B(t)/\Delta\sigma_B(0) = \exp[-(t/\tau)^{\beta}]$ where $\beta = T/T_0$ is temperature dependent and less than unity, and T_0 is a material property that is typically around 600 K. In contrast, the decay of the normalized $\Delta\sigma_B(t)/\Delta\sigma_B(0)$ for the nc-Ge/a-Si:H film in Figure 5.4 is well described by a simple exponential time dependence (that is, $\beta = 1$).

More striking is the absence of a temperature dependence in the time constant τ for the decay of the photo-induced excess conductivity in Figure 5.4. For both the PPC effect

and the SWE effect in a-Si:H based materials, the decay time constant is thermally activated $\tau = \tau_0 \exp[E_\tau / k_B T]$, where ε_τ is the activation energy, k_B is Boltzmann's constant and T is the temperature. Studies of the SWE in a-Si:H find E_τ = 0.94 eV, [98] while PPC in doping modulated a-Si:H multilayers exhibited a decay with E_τ = 1.1 eV [22] and E_τ = 0.55 eV in compensated a-Si:H [100]. In contrast to these systems, the time dependence of the relaxation of the photo-induced excess conductivity in

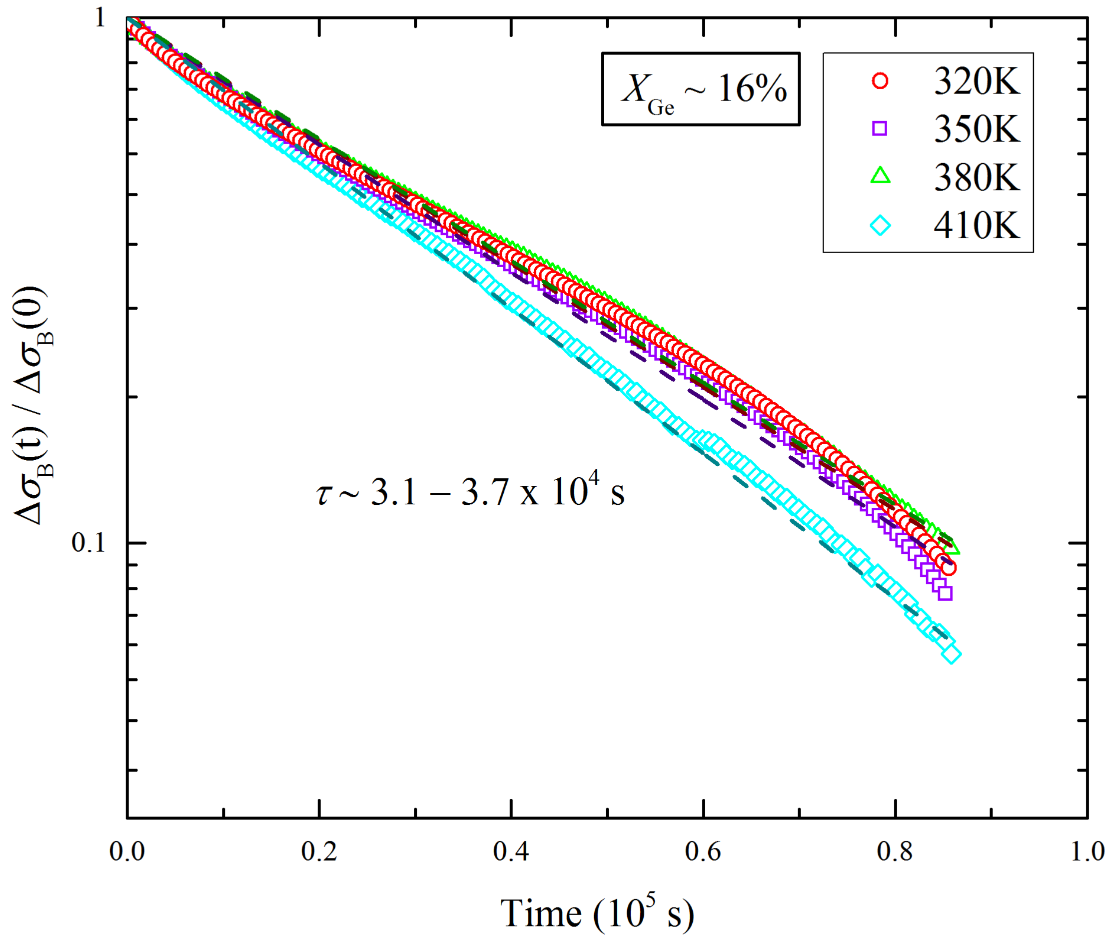

Figure 5.4: Log-linear plot of the decay of the photo-enhanced excess conductivity versus time for a single film with $X_{Ge} \sim 16\%$. The y-axis is the dark conductivity measured after 24 hours of illumination, normalized to 1 at $t = 0$ and to zero at $t = \infty$. The dashed lines are exponential fits to each curve, which represents the decay at temperatures between 320 K and 410 K.

nc-Ge/a-Si:H is temperature independent between 320 and 410 K, where τ is 3.1 – 3.7 x 10^4 seconds. As shown in the Arrhenius plot of the decay time τ in Figure 5.5, the relaxation of the photo-induced excess conductivity for nc-Ge/a-Si:H is characterized by E_τ ~ 0 eV. This accounts for the much longer 'annealing time' necessary to restore the state A conductivity in this film, as the elevated temperature is not significant.

5.4 – Discussion

This section will address a possible mechanism for the light-induced enhancement of the dark conductivity in nc-Ge/a-Si:H. The photo-induced excess conductivity observed in nc-Ge/a-Si:H is unlike other light-induced metastable conductance changes observed in amorphous silicon-based material systems. Studies of light-induced conductivity changes

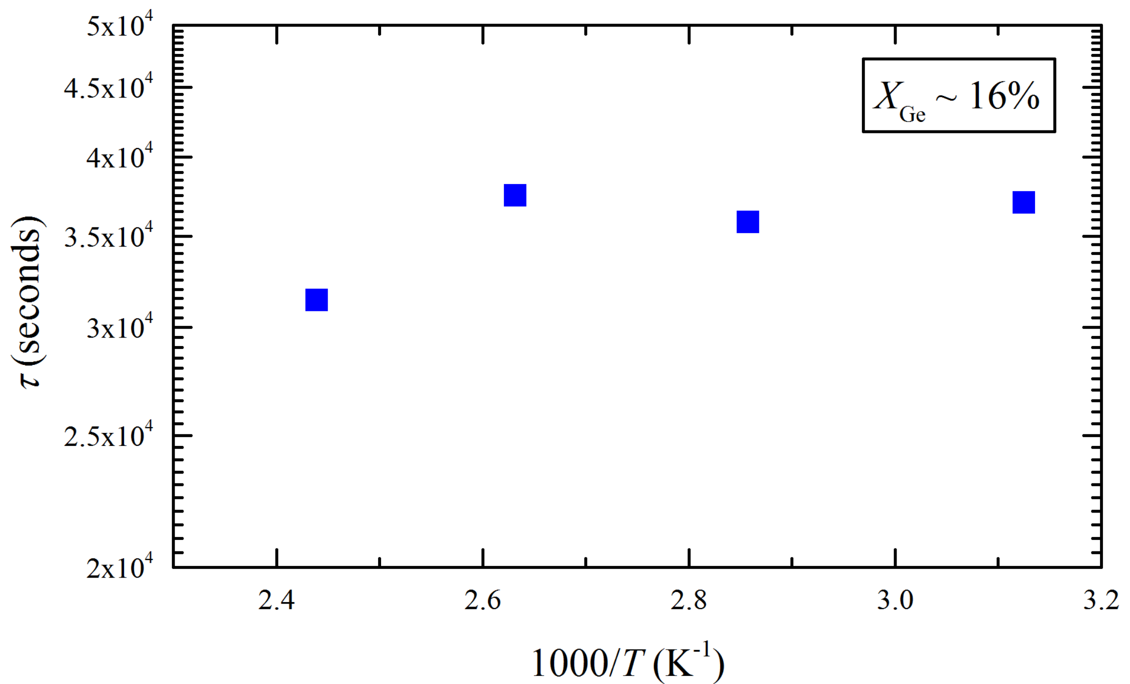

Figure 5.5: Arrhenius plot of the values of τ found for each curve in Figure 5.4, plotted versus 1000/*T*.

in a-Si:H based materials suggest that hydrogen motion plays an important role in both the PPC and SWE effects. The observed stretched exponential relaxation and activation energy of ~ 1 eV for the decay time constant for the PPC and SWE effects have been shown to be in quantitative agreement with measurements of the hydrogen diffusion coefficient in amorphous silicon. In contrast, the simple exponential decay and temperature-independent lifetime observed in nc-Ge/a-Si:H indicates that hydrogen motion is unlikely to be involved in the photo-induced excess conductivity effect described here. Instead, the temperature-independent relaxation of the excess conductivity state suggests that a tunneling process governs the removal of this effect.

The other striking difference between the effect described here and other light-induced metastabilities in a-Si:H-based systems is the absence of a photocurrent in nc-Ge/a-Si:H. The lack of a photoresponse indicates that the density of recombination centers in materials with large X_{Ge} is high enough to quench any photocurrent. In a-Si:H the most common type of recombination center is a dangling bond defect, that is, a silicon atom with only three covalent bonds to the surrounding network. As the concentration of germanium nanocrystals is increased, the photoresponse of the resulting composite film decreases uniformly, until a photoresponse of unity is found for $X_{Ge} \geq 13\%$. A similar decrease in photosensitivity has been observed in a-Si:H containing silicon nanocrystalline inclusions fabricated in the same dual-chamber co-deposition system, though for the a/nc-Si:H films the photosensitivity is ~ 10^2 even for films with crystalline content of 10 – 20% [13]. For these films the reduction in photoconductivity is associated with an increase in dangling bond density, as reflected in electron spin resonance and constant photocurrent spectroscopy measurements [101]. Preliminary measurements on the nc-Ge/a-Si:H

samples presented here using the constant photocurrent method show an increase in the midgap density of states, as well as a decreased bandtail slope as X_{Ge} is increased. It is thus not unreasonable that the decrease in photoresponse seen here is also due to additional dangling bonds introduced into the composite film with the nc-Ge inclusions.

We therefore suggest the following speculative model. When germanium nanocrystals are embedded in the a-Si:H film, they introduce many dangling bond defects in the surrounding material. Upon light exposure, this excess of dangling bond defects causes very rapid recombination of photo-generated electron-hole pairs, decreasing the photoresponse. Simultaneously, any metastable defect creation due to the Staebler-Wronski Effect is overwhelmed by the large defect density already present. This draws a parallel to the opto-electronic response in unhydrogenated amorphous silicon, which has no photoresponse or SWE due to its large density of midgap defects.

In the nc-Ge/a-Si:H films, a fraction of the defects may reside in or near the grain boundary regions surrounding the nanocrystalline inclusions. In fact, following the discussion in Section 3.4, it is likely that the defect density is larger in the a-Si:H surrounding germanium nanocrystals, compared to the bulk a-Si:H film far from any nanocrystal inclusions. As sketched in Figure 4.8, it is energetically favorable for free holes to reside in the nanocrystalline germanium phase, while free electrons achieve a lower energy in the amorphous silicon phase. If a photo-generated hole is trapped at a defect site in the grain boundary of a germanium nanocrystal, the hole would have a probability of tunneling into the nanocrystal itself, thereby becoming unavailable for recombination with a photo-excited electron, which would remain in the a-Si:H phase.

The effect of this tunneling process would be to add additional free electrons to the surrounding a-Si:H matrix during illumination which would remain after the illumination is stopped, along with excess holes added to the nc-Ge. As discussed in Chapter 4, thermopower studies of the nc-Ge/a-Si:H films show that the a-Si:H is n-type, while conduction through the nc-Ge is p-type. This charge trapping process would enhance the conductivity of both the amorphous silicon and nanocrystalline germanium phases. The enhanced conductivity would persist until the holes tunnel out of the nc-Ge back into the a-Si:H, at which point they are able to recombine with the excess electrons. This process is similar to the one put forth to account for PPC in compensated a-Si:H and doping modulated amorphous silicon multilayer films, but in these systems the metastable hole trap is associated with boron-complexes that undergo a structural reorientation upon charged trapping [87]. Studies of the photo-induced excess conductivity as a function of nc-Ge concentration and surface treatment of the nanocrystalline inclusions are underway to further elucidate this tentative theory.

– Chapter 6 –

Non-Arrhenius Conductivity

This chapter returns to the conductivity measurements performed on the nc-Ge/a-Si:H films originally presented in Section 4.1. While the previous discussion described the conductivity in the context of understanding the influence of adding more germanium nanocrystals to the a-Si:H film, this section focuses on a more fundamental question: by what mechanism does charge transport occur through these samples? Of course, this question was answered in Section 4.1, where I claimed that transport in both n- and p-type samples (that is, $X_{Ge} < 10$ % and $X_{Ge} > 25\%$) was thermally activated with E_{σ} ~ 0.8 eV and ~ 0.4 eV, respectively. This chapter will show that transport in these films is in fact not thermally activated, and a theory that more accurately describes the conductivity data, developed for a-Si:H in the 1980s, will be described.

6.1 – Results

In thermally activated transport processes, the conductivity depends exponentially on the inverse of the temperature, that is, an Arrhenius plot of σ vs. T gives a straight line where the slope is the activation energy E_{σ}. Close inspection of the n- and p-type conductivity curves (red circles and blue squares, respectively) in Figure 4.1 reveal that there is a very slight curvature. On its own, this slight curvature would not be sufficient justification to question whether transport is indeed thermally activated. Previously published studies of the temperature dependence of a-Si:H films commonly display larger deviations from a straight line, or do not have dense enough data points to make a definitive

claim one way or another [3,22,26,27,102,103]. In these cases, the data is described well enough by an Arrhenius expression that other common transport mechanisms such as Mott or Efros-Shklovskii variable-range hopping are excluded from consideration. However, the reduced activation energy calculations in the inset of Figure 4.1 are very sensitive to any curvature in the original data, and it is in these plots that consistent deviations from an Arrhenius expression can be identified. Figure 6.1 shows log-log plots of the reduced activation energy calculations vs. temperature for four nc-Ge/a-Si:H samples from different deposition runs, with X_{Ge} from 3 to 29%. Each plot shows calculations of the reduced activation energy for potential conductivity temperature dependences of the form

$$\sigma(T) = \sigma_1 \exp[-(T_0/T)^{\kappa}] \tag{6.1}$$

where κ is equal to -1 (gray), -3/4 (green) or -1/2 (violet) for different nc-Ge/a-Si:H samples. Each of the three model curves presents a straight line in a log-log plot of the reduced activation energy vs. temperature, and the slope of the line is equal to the value of κ. When κ = -1, Equation (6.1) simplifies to the expression for thermally activated conduction, as in Equation (1.2). When κ = -1/2, the expression for Efros-Shklovskii variable-range hopping is recovered, and κ = -1/4, which is not shown in Figure 6.1, would correspond to Mott variable-range hopping. All four samples in Figure 6.1 display a conductivity temperature dependence that is inconsistent with the κ = -1 and κ = -1/2 model curves, and match very closely to the κ = -3/4 model curve.

Figure 6.2 shows the conductivity data from the n-type sample in Figure 3.9, plotted against 1000/T (violet) and $T^{-3/4}$ (green). The black lines overlaying the data are both straight lines, and the plot vs 1000/T shows noticeable curvature over the entire temperature

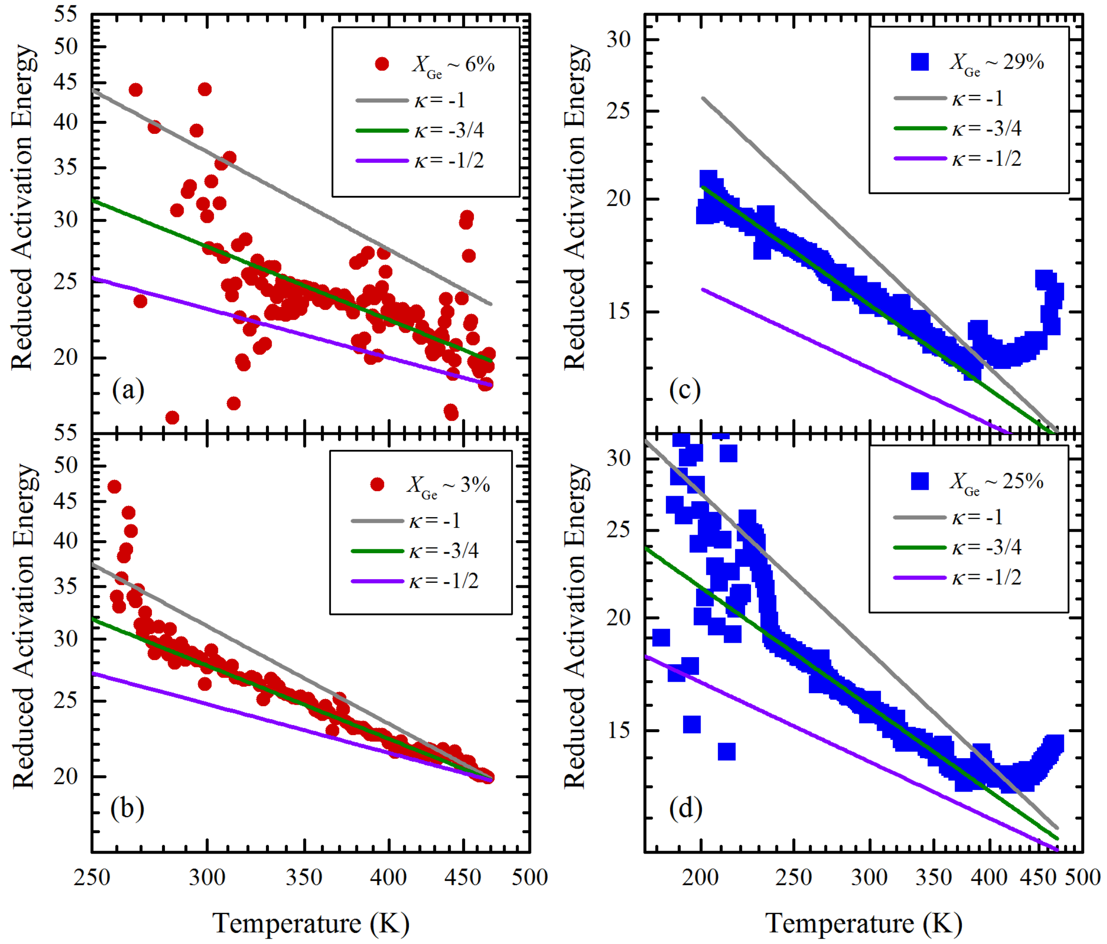

Figure 6.1**:** Log-log plots of the reduced activation energy versus temperature for four nc-Ge/a-Si:H samples with germanium concentrations as determined by Raman measurements included. Overlaid on each plot are model curves of the form $\sigma(T) = \sigma_1 \exp[-(T_0/T)^\kappa]$ where κ is equal to -1 (gray), -3/4 (green) and -1/2 (violet).

range, while the plot vs $T^{-3/4}$ shows no detectable curvature. These analyses were performed on a number of nc-Ge/a-Si:H samples, and in no case did the conductivity data match the thermally activated expression, κ = -1. In every case, κ = -3/4 more closely matched the data, however κ = -3/4 does not correspond to any commonly seen or well-understood theory of conduction in disordered semiconductors.

For nc-Ge/a-Si:H samples with $X_{Ge} > 25\%$, conduction occurs through percolating chains of germanium nanocrystals; the boundaries of each nanocrystal may present significant barriers to conduction. One expects that adjacent nanocrystals would not have matching crystal lattice directions, creating a narrow region of disordered material, and oxidation may present a potential barrier between nanocrystals as well. For these reasons and more, it is perhaps unsurprising that the expression for thermally activated conduction does not match the measured data. For the samples with $X_{Ge} < 10\%$, however, conduction occurs only through the a-Si:H phase, and a-Si:H has been described as displaying

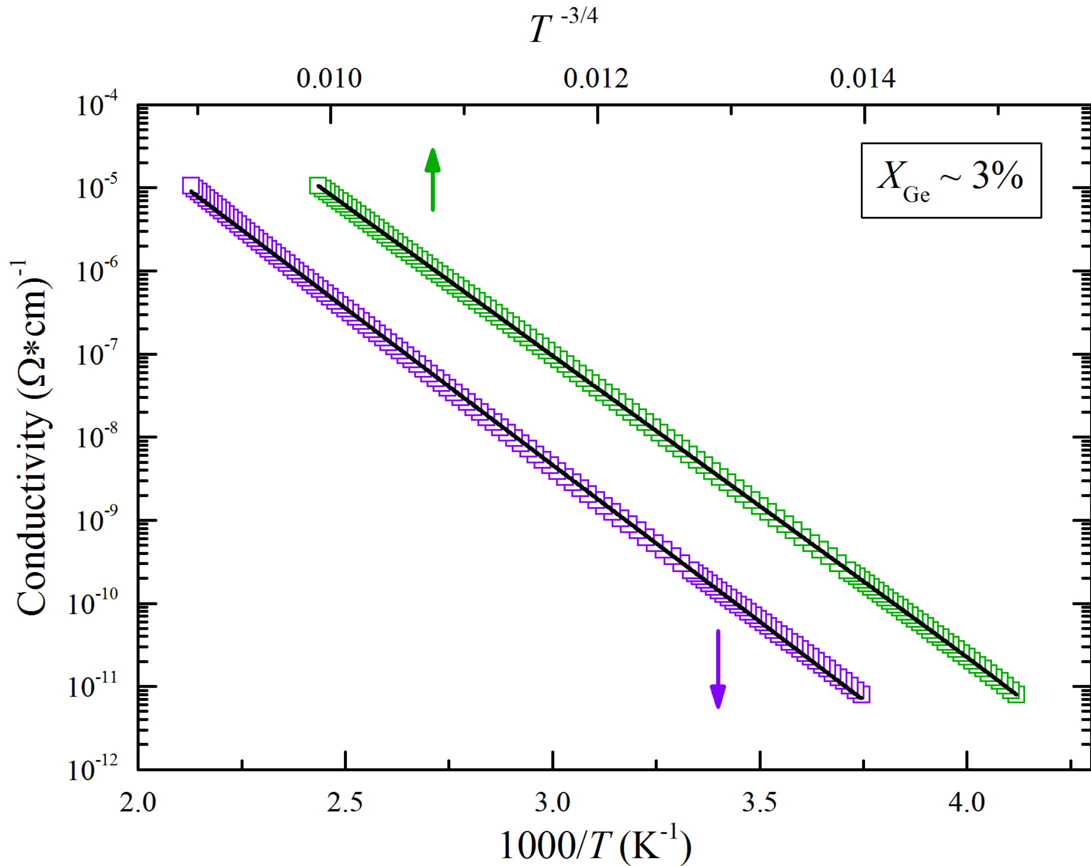

Figure 6.2**:** Plot of the temperature dependence of the conductivity of a nc-Ge/a-Si:H sample with X_{Ge} ~ 3%, when plotted against T^{-1} (violet curve) and $T^{-0.82}$ (green curve).

thermally activated conduction for decades. If there are regions of enhanced disorder in the a-Si:H due to nearby nc-Ge, the conductivity of these regions would be degraded relative to the bulk of the a-Si:H phase. These regions would then play little to no role in the total conductivity of the sample, especially for samples with very small X_{Ge}, as in the case of the sample in Figure 6.2. At any rate, it is quite simple to determine if the curvature seen in the conductivity of the n-type samples is due to the presence of the nc-Ge in the material by measuring a sample that has no germanium nanocrystals.

Figure 6.3 plots the reduced activation energy vs. temperature in a log-log plot for a pure a-Si:H sample that has no nanocrystals of any kind. This sample was grown in a single-chamber PECVD system from the decomposition of silane gas at low pressure and power, as described in Section 1.1.1. Between room temperature and 400 K, a fit is found in which $\kappa = -0.76$, and the data is clearly inconsistent with thermally activated conduction ($\kappa = -1$) or Efros-Shklovskii VRH ($\kappa = -1/2$), just as in nc-Ge/a-Si:H samples with $X_{Ge} < 10\%$.

A summary of the conductivity measurements and Zabrodskii plots for a variety of samples is shown in Table I. The table is split into five groups: pure a-Si:H samples which were grown in a single-chamber configuration, nc-Ge/a-Si:H samples which show no detectable nc-Ge content in Raman measurements, a/nc-Si:H samples which are a-Si:H films with embedded Si nanocrystals instead of Ge nanocrystals, and nc-Ge/a-Si:H samples with $X_{Ge} < 10\%$ and $X_{Ge} > 25\%$. When fit to a simple thermally activated temperature dependence, the activation energies for groups 1-4 are near 0.75 – 0.8 eV, consistent with what is typically found for undoped a-Si:H [16,26]. For group 5, the activation energy is

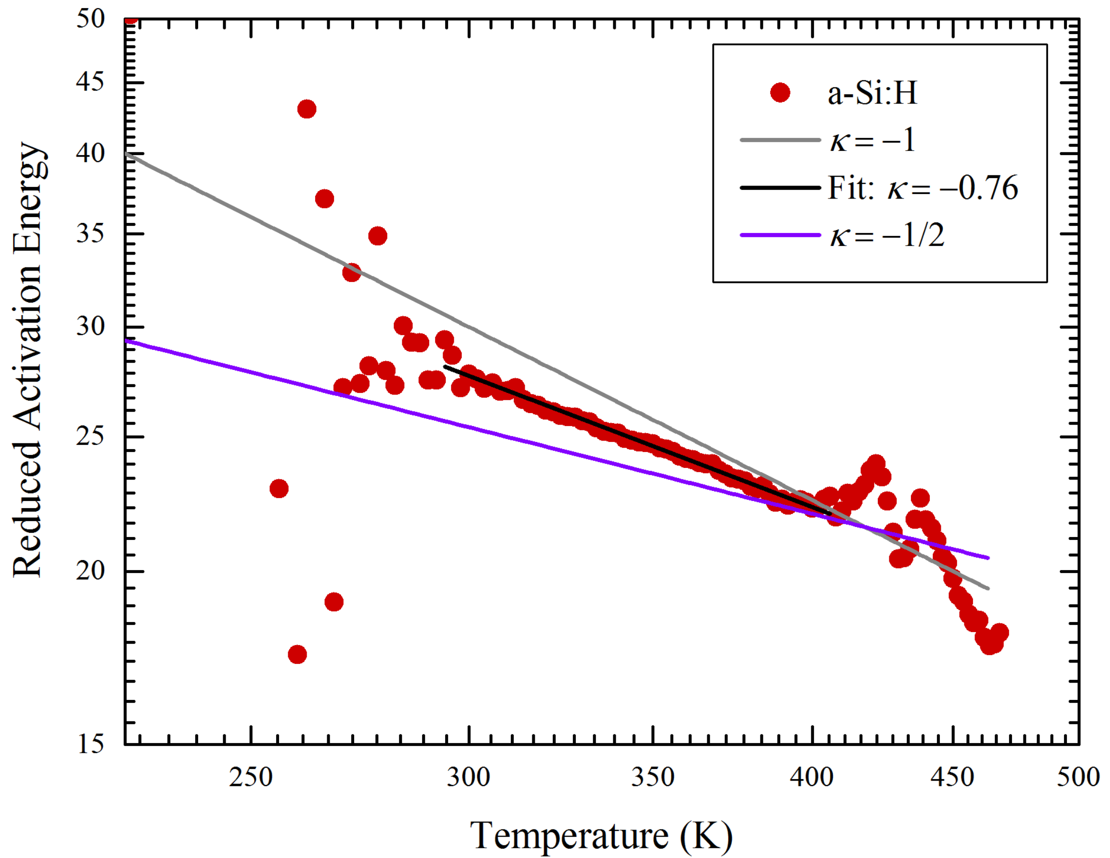

Figure 6.3**:** Log-log plot of the reduced activation energy for an a-Si:H sample with no Ge nanocrystals, against temperature. Also shown is the expected reduced activation energy for a T^{-1} (gray) and $T^{-1/2}$ (violet) temperature dependence, and a fit to the data (black).

around 0.4 eV, as described in Section 4.1. However, the power-law exponent obtained from the reduced activation energy analysis for all five groups is never found to be -1. For the films in Table I, the κ values are closer to -0.75, however there is a fair amount of scatter in the exact values. It appears that groups 1-4 have similar values of κ, all between 0.71 and 0. 84, with the exception of sample 4d. Group 5 samples, in which the conduction path is fundamentally different, appear to have smaller vales of κ, though further study is necessary to make these potential trends certain. However, the results summarized in Table

I indicate that the conductivity is best described by Equation (6.1), where κ is near 0.75 – 0.8. As a check on our analysis procedure, and the system in which these measurements were made, a low-defect intrinsic c-Si wafer was measured in the same system. The reduced activation energy analysis found a power-law exponent of -0.96, consistent with Arrhenius behavior with a weakly temperature-dependent conductivity pre-factor.

Table I: Results of fits to $\sigma(T) = \sigma_0 \exp[E_\sigma / k_B T]$ and $\sigma(T) = \sigma_1 \exp[-(T_0 / T)^\kappa]$ for a variety of samples.

Sample Group		Sample	σ_0	E_σ	σ_1	κ
1	pure a-Si:H	a	6.81E+3	0.761	1.08E+8	0.741
		b	5.37E+2	0.747	1.42E+6	0.764
		c	3.82E+3	0.802	1.42E+6	0.843
		d	1.04E+3	0.662	9.75E+4	0.830
2	nc-Ge/a-Si:H $X_{Ge} = 0\%$	a	2.37E+4	0.820	1.05E+7	0.813
		b	2.03E+3	0.779	1.67E+7	0.743
		c	5.09E+3	0.747	1.24E+8	0.722
		d	8.27E+2	0.720	8.17E+4	0.844
3	a/nc-Si:H	a	6.76E+2	0.790	5.72E+6	0.737
		b	5.83E+2	0.680	1.83E+3	0.747
4	nc-Ge/a-Si:H $X_{Ge} < 10\%$ n-type	a	2.78E+3	0.775	2.62E+3	0.789
		b	9.79E+2	0.756	2.59E+3	0.795
		c	1.19E+3	0.744	1.55E+3	0.708
		d	5.93E+1	0.745	5.21E+3	0.905
5	nc-Ge/a-Si:H $X_{Ge} > 25\%$ p-type	a	8.35E-2	0.476	1.15E+3	0.750
		b	9.82E-2	0.419	8.19E+2	0.695
		c	7.01E-2	0.453	5.94E+2	0.639
		d	1.87E-1	0.430	1.01E+3	0.736

6.2 – Discussion

Previous studies on disordered non-metallic thin films have also found conductivities described by Equation (6.1) with values of κ near 0.75. An exponent $\kappa \sim 0.75 \pm 0.05$ was observed in the conductivity of ultra-thin disordered films of Ag, Bi, Pb and Pd below 20 K [104], which, it was suggested, could result from the collective variable range hopping model of Fisher *et a*. [105]. This model was developed in the context of superconductor vortices, but can be adapted to disordered semiconductors. Additionally, in samples of weakly coupled Au nanoparticles and ZnO quantum dot arrays, values of κ were reported very close to 2/3 [106,107], which were ascribed to a modified Efros-Shklovskii VRH which includes nonresonant tunneling based on local energy fluctuations. Both of the systems in references [106] and [107] bear similarity to the nc-Ge/a-Si:H samples with $X_{\mathrm{Ge}} > 25\%$, and indeed the values of κ seen for these samples in Table I are near to 2/3.

For samples in which conduction occurs through the a-Si:H phase, that is, Groups 1-4 in Table I, while the collective VRH model from reference [105] cannot be excluded, a more promising theory is one suggested for transport in a-Si:H. This is a model proposed by Monroe [108], and independently by Grünewald and Thomas [109] in which conduction occurs via variable-range hopping through an exponential density of states, as in the bandtails of a-Si:H. This model is distinguished from the VRH formulations of Mott and Efros-Shklovskii in that it involves a different density of states; furthermore, the hopping current flows through states near a "transport energy" that may be far from the Fermi

energy, while the Mott and Efros-Shklovskii VRH models describe hopping through states near the Fermi energy.

The transport energy model is usually thought to describe electronic transport in a-Si:H at temperatures below 300 K, while at higher temperatures, conduction occurs via electrons thermally activated above a mobility edge. It may be the case, however, that the temperature at which activated conduction dominates is much higher in most a-Si:H samples. As mentioned in Section 1.2 and sketched in Figure 1.4, a-Si:H has an exponential density of states in the bandtails

$$g(\varepsilon) = \frac{N}{\varepsilon_0} \exp[-\varepsilon / \varepsilon_0] \tag{6.2}$$

where ε is measured from the conduction band edge with $\varepsilon > 0$ inside the bandgap, ε_0 is the bandtail width and N is the total density of states, as determined from optical spectroscopy and time of flight measurements [110,111]. Far from the Fermi energy, the carrier concentration at ε is given by

$$dn(\varepsilon) = g(\varepsilon) \exp\left[\frac{\varepsilon - \varepsilon_F}{kT}\right] d\varepsilon \tag{6.3}$$

where the factor $\exp[(\varepsilon - \varepsilon_F)/kT]$ is the Fermi function at ε, and $0 < \varepsilon < \varepsilon_F$. When the bandtail width ε_0 is larger than kT, the carrier concentration increases as ε moves into the bandgap from the conduction band mobility edge. Following the discussion by Shklovskii *et al.* [112], the conductivity at ε is

$$d\sigma(\varepsilon) \sim dn(\varepsilon)D(\varepsilon) \tag{6.4}$$

where $D(\varepsilon)$ is the electron diffusion coefficient at ε given by

$$D(\varepsilon) = \frac{1}{6}R^2(\varepsilon)\nu(\varepsilon) \tag{6.5}$$

$R(\varepsilon)$ is the average distance between nearest neighbor states at ε,

$$R(\varepsilon) = N^{-1/3}\exp\left[\frac{\varepsilon}{3\varepsilon_0}\right] \tag{6.6}$$

for an exponential density of states, while $\nu(\varepsilon)$ is the hopping rate at ε,

$$\nu(\varepsilon) = \nu_0 \exp\left[\frac{-2R}{a}\right] \tag{6.7}$$

and a is the distance between adjacent atoms. Because $\nu(\varepsilon)$ is the exponential of an exponential and dominates in Equation (6.5), $D(\varepsilon)$ decreases with a faster than exponential energy dependence as ε moves away from the mobility edge into the bandgap. The product $dn(\varepsilon)D(\varepsilon)$ in Equation (6.4) is a sharply peaked function at some energy, called the transport energy, where the vast majority of conduction occurs. The transport energy can be calculated as

$$\varepsilon_t = 3\varepsilon_0 \ln\left[\frac{a}{2}N^{1/3}\left(\frac{3\varepsilon_0}{kT} - 1\right)\right] \tag{6.8}$$

provided that $3\varepsilon_0 > kT$. For high temperatures or steep bandtail slopes where ε_0 is small, the solution for ε_t vanishes and conduction is dominated by carriers thermally excited to and above the mobility edge. At moderate temperatures where Equation (6.8) is still valid, the transport energy ε_t shifts towards the conduction band edge as temperature increases. As a first approximation, the conductivity is described by an Arrhenius expression, where ε_t is a temperature-dependent activation energy, that is,

$$\sigma(T) = \sigma_0 \exp\left[-\frac{\varepsilon_t}{k_B T}\right] \tag{6.9}$$

and an Arrhenius plot of σ vs T^{-1} displays curvature similar to that seen in Figure 6.2.

A somewhat more complete calculation of the conductivity is possible by considering transport only through states a width $W = \sqrt{6\varepsilon_0 k_B T}$ from the transport energy, and assuming Equations (6.3) – (6.8) are constant over that width. A result from that calculation is plotted in Figure 6.4 along with the data from the sample with X_{Ge} ~ 3% in Figure 6.2 and Figure 6.1b, using the following parameters: ε_0 = 50 meV, $N = 10^{20}$ cm^{-3}, a = 1.5 nm, ε_F = 0.85 eV and ν_0 = 10^{15} s^{-1}. These values were chosen to achieve a close fit in Figure 6.4a, and are all within reason for an a-Si:H film. Notably, the transport energy model results in a conductivity temperature dependence that is identical to Equation (6.1), as evidenced by the straight line in the reduced activation energy calculation of Figure 6.4a. In Figure 6.4b, the model and measurement data are not artificially offset, and while the model predicts the correct average activation energy E_σ, it underestimates the conductivity prefactor σ_0 in the Arrhenius expression, Equation (1.2), by a factor of about 30; however,

the mobility edge model also predicts a value for σ_0 which is smaller than that found in measurements, but by around 3 orders of magnitude [113].

Small adjustments to any of the input parameters can change the resulting calculated values of E_σ and κ, but for conduction bandtail widths between 30 – 60 meV, κ is generally between 0.9 – 0.7, in good agreement with the experimental results summarized in Table I. Hydrogenated amorphous silicon thin films frequently exhibit Urbach energies between 50 – 100 meV [114], which implies conduction bandtail widths of 25 – 50 meV, in reasonable agreement with our calculations. It is important to note that while simulations based on Equations (6.3) –(6.8), when plotted as in Figure 6.4, agree with our observations, this model does not provide closed-form expressions for κ or T_0 in terms of material parameters for a-Si:H. A more complete theory for Equation (6.8), either involving variable-range hopping through exponential bandtail states or some other conduction mechanism is needed.

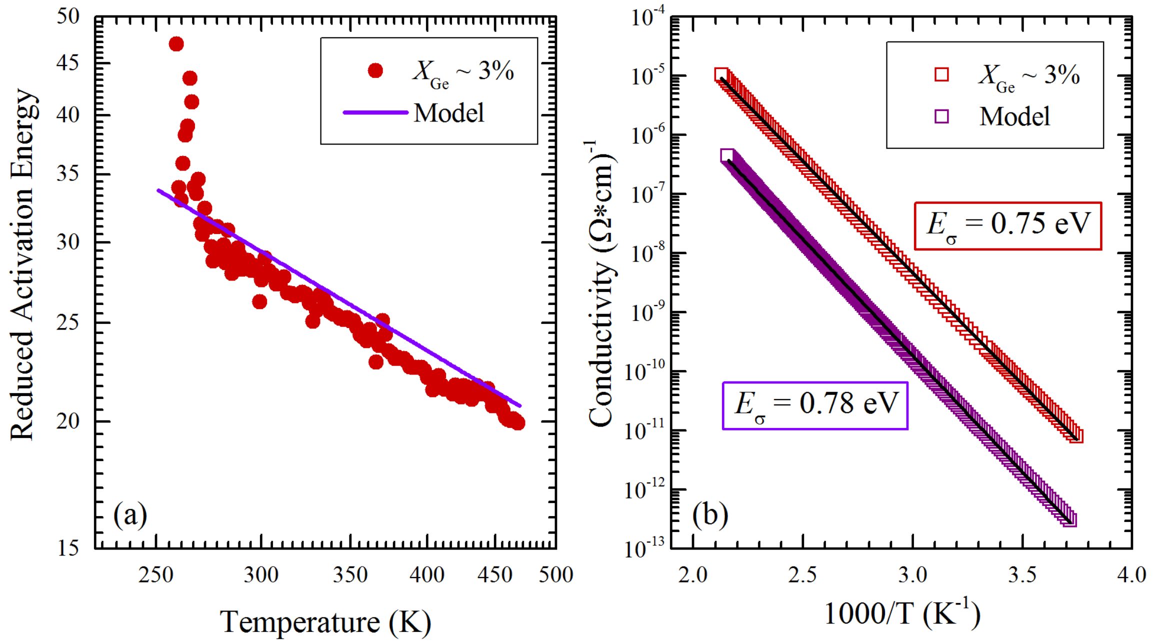

Figure 6.4**:** (a) Log-log plot of the reduced activation energy versus temperature and (b) Arrhenius plot of the conductivity versus 1000/*T* for the sample in Figure 6.1a and Figure 6.2. In both of these figures, the data is shown in red and the transport energy model is shown in violet. In Figure 6.4b, the black lines represent best fits to an Arrhenius temperature dependence, yielding average activation energies E_σ = 0.75 and 0.78 eV for the data and model, respectively.

– Chapter 7 –

Conclusions

In this thesis, I have described the synthesis and characterization of nc-Ge/a-Si:H thin films, composed of hydrogenated amorphous silicon with embedded germanium nanocrystals. These samples are fabricated in a dual-chamber dual-plasma co-deposition PECVD system, in which the nc-Ge are synthesized in an upstream reactor and injected into a separate downstream plasma in which the a-Si:H thin film grows. The nc-Ge are dispersed and embedded in the growing a-Si:H film such that a series of samples is produced in which only the concentration of nc-Ge is varied. Raman spectroscopy measurements are used to determine the nc-Ge concentration X_{Ge}, and samples with X_{Ge} between 0 and 75% are studied. FTIR measurements indicate that the disorder of the a-Si:H film increases as X_{Ge} increases, and there is a concurrent increase in the level of oxidation present in the film.

Measurements of the dark conductivity and thermopower on these samples indicate a transition from transport through the a-Si:H phase to transport through the nc-Ge phase as X_{Ge} increases. The transition is gradual, occurring between $10 < X_{Ge} < 25\%$, and within that regime, a temperature-dependent transition is also observed such that n-type transport is seen at high temperatures and p-type transport at low temperatures. For small $X_{Ge} < 10\%$, the conductivity is nearly thermally activated with activation energy $E_\sigma \sim 0.8$ eV and the thermopower is n-type with activation energy $E_S \sim -0.4$ eV, similar to previous reports of undoped a-Si:H. For large $X_{Ge} > 25\%$, the conductivity is nearly thermally activated with

activation energy $E_{\sigma} \sim 0.4$ eV and the thermopower is p-type with activation energy $E_S \sim + 0.2$ eV, consistent with previous reports on germanium nanocrystals. The conductivity in the intermediate regime $10 < X_{Ge} < 25\%$ is adequately described by the sum of conduction paths through the a-Si:H and nc-Ge.

The complete transition from n-type to p-type transport, measured by the thermopower, can be modeled using a modified version of a dual-channel picture, in which the conductivity of each phase is weighted by X_{Ge}, but is also constrained by percolation. Accordingly, for $X_{Ge} < 20\%$, the nc-Ge phase does not percolate across the sample, so conduction through that phase is decreased. However, a corresponding percolation threshold of the a-Si:H phase is found close to $X_{Ge} \sim 15 - 25\%$, rather than at $X_{Ge} \sim 80\%$ as would be expected if the percolation problem was reversed. It is suggested that this discrepancy is related to the increased disorder and oxidation in the a-Si:H phase when the nc-Ge are introduced into the sample.

Measurements of the conductivity changes of these samples due to exposure to illumination reveal that the concentration of nc-Ge corresponds with a sharp decrease in the photoresponse, and samples with $X_{Ge} > 10\%$ exhibit no increase in conductivity upon the onset of illumination. It is suggested that the increase in the disorder of the a-Si:H phase due to nearby nc-Ge increases the recombination rate, preventing photo-generated free electron-hole pairs from contributing to conduction. Unexpectedly, however, samples with $X_{Ge} > 2\%$ exhibit an increase in the dark conductivity following exposure to illumination. A model is proposed in which photo-generated free holes in the a-Si:H phase tunnel into the nc-Ge phase, preventing recombination with free electrons. This model is in qualitative

agreement with measurements of the decay of the photo-induced excess conductivity, which find an exponential decay with a temperature-independent decay rate.

Detailed measurements of the temperature dependence of the conductivity of n-type and p-type nc-Ge/a-Si:H samples, as well as pure a-Si:H samples reveal a subtle but consistent variation from the thermally activated expression. The conductivity temperature dependence is more accurately described by the expression $\sigma(T) = \sigma_1 \exp[-(T_0/T)^{\kappa}]$, where κ is near 0.75. These results are in close agreement with a model put forth in the mid-1980s describing hopping through bandtail states in a-Si:H.

References

[1] C. C. Wu, S. D. Theiuss, G. Gu, M.-H. Lu, J. C. Sturm, S. Wagner, and S. R. Forrest, IEEE Electron Device Lett. **18**, 609 (1997).
[2] C. R. Wronski, B. Von Roedern, and A. Kołodziej, Vacuum **82**, 1145 (2008).
[3] R. C. Chittick, J. H. Alexander, and H. F. Sterling, J. Electrochem. Soc. **116**, 77 (1969).
[4] N. M. Johnson, C. E. Nebel, P. V. Santos, W. B. Jackson, R. A. Street, K. S. Stevens, and J. Walker, Appl. Phys. Lett. **59**, 1443 (1991).
[5] W. M. M. Kessels, R. J. Severens, A. H. M. Smets, B. A. Korevaar, G. J. Adriaenssens, D. C. Schram, and M. C. M. van de Sanden, J. Appl. Phys. **89**, 2404 (2001).
[6] A. A. Howling, J.-L. Dorier, C. Hollenstein, U. Kroll, and F. Finger, J. Vac. Sci. Technol. A **10**, 1080 (1992).
[7] P. A. Longeway, R. D. Estes, and H. A. Weakliem, J. Phys. Chem. **88**, 73 (1984).
[8] G. Ganguly and A. Matsuda, Phys. Rev. B **47**, 3661 (1993).
[9] T. Nakashita, A. Inoue, S. Hagiwara, F. Uehara, and K. Kohno, Jpn. J. Appl. Phys. **31**, 1730 (1992).
[10] Y. Bouizem, A. Belfedal, J. D. Sib, A. Kebab, and L. Chahed, J. Phys. Condens. Matter **17**, 5149 (2005).
[11] W. A. Turner, S. J. Jones, D. Pang, B. F. Bateman, J. H. Chen, Y.-M. Li, F. C. Marques, A. E. Wetsel, P. Wickboldt, W. Paul, J. Bodart, R. E. Norberg, I. E. Zawawi, and M. L. Theye, J. Appl. Phys. **67**, 7430 (1990).
[12] L. Mangolini, E. Thimsen, and U. Kortshagen, Nano Lett. **5**, 655 (2005).
[13] Y. Adjallah, C. Anderson, U. Kortshagen, and J. Kakalios, J. Appl. Phys. **107**, 043704 (2010).
[14] W. Schülke, Philos. Mag. Part B **43**, 451 (1981).
[15] A. D’Amico, G. Fortunato, and C. M. Van Vliet, Solid-State Electron. **28**, 837 (1985).
[16] R. A. Street, *Hydrogenated Amorphous Silicon* (Cambridge University Press, 2005).
[17] P. G. Le Comber, A. Madan, and W. E. Spear, J. Non-Cryst. Solids **11**, 219 (1972).
[18] A. H. Mahan, J. Carapella, B. P. Nelson, R. S. Crandall, and I. Balberg, J. Appl. Phys. **69**, 6728 (1991).
[19] W. E. Spear and P. G. Le Comber, Solid State Commun. **17**, 1193 (1975).
[20] P. G. Le Comber, D. I. Jones, and W. E. Spear, Philos. Mag. **35**, 1173 (1977).
[21] H. M. Dyalsingh and J. Kakalios, Phys. Rev. B **54**, 7630 (1996).
[22] D. L. Staebler and C. R. Wronski, Appl. Phys. Lett. **31**, 292 (1977).
[23] L. K. Wagner and J. C. Grossman, Phys. Rev. Lett. **101**, 265501 (2008).
[24] N. F. Mott, Adv. Phys. **16**, 49 (1967).
[25] H. Overhof and W. Beyer, Philos. Mag. Part B **43**, 433 (1981).
[26] J. Jang, C. H. Choi, and C. Lee, J. Non-Cryst. Solids **51**, 129 (1982).
[27] T. A. Abtew, M. Zhang, Y. Pan, and D. A. Drabold, J. Non-Cryst. Solids **354**, 2909 (2008).
[28] N. F. Mott, J. Non-Cryst. Solids **1**, 1 (1968).

[29] A. L. Efros and B. I. Shklovskii, J. Phys. C Solid State Phys. **8**, L49 (1975).
[30] J. Zhang and B. I. Shklovskii, Phys. Rev. B **70**, 115317 (2004).
[31] L. R. Wienkes, C. Blackwell, and J. Kakalios, Appl. Phys. Lett. **100**, 072105 (2012).
[32] N. F. Mott and E. A. Davis, *Electronic Processes in Non-Crystalline Materials* (Oxford University Press, 2012).
[33] T. D. Moustakas, J. Electron. Mater. **8**, 391 (1979).
[34] H. J. Goldsmid and R. W. Douglas, Br. J. Appl. Phys. **5**, 386 (1954).
[35] H. J. Goldsmid, CERN Doc. Serv. (1964).
[36] A. F. Joffe and L. S. Stil'bans, Rep. Prog. Phys. **22**, 167 (1959).
[37] M. Stutzmann, W. B. Jackson, and C. C. Tsai, Phys. Rev. B **32**, 23 (1985).
[38] H. M. Branz, Phys. Rev. B **59**, 5498 (1999).
[39] R. Biswas, B. C. Pan, and Y. Y. Ye, Phys. Rev. Lett. **88**, 205502 (2002).
[40] D. Redfield, Appl. Phys. Lett. **54**, 398 (1989).
[41] S. Zhang and H. Branz, Phys. Rev. Lett. **87**, 105503 (2001).
[42] S. R. Jadkar, J. V. Sali, S. T. Kshrisagar, and M. G. Takwale, Thin Solid Films **437**, 18 (2003).
[43] J. Kakalios, U. Kortshagen, C. Blackwell, C. Anderson, Y. Adjallah, L. R. Wienkes, K. Bodurtha, and J. Trask, MRS Online Proc. Libr. **1321**, null (2011).
[44] H. Richter and L. Ley, J. Appl. Phys. **52**, 7281 (1981).
[45] V. Paillard, P. Puech, M. A. Laguna, R. Carles, B. Kohn, and F. Huisken, J. Appl. Phys. **86**, 1921 (1999).
[46] S. Hayashi, M. Ito, and H. Kanamori, Solid State Commun. **44**, 75 (1982).
[47] G. Viera, S. Huet, and L. Boufendi, J. Appl. Phys. **90**, 4175 (2001).
[48] R. Meyer and D. Comtesse, Phys. Rev. B **83**, 014301 (2011).
[49] D. Bermejo and M. Cardona, J. Non-Cryst. Solids **32**, 405 (1979).
[50] W. K. Choi, V. Ng, S. P. Ng, H. H. Thio, Z. X. Shen, and W. S. Li, J. Appl. Phys. **86**, 1398 (1999).
[51] G. Amato, F. Fizzotti, C. Manfredotti, P. Menna, G. Nobile, and R. Spagnolo, Phys. Status Solidi B **170**, 119 (1992).
[52] G. Lucovsky, R. J. Nemanich, and J. C. Knights, Phys. Rev. B **19**, 2064 (1979).
[53] C. Manfredotti, F. Fizzotti, M. Boero, P. Pastorino, P. Polesello, and E. Vittone, Phys. Rev. B **50**, 18046 (1994).
[54] K. K. Gleason, M. A. Petrich, and J. A. Reimer, Phys. Rev. B **36**, 3259 (1987).
[55] M. Cardona, Phys. Status Solidi B **118**, 463 (1983).
[56] P. Scherrer, Nachr Ges Wiss Gött. **2**, 96 (1918).
[57] P. D. Persans, A. F. Ruppert, B. Abeles, and T. Tiedje, Phys. Rev. B **32**, 5558 (1985).
[58] F. Yndurain, Phys. Rev. Lett. **37**, 1062 (1976).
[59] U. K. Das, P. Chaudhuri, and S. T. Kshirsagar, J. Appl. Phys. **80**, 5389 (1996).
[60] P. O'Keeffe, Y. Aoyagi, S. Komuro, T. Kato, and T. Morikawa, Appl. Phys. Lett. **66**, 836 (1995).
[61] F. Yun, B. . Hinds, S. Hatatani, S. Oda, Q. . Zhao, and M. Willander, Thin Solid Films **375**, 137 (2000).
[62] R. Street, J. Electron. Mater. **22**, 39 (1993).
[63] B. Zhang, S. Shrestha, M. A. Green, and G. Conibeer, Appl. Phys. Lett. **97**, 132109 (2010).
[64] A. G. Zabrodskii and I. S. Shlimak, Sov. Phys. Semicond. **9**, 391 (1975).

[65] The measured slope in the Zabrodskii plots for these films is slightly less than -1, and will be discussed in detail elsewhere., (n.d.).
[66] T. H. Geballe and G. W. Hull, Phys. Rev. **94**, 1134 (1954).
[67] A. E. Middleton and W. W. Scanlon, Phys. Rev. **92**, 219 (1953).
[68] T. Hanrath and B. A. Korgel, J. Phys. Chem. B **109**, 5518 (2005).
[69] S. Zhang, E. R. Hemesath, D. E. Perea, E. Wijaya, J. L. Lensch-Falk, and L. J. Lauhon, Nano Lett. **9**, 3268 (2009).
[70] J.-S. Park, B. Ryu, C.-Y. Moon, and K. J. Chang, Nano Lett. **10**, 116 (2010).
[71] J. Xiang, W. Lu, Y. Hu, Y. Wu, H. Yan, and C. M. Lieber, Nature **441**, 489 (2006).
[72] W. Lu, J. Xiang, B. P. Timko, Y. Wu, and C. M. Lieber, Proc. Natl. Acad. Sci. U. S. A. **102**, 10046 (2005).
[73] A. D. Stewart, D. I. Jones, and G. Willeke, Philos. Mag. Part B **48**, 333 (1983).
[74] D. K. C. MacDonald, *Thermoelectricity: An Introduction to the Principles* (Courier Dover Publications, 1962).
[75] W. J. Frith and R. Buscall, J. Chem. Phys. **95**, 5983 (1991).
[76] M. J. Powell, Phys. Rev. B **20**, 4194 (1979).
[77] B. I. Shklovskii and A. L. Efros, in *Electron. Prop. Doped Semicond.* (Nauka, Moscow, 1979), pp. 111–126.
[78] C. Bulutay, Phys. Rev. B **76**, 205321 (2007).
[79] B. H. Koh, E. W. H. Kan, W.-K. Chim, W. K. Choi, D. A. Antoniadis, and E. A. Fitzgerald, J. Appl. Phys. **97**, 124305 (2005).
[80] Y. Nakamura, K. Watanabe, Y. Fukuzawa, and M. Ichikawa, Appl. Phys. Lett. **87**, 133119 (2005).
[81] B. I. Shklovskiĭ and A. L. Éfros, Sov. Phys. Uspekhi **18**, 845 (1975).
[82] P. A. Lightsey, Phys. Rev. B **8**, 3586 (1973).
[83] M. I. Nathan, Solid-State Electron. **29**, 167 (1986).
[84] O. Ray, I. P. Smorchkova, and N. Samarth, Phys. Rev. B **59**, 9810 (1999).
[85] H. X. Jiang and J. Y. Lin, Phys. Rev. B **40**, 10025 (1989).
[86] C. H. Lee, G. Yu, and A. J. Heeger, Phys. Rev. B **47**, 15543 (1993).
[87] S. C. Agarwal and S. Guha, Phys. Rev. B **32**, 8469 (1985).
[88] J. Kakalios and H. Fritzsche, Phys. Rev. Lett. **53**, 1602 (1984).
[89] M. Hundhausen and L. Ley, Phys. Rev. B **32**, 6655 (1985).
[90] F.-C. Su, S. Levine, P. E. Vanier, and F. J. Kampas, Appl. Phys. Lett. **47**, 612 (1985).
[91] Y.-P. Chou and S.-C. Lee, J. Appl. Phys. **83**, 4111 (1998).
[92] K. D. Mackenzie, J. R. Eggert, D. J. Leopold, Y. M. Li, S. Lin, and W. Paul, Phys. Rev. B **31**, 2198 (1985).
[93] G. Nakamura, K. Sato, and Y. Yukimoto, Sol. Cells **9**, 75 (1983).
[94] A. Morimoto, T. Miura, M. Kumeda, and T. Shimizu, Jpn. J. Appl. Phys. **20**, L833 (1981).
[95] M. Kumeda, Y. Tsujimura, Y. Yonezawa, A. Morimoto, and T. Shimizu, Solid State Commun. **55**, 409 (1985).
[96] W. B. Jackson and J. Kakalios, Phys. Rev. B **37**, 1020 (1988).
[97] A. J. Hamed, Phys. Rev. B **44**, 5585 (1991).
[98] B. Everitt and J. Kakalios, Phys. Rev. B **43**, 6820 (1991).
[99] B.-S. Yoo, Y.-H. Song, C. Lee, and J. Jang, Phys. Rev. B **41**, 10787 (1990).
[100] H. Mell and W. Beyer, J. Non-Cryst. Solids **59–60, Part 1**, 405 (1983).

[101] L. Wienkes, A. Besaw, C. Anderson, D. Bobela, P. Stradins, U. Kortshagen, and J. Kakalios, MRS Online Proc. Libr. **1245**, null (2010).
[102] P. Chaudhuri, S. Ray, and A. K. Barua, Thin Solid Films **113**, 261 (1984).
[103] W. Beyer and H. Overhof, Solid State Commun. **31**, 1 (1979).
[104] N. Marković, C. Christiansen, D. E. Grupp, A. M. Mack, G. Martinez-Arizala, and A. M. Goldman, Phys. Rev. B **62**, 2195 (2000).
[105] M. P. A. Fisher, T. A. Tokuyasu, and A. P. Young, Phys. Rev. Lett. **66**, 2931 (1991).
[106] A. Zabet-Khosousi, P.-E. Trudeau, Y. Suganuma, A.-A. Dhirani, and B. Statt, Phys. Rev. Lett. **96**, 156403 (2006).
[107] A. J. Houtepen, D. Kockmann, and D. Vanmaekelbergh, Nano Lett. **8**, 3516 (2008).
[108] D. Monroe, Phys. Rev. Lett. **54**, 146 (1985).
[109] M. Grünewald and P. Thomas, Phys. Status Solidi B **94**, 125 (1979).
[110] W. B. Jackson and N. M. Amer, Phys. Rev. B **25**, 5559 (1982).
[111] T. Tiedje, J. M. Cebulka, D. L. Morel, and B. Abeles, Phys. Rev. Lett. **46**, 1425 (1981).
[112] B. I. Shklovskii, E. I. Levin, H. Fritzsche, and S. D. Baranovskii, Adv. Disord. Semicond. 161 (1990).
[113] W. E. Spear, D. Allan, P. L. Comber, and A. Ghaith, Philos. Mag. Part B **41**, 419 (1980).
[114] W. B. Jackson and N. M. Amer, J. Phys. Colloq. Orsay Fr. **42**, C4 293 (1981).

Appendices

Appendix A

The nearest neighbor distances in Si and Ge are very close, 0.235 and 0.245 nm, respectively. For these basic calculations, I will treat these as equal, such that both phases have an atomic number density $n \sim 5 \times 10^{22}$ cm^{-3}. The number of atoms in a germanium nanocrystal of radius R is

$$N_c = \frac{4}{3}\pi R^3 n \tag{1}$$

The number of atoms in a non-conducting shell of thickness $t = (R_{sh} - R)$ is

$$N_{sh} = \frac{4}{3}\pi(R_{sh}{}^3 - R^3) \tag{2}$$

The ratio of atoms in the shell to those in the crystal is

$$\frac{N_{sh}}{N_c} = \left(\frac{R_{sh}{}^3 - R^3}{R^3}\right) \tag{3}$$

Now, every atom must be in a nanocrystal, in a shell, or neither. The fraction in a nanocrystal is just X_{Ge}, and the fraction in a shell is

$$\frac{N_{sh}}{N_c} X_{Ge} \tag{4}$$

and Equation (4) can be multiplied by (1-X_{Ge}) to arrive at the fraction of shell atoms that are Si and not Ge, so that we don't double-count Ge atoms in a nanocrystal but close to another nanocrystal. When at the percolation threshold for the Si phase that isn't in a shell, the fraction of atoms that are part of the conducting Si phase

$$X_{Si-cond} = 1 - X_{Ge} - \left(\frac{N_{sh}}{N_c} X_{Ge} (1 - X_{Ge}) \right) = 0.2 \tag{5}$$

Solving Equation (5) for R_{sh} using X_{Ge} = 0.2 and R = 2 nm yields R_{sh} = 3.36 nm.

Appendix B

The calculation for R_{sh} when considering the void fraction proceeds in a similar fashion to in Appendix A. Since the non-conducting shell exists around the voids here, Equation (4) is rewritten for the void fraction

$$\frac{N_{sh}}{N_c} X_{Void} \tag{6}$$

where X_{Void} ~ 0.37, estimated from Figure 4.9. To find the fraction of shell atoms that are Si and not Ge or voids, Equation (6) is multiplied by X_{Si}, which is estimated from Figure 4.9 to be ~ 50%. Now, Equation (5) is rewritten as

$$X_{Si-cond} = 1 - X_{Ge} - X_{Void} - \left(\frac{N_{sh}}{N_c} X_{Void} X_{Si} \right) = 0.2 \tag{7}$$

where X_{Ge} is the total volume fraction of the germanium phase (X_{Ge} ~ 0.13, estimated from Figure 4.9) and the calculation yields R_{sh} = 2.76 nm.